DEVELOPMENT OF A POLYNOMIAL NODAL METHOD WITH FLUX AND CURRENT DISCONTINUITY FACTORS

by

Michael Leigh Zerkle

B.S. Nuclear Engineering, University of Cincinnati
(1986)

S.M. Nuclear Engineering, Massachusetts Institute of Technology
(1989)

SUBMITTED TO THE DEPARTMENT OF
NUCLEAR ENGINEERING
IN PARTIAL FULFILLMENT OF THE REQUIREMENTS
FOR THE DEGREE OF

DOCTOR OF PHILOSOPHY

at the

MASSACHUSETTS INSTITUTE OF TECHNOLOGY

June 1992

© Massachusetts Institute of Technology 1992
All Rights Reserved

Signature of Author ________________________________
Department of Nuclear Engineering
February 20, 1992

Certified by ________________________________
Allan F. Henry
Thesis Supervisor

Certified by ________________________________
Lawrence M. Lidsky
Thesis Supervisor

Accepted by ________________________________
Allan F. Henry
Chairman, Departmental Committee on Graduate Students

MASSACHUSETTS INSTITUTE
OF TECHNOLOGY

JUN 23 1992

ARCHIVES

DEVELOPMENT OF A POLYNOMIAL NODAL METHOD WITH FLUX AND CURRENT DISCONTINUITY FACTORS

by

Michael Leigh Zerkle

Submitted to the Department of Nuclear Engineering
on February 20, 1992 in partial fulfillment of the
requirements of the Degree of Doctor of Philosophy
in the field of Nuclear Engineering

ABSTRACT

The objective of this research was the development of a computationally efficient polynomial nodal method for solving the multidimensional, few-group, static neutron diffusion equation. This nodal method permits discontinuities in the face-averaged fluxes and net-currents through the use of flux and current discontinuity factors. Discontinuous face-averaged net-currents were permitted in order to accommodate advance spatial homogenization methods. This research also explores a nonlinear iteration scheme based on the coarse mesh finite-difference (CMFD) method. This iteration scheme uses the polynomial nodal method to determine the inter-nodal coupling and to generate coarse mesh finite-difference discontinuity factor ratios. The coarse mesh finite-difference discontinuity factor ratios are then used to force the CMFD method to reproduce the polynomial nodal method solution. The use of this nonlinear iteration scheme reduces the number of unknowns required by the nodal method.

The accuracy of this nodal method for assembly sized nodes is consistent with other nodal methods and much higher than finite-difference methods. The computational efficiency of this nodal method is slightly lower than other nodal methods. The reduced computational efficiency is believed to be a consequence of the additional generality of this nodal method. Instability problems were encountered with three-dimensional problems where the axial mesh size was much greater than the radial mesh size. For three-dimensional problems the axial mesh size must be less than three times the radial mesh size to guarantee stability.

Thesis Supervisor:	Allan F. Henry
Title:	Professor of Nuclear Engineering
Thesis Supervisor:	Lawrence M. Lidsky
Title:	Professor of Nuclear Engineering

ACKNOWLEDGEMENTS

I would like to express my gratitude to Professor Allan F. Henry for the support and guidance he has provided. Over the years I have found my association with Professor Henry to be particularly rewarding.

I would also like to express my gratitude for the assistance Professor Lawrence M. Lidsky has provided. Access to the workstations used in the development of this work were provided by Professor Lidsky. Professor Lidsky also arranged a Visiting Scientist position at the Kernforschungsanlange Jülich during the summer of 1989 and I found this experience particularly rewarding.

Many of my fellow graduate students have been especially helpful over the years. Whether through their technical contributions or their help in maintaining my perspective and sanity. In particular, I would like to thank Robert Jacqmin, Jess Gehin, Andy Dobrzeniecki and Jerry Martin.

And finally, I would like to thank my wife Christine for the love and, sometimes not so gentle, encouragement she has provided.

TABLE OF CONTENTS

ABSTRACT 2

ACKNOWLEDGEMENTS 3

TABLE OF CONTENTS 4

LIST OF FIGURES 8

LIST OF TABLES 10

CHAPTER 1 INTRODUCTION 12

1.1 BACKGROUND 12

1.2 OBJECTIVE OF RESEARCH 13

1.3 THESIS OVERVIEW 14

CHAPTER 2 SOLUTION OF THE STATIC NEUTRON DIFFUSION EQUATION WITH AN EXTRANEOUS NEUTRON SOURCE 16

2.1 INTRODUCTION 16

2.2 CMFD WITH FLUX AND CURRENT DISCONTINUITY FACTORS 20

2.2.1 Boundary Conditions 24

2.3 POLYNOMIAL NODAL METHOD WITH FLUX AND CURRENT DISCONTINUITY FACTORS 26

2.3.1 Transverse-Integrated Neutron Diffusion Equation 26

2.3.2 Polynomial Expansion 27

2.3.3 Nodal Coupling Equation 34

2.3.3.1 Boundary Conditions 36

2.3.4 CMFD Discontinuity Factor Ratios 37

2.4 SUMMARY 38

CHAPTER 3 NUMERICAL CONSIDERATIONS 39

3.1 INTRODUCTION 39

3.2 NUMERICAL PROPERTIES 39

3.3 ITERATION STRATEGIES FOR EIGENVALUE PROBLEMS 43

3.3.1 Outer Iterations 43

3.3.2 Inner Iterations 48

3.3.3 Flux Iterations 49

3.3.4 General Iteration Strategy 51

3.4 ITERATION STRATEGIES FOR SOURCE PROBLEMS 54

3.4.1 Outer Iterations 54

3.4.2 Inner Iterations 55

3.4.3 Flux Iterations 56

3.4.4 General Iteration Strategies 57

3.5 ITERATION OPTIMIZATION 59

3.5.1 Inner Iterations 59

3.5.2 Flux Iterations 61

3.5.3 Eigenvalue Shift Optimization 63

3.6 SUMMARY 71

CHAPTER 4 RESULTS 72

4.1 INTRODUCTION 72

4.2 QUAGMIRE CODE 72

4.2.1 Transverse-Leakage Approximation at the Reactor Boundary 73

4.2.2 Measurements of Error 75

4.2.3 Number of Unknowns 77

4.2.4 Execution Times 78

4.3 2D STATIC RESULTS 81

4.3.1 Two-Group Homogeneous Bare Core Benchmark Problem 81

4.3.2 Seven-Group Homogeneous Bare Core Benchmark Problem 86

4.3.3 2D IAEA PWR Benchmark Problem 88

4.3.4 2D LRA BWR Static Benchmark Problem 95

4.3.5 2D LMFBR Static Benchmark Problem 101
4.3.6 CISE BWR Benchmark Problem 104
4.3.7 HAFAS BWR Benchmark Problem 106
4.3.8 Two-Group Source Benchmark Problem 108
4.4 3D STATIC RESULTS 110
4.4.1 3D IAEA PWR Benchmark Problem 110
4.4.2 3D LRA BWR Static Benchmark Problem 114
4.4.3 3D LMFBR Static Benchmark Problem 117
4.5 STABILITY CONSIDERATIONS 119
4.6 SUMMARY 123

CHAPTER 5 SUMMARY 124
5.1 OVERVIEW OF THE INVESTIGATION 124
5.2 CONCLUSIONS AND RECOMMENDATIONS 125
5.2.1 Removing Axial Mesh Restriction 126
5.2.2 Conjugant Gradient Methods 126
5.2.3 Thermal-Hydraulic Feedback 127
5.2.4 Time Dependence 128
5.2.5 Other Coordinate Systems 128

REFERENCES 129

APPENDIX A DERIVATION OF THE FLUX AND CURRENT MOMENTS 132

APPENDIX B DERIVATION OF THE TRANSVERSE-LEAKAGE MOMENTS 137
B.1 QUADRATIC TRANSVERSE-LEAKAGE APPROXIMATION 138
B.2 LHS-BIASED QUADRATIC TRANSVERSE-LEAKAGE APPROXIMATION 141
B.3 RHS-BIASED QUADRATIC TRANSVERSE-LEAKAGE APPROXIMATION 143

B.4 FLAT TRANSVERSE-LEAKAGE APPROXIMATION 145

APPENDIX C DESCRIPTION OF BENCHMARK PROBLEMS 146

C.2 TWO-GROUP HOMOGENEOUS BARE CORE BENCHMARK PROBLEM 147

C.2 SEVEN-GROUP HOMOGENEOUS BARE CORE BENCHMARK PROBLEM 148

C.3 IAEA PWR BENCHMARK PROBLEM 149

C.4 LRA BWR STATIC BENCHMARK PROBLEM 152

C.5 LMFBR STATIC BENCHMARK PROBLEM 155

C.6 CISE BWR BENCHMARK PROBLEM 161

C.7 HAFAS BWR BENCHMARK PROBLEM 166

C.8 TWO-GROUP SOURCE BENCHMARK PROBLEM 174

APPENDIX D CORE MAPS 176

LIST OF FIGURES

Figure Page

4-1 Two-Group Bare Core Problem: Eigenvalue Error versus Mesh Size 84

4-2 Two-Group Bare Core Problem: Eigenvalue Error versus Mesh Size (Very Fine Mesh) 84

4-3 Two-Group Bare Core Problem: Eigenvalue Error versus h^2 85

4-4 Two-Group Bare Core Problem: Eigenvalue Error versus h^4 85

4-5 2D IAEA PWR Benchmark Problem: Traverse of the Transverse-Integrated, X-Directed Fast Flux Along the Core Centerline (j = 1) for Several Spatial Mesh Sizes 93

4-6 2D IAEA PWR Benchmark Problem: Traverse of the Transverse-Integrated, X-Directed Thermal Flux Along the Core Centerline (j = 1) for Several Spatial Mesh Sizes 94

4-7 2D LRA BWR Static Benchmark Problem: Traverse of the Transverse-Integrated, X-Directed Fast Flux Along the Core Centerline (j = 1) for Several Spatial Mesh Sizes 99

4-8 2D LRA BWR Static Benchmark Problem: Traverse of the Transverse-Integrated, X-Directed Thermal Flux Along the Core Centerline (j = 1).for Several Spatial Mesh Sizes 100

4-9 3D LRA BWR Static Benchmark Problem: Z-Directed Fast and Thermal Flux Traverse for Nodes (1,1,k) Prior to Instability, 7.5x7.5x25(10) cm Spatial Mesh 120

4-10 3D LRA BWR Static Benchmark Problem: Z-Directed Fast Flux Traverse in the Lower Axial Reflector for Nodes (1,1,k) Prior to Instability, 7.5x7.5x25(10) cm Spatial Mesh 121

4-11 3D LRA BWR Static Benchmark Problem: Z-Directed Thermal Flux Traverse in the Lower Axial Reflector for Nodes (1,1,k) Prior to Instability, 7.5x7.5x25(10) cm Spatial Mesh 122

D-1 Seven-Group Homogeneous Bare Core Problem: Error in Normalized Nodal Power Density 177

D-2 2D IAEA PWR Benchmark Problem: Error in Normalized Assembly Power Density 178

D-3 2D IAEA PWR Benchmark Problem: Relative Error in Normalized Assembly Power Density 179

D-4 2D LRA BWR Static Benchmark Problem: Error in Normalized Assembly Power Density 180

D-5 2D LRA BWR Static Benchmark Problem: Relative Error in Normalized Assembly Power Density 181

D-6 CISE BWR Benchmark Problem: Error in Normalized Assembly Power Density 182

D-7 HAFAS BWR Benchmark Problem: Error in Normalized Assembly Power Density 183

D-8 Two-Group Source Benchmark Problem: Error in Assembly-Averaged Flux 184

D-9 3D IAEA PWR Benchmark Problem: Error in Normalized Assembly Power Density 185

D-10 3D IAEA PWR Benchmark Problem: Relative Error in Normalized Assembly Power Density 186

D-11 3D LRA BWR Static Benchmark Problem: Error in Normalized Assembly Power Density 187

D-12 3D LRA BWR Static Benchmark Problem: Relative Error in Normalized Assembly Power Density 188

LIST OF TABLES

Table Page

3-1 Inner Iteration Optimization 60

3-2 Flux Iteration Optimization 62

3-3 Eigenvalue Shift Optimization (Coarse Mesh IAEA PWR) 66

3-4 Eigenvalue Shift Optimization (Fine Mesh IAEA PWR) 67

3-5 Eigenvalue Shift Optimization (Very Fine Mesh IAEA PWR) 68

3-6 Eigenvalue Shift Optimization (Coarse Mesh LRA BWR) 69

3-7 Eigenvalue Shift Optimization (Fine Mesh LRA BWR) 70

4-1 Number of Unknowns Required by Nodal Methods 77

4-2 LINPACK MFLOPS Ratings for Several Computer Systems 80

4-3 Two-Group Bare Core Problem: Errors at Selected Mesh Sizes 83

4-4 Summary of Results for the Seven-Group Homogeneous Bare Core Benchmark Problem 87

4-5 Summary of Results for the 2D IAEA PWR Benchmark Problem 90

4-6 Summary of Results for the 2D IAEA PWR Benchmark Problem Obtained by Several Nodal Codes with a 20 cm Mesh 91

4-7 Summary of Results for the 2D IAEA PWR Benchmark Problem Obtained by Several Nodal Codes with a 10 cm Mesh 92

4-8 Summary of Results for the 2D LRA BWR Static Benchmark Problem 97

4-9 Comparison of Results for the 2D LRA BWR Static Benchmark Problem with Assembly-Sized Nodes 98

4-10 Summary of Results for the 2D LMFBR Static Benchmark Problem 102

4-11 Comparison of Results for the 2D LMFBR Static Benchmark Problem 103

4-12 Summary of Results for the CISE BWR Benchmark Problem 105

4-13 Summary of Results for the HAFAS BWR Benchmark Problem 107

4-14 Summary of Results for the Two-Group Source Benchmark Problem 109

4-15 Summary of Results for the 3D IAEA PWR Benchmark Problem 112

4-16 Comparison of Coarse Mesh 3D IAEA PWR Benchmark Solutions 113

4-17 Summary of Results for the 3D LRA BWR Static Benchmark Problem............ 115

4-18 Comparison of Coarse Mesh 3D LRA BWR Static Benchmark Solutions 116

4-19 Summary and Comparison of Results for the 3D LMFBR Static Benchmark Problem 118

CHAPTER 1

INTRODUCTION

1.1 BACKGROUND

The finite-difference method has been the principal technique for solving the neutron diffusion equation for more than 35 years. The computer codes based on the finite-difference method [C1, F4, V1] that were developed were robust and employed the most efficient iterative techniques that were available at the time. However, finite-differencing is inherently a brute force approach to the problem. Even with the continued advancements in computer technology, there remained constraints on the size and class of problems that may be solved because of practical limitations on computer storage and execution time.

Over the last 15 year modern, consistently formulated nodal methods [L1] have been developed that rival the accuracy of finite-difference methods while using a coarse, assembly-sized mesh. These modern nodal methods typically reduced the execution time required to solve these problems by two orders of magnitude. Modern nodal methods typically break a multidimensional problem into a series of one-dimensional problems by integrating the neutron diffusion equation over the directions transverse to each coordinate axis. The procedures used to solve the resulting transverse-integrated diffusion equation may be used as a natural basis for separating modern nodal methods into two additional classes: analytic and polynomial. Analytic nodal methods are based on the analytic solution of the transverse-integrated diffusion equation for each node. The QUANDRY [S2] code is an example of the analytic nodal method. However, because of its complexity the analytic nodal method is effectively restricted to modelling problems with no more than two energy groups. Polynomial nodal methods approximate the solution of the transverse-integrated diffusion equation for each node with a low order polynomial expansion. The Nodal Expansion Method (NEM) [B1, B2, F1, F2] is an example of the first generation of polynomial nodal methods. One of the principal advantages of polynomial nodal methods is that they have no effective restriction on the number of energy groups that may be modelled. The accuracy of both analytic and polynomial nodal methods is comparable.

Parallel to the development of modern nodal methods considerable advancements in spatial homogenization methods have been made [S4]. Homogenized cross sections for assembly sized nodes are typically obtained using the conventional flux-weighting procedure, with each assembly type being modelled using zero net-current boundary conditions. This conventional approach does not provide enough degrees of freedom to match both the flux distribution and the eigenvalue. Smith [S3] provided the sufficient degrees of freedom by permitting the nodal face-averaged fluxes to be discontinuous. These discontinuity factors are typically obtained for an assembly by taking the ratio of the average flux on the face to the node-averaged flux.

At MIT there has recently been interest in homogenization methods for space-time analysis [K1, T1]. Currently, conventional flux-weighting procedures are used to generate homogenized cross sections for use in space-time analysis. Kim [K1] and Tarantino [T1] explored several bilinear weighting schemes based on variational theory. These bilinear weighting schemes typically required discontinuities in both the face-averaged flux and net-current [T1].

1.2 OBJECTIVE OF RESEARCH

The objective of this research is the development of an efficient polynomial nodal method for the solution of the multidimensional, few-group, static neutron diffusion equation. The nodal method will permit discontinuities in both the face-averaged flux and net-current. This extended set of homogenization parameters is proposed to support future research in advanced spatial homogenization methods. There is to be no restrictions on the number of energy groups or the structure of the energy groups.

Upscattering will be permitted. Extraneous neutrons sources will also be modelled. Therefore, the nodal method will solve both eigenvalue and source problems.

The second objective of this research is the development of a nonlinear iteration scheme based on the coarse mesh finite-difference (CMFD) method. In the proposed iteration scheme the higher-order polynomial nodal method is used to determine the inter-nodal coupling. CMFD discontinuity factor ratios which will reproduce the polynomial nodal method results are then determined. The CMFD method will then be used to determine the node-averaged flux. This nonlinear iteration scheme was selected because it is believed to reduce the storage and execution time requirements of the nodal method. It was also selected because the numerical properties of the CMFD method are better understood.

1.3 THESIS OVERVIEW

In Chapter 2 a coarse mesh finite-difference (CMFD) method and a polynomial nodal method both which permit discontinuities in the face-averaged flux and net-current are derived. First the CMFD method is derived. CMFD discontinuity factor ratios which will reproduce a reference solution are defined. Then a polynomial nodal method with flux and current discontinuity factors is derived. Finally, a procedure for determining CMFD discontinuity factor ratios using the polynomial nodal method is described.

In Chapter 3 the numerical properties of the nodal method are discussed. A procedure for guaranteeing the stability of the iterative solution is described. The iterative scheme used to solve both eigenvalue and source problems are described. Finally the issues regarding the optimization of the iterative solution are discussed.

In Chapter 4 the QUAGMIRE code is described. The QUAGMIRE solutions for a variety two-dimensional and three-dimensional benchmark problems are presented and compared to other nodal methods and finite-difference methods.

Finally, in Chapter 5 the results of this research are summarized. Conclusions and recommendations for further research are made.

CHAPTER 2

SOLUTION OF THE STATIC NEUTRON DIFFUSION EQUATION WITH AN EXTRANEOUS NEUTRON SOURCE

2.1 INTRODUCTION

In this chapter two numerical methods for solving the static neutron diffusion equation with an extraneous neutron source are derived. These methods permit discontinuities in both the face-averaged flux and the face-averaged net current at nodal interfaces. First a coarse mesh finite-difference (CMFD) method with flux and current discontinuity factors is derived. CMFD discontinuity factor ratios are defined which will reproduce a reference flux distribution. Then a polynomial nodal method with flux and current discontinuity factor ratios is derived. Finally, a procedure for obtaining CMFD discontinuity factor ratios using the polynomial nodal method is described.

Written in the standard P_1 form [H2], the static neutron diffusion equation with an extraneous neutron source is

$$\nabla \cdot \mathbf{J}_g(\mathbf{r}) + \Sigma_{tg}(\mathbf{r})\phi_g(\mathbf{r}) = \sum_{g'=1}^{G} \left(\frac{1}{\lambda}\chi_g(\mathbf{r})\nu\Sigma_{fg'}(\mathbf{r}) + \Sigma_{gg'}(\mathbf{r}) \right)\phi_{g'}(\mathbf{r}) + q_g(\mathbf{r}) \qquad (2\text{-}1a)$$

$$\mathbf{J}_g(\mathbf{r}) = -D_g(\mathbf{r})\nabla\phi_g(\mathbf{r}), \quad g=1,2,\cdots,G \qquad (2\text{-}1b)$$

where,

J_g = net current of neutrons in group g ($cm^{-2}\,s^{-1}$),
ϕ_g = scalar neutron flux in group g ($cm^{-2}\,s^{-1}$),
λ = reactor eigenvalue,
Σ_{tg} = macroscopic total neutron cross section (cm^{-1}),
χ_g = fission neutron spectrum for group g,
$\nu\Sigma_{fg}$ = mean number of neutrons emitted per fission times the macroscopic fission cross section for group g (cm^{-1}),
$\Sigma_{gg'}$ = macroscopic transfer cross section from group g' to g (cm^{-1}),
q_g = extraneous neutron source ($cm^{-3}\,s^{-1}$),
D_g = diffusion coefficient for group g (cm),
G = total number of energy groups.

We will use three-dimensional Cartesian geometry to model the global reactor problem. A general notation for the coordinate directions will prove to be very useful; therefore u, v, and w are used as the generalized coordinate subscripts. The spatial domain of the reactor is partitioned into a regular array of right rectangular parallelepipeds (nodes) with grid indices defined by u_l, v_m, w_n where

$$l, m, n \equiv \begin{cases} i = 1, 2, \ldots, I+1 & u = x, y, z \\ j = 1, 2, \ldots, J+1 & v \neq u \\ k = 1, 2, \ldots, K+1 & w \neq u \neq v\,. \end{cases}$$

The node (i,j,k) is defined by

$$\begin{aligned} x &\in [x_i, x_{i+1}], \\ y &\in [y_j, y_{j+1}], \\ z &\in [z_k, z_{k+1}]. \end{aligned}$$

The node widths are defined by

$$h_u^l \equiv u_{l+1} - u_l; \quad u = x, y, z$$

and the node volume is

$$V^{i,j,k} \equiv h_x^i \, h_y^j \, h_z^k.$$

In Cartesian geometry Equations (2-1a) and (2-1b) are

$$\begin{aligned} &\frac{\partial}{\partial x} J_{gx}(x,y,z) + \frac{\partial}{\partial y} J_{gy}(x,y,z) + \frac{\partial}{\partial z} J_{gz}(x,y,z) + \Sigma_{tg}(x,y,z)\,\phi_g(x,y,z) = \\ &\sum_{g'=1}^{G} \left(\frac{1}{\lambda} \chi_g(x,y,z)\, \nu\Sigma_{fg'}(x,y,z) + \Sigma_{gg'}(x,y,z) \right) \phi_{g'}(x,y,z) + q_g(x,y,z)\,, \end{aligned} \tag{2-2a}$$

$$J_{gu}(x,y,z) = -D_g(x,y,z) \frac{\partial}{\partial u} \phi_g(x,y,z), \quad u = x,y,z\,. \tag{2-2b}$$

We assume spatially homogeneous cross sections and extraneous neutron source within node (ijk). Typically these few-group cross sections result from group condensation and spatial homogenization using an assembly transport calculation. We also permit discontinuities in the face-averaged flux and the face-averaged current. The flux discontinuity factors provide the additional degrees of freedom required by many spatial homogenization methods. If bilinear-weighting is used both the flux and current discontinuity factors provide the additional homogenization parameters required by this weighting scheme. The flux continuity condition at the node boundaries becomes

$$f_{gu,\phi}^{l-1,mn}(u_l^-)\,\phi_{gu}^{l-1,mn}(u_l^-) \equiv f_{gu,\phi}^{lmn}(u_l^+)\,\phi_{gu}^{lmn}(u_l^+) \tag{2-3}$$

where,

$\phi_{gu}^{l-1,mn}(u_l^-)$ = homogenized u-directed face-averaged flux at u_l^-,

$\phi_{gu}^{lmn}(u_l^+)$ = homogenized u-directed face-averaged flux at u_l^+,

$f_{gu,\phi}^{l-1,mn}(u_l^-)$ = u-directed flux discontinuity factor at u_l^-,

$f_{gu,\phi}^{lmn}(u_l^+)$ = u-directed flux discontinuity factor at u_l^+.

Similarly, the current continuity condition at the node boundaries becomes

$$f_{gu,J}^{l-1,mn}(u_l^-)\,J_{gu}^{l-1,mn}(u_l^-) \equiv f_{gu,J}^{lmn}(u_l^+)\,J_{gu}^{lmn}(u_l^+) \tag{2-4}$$

where,

$J_{gu}^{l-1,mn}(u_l^-)$ = homogenized u-directed face-averaged current at u_l^-,

$J_{gu}^{lmn}(u_l^+)$ = homogenized u-directed face-averaged current at u_l^-,

$f_{gu,J}^{l-1,mn}(u_l^-)$ = u-directed current discontinuity factor at u_l^-,

$f_{gu,J}^{lmn}(u_l^+)$ = u-directed current discontinuity factor at u_l^+.

The neutron balance equation is obtained by integrating Equation (2-2a) over the node volume, V^{ijk}, and then dividing by V^{ijk},

$$\begin{gathered}\frac{1}{h_x^i}\left[J_{gx}^{ijk}(x_{i+1}^-) - J_{gx}^{ijk}(x_i^+)\right] + \frac{1}{h_y^j}\left[J_{gy}^{ijk}(y_{j+1}^-) - J_{gy}^{ijk}(y_j^+)\right] + \frac{1}{h_z^k}\left[J_{gz}^{ijk}(z_{k+1}^-) - J_{gz}^{ijk}(z_k^+)\right] + \\ \Sigma_{tg}^{ijk}\bar{\phi}_g^{ijk} = \sum_{g'=1}^{G}\left(\frac{1}{\lambda}\chi_g^{ijk}\nu\Sigma_{fg'}^{ijk} + \Sigma_{gg'}^{ijk}\right)\bar{\phi}_{g'}^{ijk} + \bar{q}_g^{ijk}, \qquad g = 1, 2, \cdots, G\end{gathered} \tag{2-5}$$

where,

$$\bar{\phi}_g^{ijk} \equiv \frac{1}{V^{ijk}} \int_{x_i^+}^{x_{i+1}^-} dx \int_{y_j^+}^{y_{j+1}^-} dy \int_{z_k^+}^{z_{k+1}^-} dz\, \phi_g(x,y,z), \tag{2-6}$$

$$\bar{q}_g^{ijk} \equiv \frac{1}{V^{ijk}} \int_{x_i^+}^{x_{i+1}^-} dx \int_{y_j^+}^{y_{j+1}^-} dy \int_{z_k^+}^{z_{k+1}^-} dz\, q_g(x,y,z), \tag{2-7}$$

$$J_{ug}^{lmn}(u) \equiv \frac{1}{h_v^m h_w^n} \int_{v_m^+}^{v_{m+1}^-} dv \int_{w_n^+}^{w_{n+1}^-} dw \;\; J_{gu}(u,v,w), \qquad \begin{array}{l} u = x,\ y,\ z \\ v \neq u \\ w \neq v \neq u \end{array} . \tag{2-8}$$

Combining the total minus transfer terms and the fission source terms yields a more compact expression for the neutron balance equation,

$$\begin{gathered} \frac{1}{h_x^i}\left[J_{gx}^{ijk}(x_{i+1}^-) - J_{gx}^{ijk}(x_i^+)\right] + \frac{1}{h_y^j}\left[J_{gy}^{ijk}(y_{j+1}^-) - J_{gy}^{ijk}(y_j^+)\right] + \frac{1}{h_z^k}\left[J_{gz}^{ijk}(z_{k+1}^-) - J_{gz}^{ijk}(z_k^+)\right] + \\ \sum_{g'=1}^{G} A_{gg'}^{ijk}\bar{\phi}_{g'}^{ijk} = \frac{1}{\lambda}\sum_{g'=1}^{G} F_{gg'}^{ijk}\bar{\phi}_{g'}^{ijk} + \bar{q}_g^{ijk}, \qquad g = 1, 2, \cdots, G \end{gathered} \tag{2-9}$$

where

$$A_{gg'}^{ijk} = \Sigma_{tg}^{ijk}\delta_{gg'} - \Sigma_{gg'}^{ijk}, \tag{2-10}$$

$$F_{gg'}^{ijk} = \chi_g^{ijk}\nu\Sigma_{fg'}^{ijk}. \tag{2-11}$$

2.2 CMFD WITH FLUX AND CURRENT DISCONTINUITY FACTORS

The CMFD expressions defining the homogenized face-averaged currents at the RHS and LHS of u_l are

$$J_{gu}^{lmn}(u_l^+) \equiv -\frac{2D_g^{lmn}}{h_u^l}\left[\bar{\phi}_g^{lmn} - \frac{\phi_{gu}^{lmn}(u_l^+)}{f_{gu}^{lmn}(u_l^+)}\right] \qquad (2\text{-}12)$$

$$J_{gu}^{l-1,mn}(u_l^-) \equiv -\frac{2D_g^{l-1,mn}}{h_u^{l-1}}\left[\frac{\phi_{gu}^{l-1,mn}(u_l^-)}{f_{gu}^{l-1,mn}(u_l^-)} - \bar{\phi}_g^{l-1,mn}\right] \qquad (2\text{-}13)$$

where the CMFD discontinuity factors $f_{gu}^{lmn}(u_l^+)$ and $f_{gu}^{l-1,mn}(u_l^-)$ are introduced to force the CMFD method to match the results of a reference calculation [H3]. We also define the heterogeneous face-averaged flux using the face-averaged flux continuity condition,

$$\phi_{gu}^{mn}(u_l) \equiv f_{gu,\phi}^{lmn}(u_l^+)\phi_{gu}^{lmn}(u_l^+) = f_{gu,\phi}^{l-1,mn}(u_l^-)\phi_{gu}^{l-1,mn}(u_l^-). \qquad (2\text{-}14)$$

Similarly, the heterogeneous face-averaged current is defined using the face-averaged current continuity condition,

$$J_{gu}^{mn}(u_l) \equiv f_{gu,J}^{lmn}(u_l^+)J_{gu}^{lmn}(u_l^+) = f_{gu,J}^{l-1,mn}(u_l^-)J_{gu}^{l-1,mn}(u_l^-). \qquad (2\text{-}15)$$

Expressions for the heterogeneous face-averaged current at u_l can be obtained by multiplying Equation (2-12) by $f_{gu,J}^{lmn}(u_l^+)$ and multiplying Equation (2-13) by $f_{gu,J}^{l-1,mn}(u_l^-)$ yielding

$$J_{gu}^{mn}(u_l) = -f_{gu,J}^{lmn}(u_l^+)\left(\frac{2D_g^{lmn}}{h_u^l}\right)\left[\bar{\phi}_g^{lmn} - \frac{\phi_{gu}^{mn}(u_l)}{f_{gu,\phi}^{lmn}(u_l^+)f_{gu}^{lmn}(u_l^+)}\right] \qquad (2\text{-}16a)$$

$$= -f_{gu,J}^{l-1,mn}(u_l^-)\left(\frac{2D_g^{l-1,mn}}{h_u^{l-1}}\right)\left[\frac{\phi_{gu}^{mn}(u_l)}{f_{gu,\phi}^{l-1,mn}(u_l^-)f_{gu}^{l-1,mn}(u_l^-)} - \bar{\phi}_g^{l-1,mn}\right]. \qquad (2\text{-}16b)$$

Expressions for the heterogeneous face-averaged flux at u_l is obtained by rearranging Equation (2-16),

$$\phi_{gu}^{mn}(u_l) = f_{gu,\phi}^{lmn}(u_l^+) f_{gu}^{lmn}(u_l^+) \left[\bar{\phi}_g^{lmn} + \frac{h_u^l}{2D_g^{lmn}} \frac{J_{gu}^{mn}(u_l)}{f_{gu,J}^{lmn}(u_l^+)} \right] \tag{2-17a}$$

$$= f_{gu,\phi}^{l-1,mn}(u_l^-) f_{gu}^{l-1,mn}(u_l^-) \left[\bar{\phi}_g^{l-1,mn} - \frac{h_u^{l-1}}{2D_g^{l-1,mn}} \frac{J_{gu}^{mn}(u_l)}{f_{gu,J}^{l-1,mn}(u_l^-)} \right]. \tag{2-17b}$$

Setting Equation (2-17a) equal to Equation (1-17b) and rearranging yields,

$$\begin{gathered} \left[\frac{h_u^{l-1}}{2D_g^{l-1,mn}} \frac{f_{gu,\phi}^{l-1,mn}(u_l^-) f_{gu}^{l-1,mn}(u_l^-)}{f_{gu,J}^{l-1,mn}(u_l^-)} + \frac{h_u^l}{2D_g^{lmn}} \frac{f_{gu,\phi}^{lmn}(u_l^+) f_{gu}^{lmn}(u_l^+)}{f_{gu,J}^{lmn}(u_l^+)} \right] J_{gu}^{mn}(u_l) = \\ \left[f_{gu,\phi}^{l-1,mn}(u_l^-) f_{gu}^{l-1,mn}(u_l^-) \bar{\phi}_g^{l-1,mn} - f_{gu,\phi}^{lmn}(u_l^+) f_{gu}^{lmn}(u_l^+) \bar{\phi}_g^{lmn} \right]. \end{gathered} \tag{2-18}$$

We then define the following discontinuity factor ratios:

$$r_{gu}^{mn}(u_l) \equiv \frac{f_{gu}^{lmn}(u_l^+)}{f_{gu}^{l-1,mn}(u_l^-)}, \tag{2-19a}$$

$$r_{gu,\phi}^{mn}(u_l) \equiv \frac{f_{gu,\phi}^{lmn}(u_l^+)}{f_{gu,\phi}^{l-1,mn}(u_l^-)}, \tag{2-19b}$$

$$r_{gu,J}^{mn}(u_l) \equiv \frac{f_{gu,J}^{lmn}(u_l^+)}{f_{gu,J}^{l-1,mn}(u_l^-)}. \tag{2-19c}$$

Then dividing Equation (2-18) by $f_{gu,\phi}^{l-1,mn}(u_l^-) f_{gu}^{l-1,mn}(u_l^-)$, substituting in the discontinuity factor ratios, and rearranging yields the following expression for the heterogeneous face-averaged current at u_l,

$$\begin{gathered} J_{gu}^{mn}(u_l) = \left[\frac{h_u^{l-1}}{2D_g^{l-1,mn}} \frac{1}{f_{gu,J}^{l-1,mn}(u_l^-)} + \frac{h_u^l}{2D_g^{lmn}} \frac{r_{gu,\phi}^{mn}(u_l) r_{gu}^{mn}(u_l)}{f_{gu,J}^{lmn}(u_l^+)} \right]^{-1} \times \\ \left[\bar{\phi}_g^{l-1,mn} - r_{gu,\phi}^{mn}(u_l) r_{gu}^{mn}(u_l) \bar{\phi}_g^{lmn} \right]. \end{gathered} \tag{2-20}$$

Substituting the current continuity condition into Equation (2-10) and dividing through by $f_{gu,J}^{lmn}(u_l^+)$ yields the LHS component of the u-directed leakage term,

$$-J_{gu}^{mn}(u_l^+) = \left[\frac{h_u^{l-1}}{2D_g^{l-1,mn}} r_{gu,J}^{mn}(u_l) + \frac{h_u^l}{2D_g^{lmn}} r_{gu,\phi}^{mn}(u_l) r_{gu}^{mn}(u_l)\right]^{-1} \times \left[r_{gu,\phi}^{mn}(u_l) r_{gu}^{mn}(u_l) \overline{\phi}_g^{lmn} - \overline{\phi}_g^{l-1,mn}\right]. \tag{2-21}$$

Similarly, the CMFD expressions defining the homogeneous face-averaged current at the RHS and LHS faces of u_{l+1} are

$$J_{gu}^{l+1,mn}(u_{l+1}^+) \blacksquare - \frac{2D_g^{l+1,mn}}{h_u^{l+1}} \left[\overline{\phi}_g^{l+1,mn} - \frac{\phi_{gu}^{l+1,mn}(u_{l+1}^+)}{f_{gu}^{l+1,mn}(u_{l+1}^+)}\right], \tag{2-22}$$

$$J_{gu}^{lmn}(u_{l+1}^-) \blacksquare - \frac{2D_g^{lmn}}{h_u^l} \left[\frac{\phi_{gu}^{lmn}(u_{l+1}^-)}{f_{gu}^{lmn}(u_{l+1}^-)} - \overline{\phi}_g^{lmn}\right]. \tag{2-23}$$

The heterogeneous face-averaged current and flux at u_{l+1} are given by

$$J_{gu}^{mn}(u_{l+1}) = - f_{gu,J}^{l+1,mn}(u_{l+1}^+) \left(\frac{2D_g^{l+1,mn}}{h_u^{l+1}}\right) \left[\overline{\phi}_g^{l+1,mn} - \frac{\phi_{gu}^{mn}(u_{l+1})}{f_{gu,\phi}^{l+1,mn}(u_{l+1}^+) f_{gu}^{l+1,mn}(u_{l+1}^+)}\right] \tag{2-24a}$$

$$= - f_{gu,J}^{lmn}(u_{l+1}^-) \left(\frac{2D_g^{lmn}}{h_u^l}\right) \left[\frac{\phi_{gu}^{mn}(u_{l+1})}{f_{gu,\phi}^{lmn}(u_{l+1}^-) f_{gu}^{lmn}(u_{l+1}^-)} - \overline{\phi}_g^{lmn}\right], \tag{2-24b}$$

$$\phi_{gu}^{mn}(u_{l+1}) = f_{gu,\phi}^{l+1,mn}(u_{l+1}^+) f_{gu}^{l+1,mn}(u_{l+1}^+) \left[\overline{\phi}_g^{l+1,mn} + \frac{h_u^{l+1}}{2D_g^{l+1,mn}} \frac{J_{gu}^{mn}(u_{l+1})}{f_{gu,J}^{l+1,mn}(u_{l+1}^+)}\right] \tag{2-25a}$$

$$= f_{gu,\phi}^{lmn}(u_{l+1}^-) f_{gu}^{lmn}(u_{l+1}^-) \left[\overline{\phi}_g^{lmn} - \frac{h_u^l}{2D_g^{lmn}} \frac{J_{gu}^{mn}(u_{l+1})}{f_{gu,J}^{lmn}(u_{l+1}^-)}\right]. \tag{2-25b}$$

Setting (2-24a) equal to (2-24b), dividing by $f_{gu,\phi}^{l+1,mn}(u_{l+1}^+) f_{gu}^{l+1,mn}(u_{l+1}^+)$, and rearranging yields

$$J_{gu}^{mn}(u_{l+1}) = \left[\frac{h_u^l}{2D_g^{lmn}} \frac{1}{f_{gu,J}^{lmn}(u_{l+1}^-)} + \frac{h_u^{l+1}}{2D_g^{l+1,mn}} \frac{r_{gu,\phi}^{mn}(u_{l+1}) r_{gu}^{mn}(u_{l+1})}{f_{gu,J}^{l+1,mn}(u_{l+1}^+)}\right]^{-1} \times \left[\overline{\phi}_g^{lmn} - r_{gu,\phi}^{mn}(u_{l+1}) r_{gu}^{mn}(u_{l+1}) \overline{\phi}_g^{l+1,mn}\right].$$

Then substituting in the current continuity condition and rearranging yields the RHS u-directed leakage term,

$$\begin{aligned} J^{mn}_{gu}(u^-_{l+1}) = \left[\frac{h^l_u}{2D^{lmn}_g} + \frac{h^{l+1}_u}{2D^{l+1,mn}_g}\frac{r^{mn}_{gu,\phi}(u_{l+1})\,r^{mn}_{gu}(u_{l+1})}{r^{mn}_{gu,J}(u_{l+1})}\right]^{-1} \times \\ \left[\bar{\phi}^{lmn}_g - r^{mn}_{gu,\phi}(u_{l+1})\,r^{mn}_{gu}(u_{l+1})\,\bar{\phi}^{l+1,mn}_g\right]. \end{aligned} \tag{2-26}$$

Combining Equations (2-21) and (2-26), and dividing by h^l_u yields the u-directed leakage term

$$\begin{aligned} &\frac{1}{h^l_u}\left[J^{mn}_{gu}(u^-_{l+1}) - J^{mn}_{gu}(u^+_l)\right] = \\ &\frac{1}{h^l_u}\left[\frac{h^l_u}{2D^{lmn}_g} + \frac{h^{l+1}_u}{2D^{l+1,mn}_g}\frac{r^{mn}_{gu,\phi}(u_{l+1})\,r^{mn}_{gu}(u_{l+1})}{r^{mn}_{gu,J}(u_{l+1})}\right]^{-1} \times \left[\bar{\phi}^{lmn}_g - r^{mn}_{gu,\phi}(u_{l+1})\,r^{mn}_{gu}(u_{l+1})\,\bar{\phi}^{l+1,mn}_g\right] + \\ &\frac{1}{h^l_u}\left[\frac{h^{l-1}_u}{2D^{l-1,mn}_g} r^{mn}_{gu,J}(u_l) + \frac{h^l_u}{2D^{lmn}_g} r^{mn}_{gu,\phi}(u_l)\,r^{mn}_{gu}(u_l)\right]^{-1} \times \left[r^{mn}_{gu,\phi}(u_l)\,r^{mn}_{gu}(u_l)\,\bar{\phi}^{lmn}_g - \bar{\phi}^{l-1,mn}_g\right] \end{aligned} \tag{2-27}$$

and similarly for the v-directed and w-directed leakage terms.

Finally, the CMFD balance equation for node (ijk) is obtained by substituting Equation (2-27) into (2-9),

$$\begin{aligned} &\frac{1}{h^i_x}\left[\frac{h^i_x}{2D^{ijk}_g} + \frac{h^{i+1}_x}{2D^{i+1,jk}_g}\frac{r^{jk}_{gx,\phi}(x_{i+1})\,r^{jk}_{gx}(x_{i+1})}{r^{jk}_{gx,J}(x_{i+1})}\right]^{-1} \times \left[\bar{\phi}^{ijk}_g - r^{jk}_{gx,\phi}(x_{i+1})\,r^{jk}_{gx}(x_{i+1})\,\bar{\phi}^{i+1,jk}_g\right] + \\ &\frac{1}{h^i_x}\left[\frac{h^{i-1}_x}{2D^{i-1,jk}_g} r^{jk}_{gx,J}(x_i) + \frac{h^i_x}{2D^{ijk}_g} r^{jk}_{gx,\phi}(x_i)\,r^{jk}_{gx}(x_i)\right]^{-1} \times \left[r^{jk}_{gx,\phi}(x_i)\,r^{jk}_{gx}(x_i)\,\bar{\phi}^{ijk}_g - \bar{\phi}^{i-1,jk}_g\right] + \\ &\frac{1}{h^j_y}\left[\frac{h^j_y}{2D^{ijk}_g} + \frac{h^{j+1}_y}{2D^{i,j+1,k}_g}\frac{r^{ik}_{gy,\phi}(y_{j+1})\,r^{ik}_{gy}(y_{j+1})}{r^{ik}_{gy,J}(y_{j+1})}\right]^{-1} \times \left[\bar{\phi}^{ijk}_g - r^{ik}_{gy,\phi}(y_{j+1})\,r^{ik}_{gy}(y_{j+1})\,\bar{\phi}^{i,j+1,k}_g\right] + \\ &\frac{1}{h^j_y}\left[\frac{h^{j-1}_y}{2D^{i,j-1,k}_g} r^{ik}_{gy,J}(y_j) + \frac{h^j_y}{2D^{ijk}_g} r^{ik}_{gy,\phi}(y_j)\,r^{ik}_{gy}(y_j)\right]^{-1} \times \left[r^{ik}_{gy,\phi}(y_j)\,r^{ik}_{gy}(y_j)\,\bar{\phi}^{ijk}_g - \bar{\phi}^{i,j-1,k}_g\right] + \\ &\frac{1}{h^k_z}\left[\frac{h^k_z}{2D^{ijk}_g} + \frac{h^{k+1}_z}{2D^{ij,k+1}_g}\frac{r^{ij}_{gz,\phi}(z_{k+1})\,r^{ij}_{gz}(z_{k+1})}{r^{ij}_{gz,J}(z_{k+1})}\right]^{-1} \times \left[\bar{\phi}^{ijk}_g - r^{ij}_{gz,\phi}(z_{k+1})\,r^{ij}_{gz}(z_{k+1})\,\bar{\phi}^{ij,k+1}_g\right] + \\ &\frac{1}{h^k_z}\left[\frac{h^{k-1}_z}{2D^{ij,k-1}_g} r^{ij}_{gz,J}(z_k) + \frac{h^k_z}{2D^{ijk}_g} r^{ij}_{gz,\phi}(z_k)\,r^{ij}_{gz}(z_k)\right]^{-1} \times \left[r^{ij}_{gz,\phi}(z_k)\,r^{ij}_{gz}(z_k)\,\bar{\phi}^{ijk}_g - \bar{\phi}^{ij,k-1}_g\right] + \\ &\sum_{g'=1}^{G} A^{ijk}_{gg'}\bar{\phi}^{ijk}_{g'} = \frac{1}{\lambda}\sum_{g'=1}^{G} F^{ijk}_{gg'}\bar{\phi}^{ijk}_{g'} + \bar{q}^{ijk}_g, \quad g = 1, \ldots, G. \end{aligned} \tag{2-28}$$

Note that if the flux and current discontinuity factor ratios are set equal to unity Equation (2-28) reduces to the mesh-centered finite-difference approximation to the neutron diffusion equation.

In addition, by rearranging Equation (2-17) we obtain an expression for the CMFD discontinuity factor ratio at u_l in terms of the node-averaged fluxes, the heterogeneous current at u_l, and the flux and current discontinuity factors at u_l,

$$r_{gu}^{mn}(u_l) = \frac{f_{gu,\phi}^{l-1,mn}(u_l^-)}{f_{gu,\phi}^{lmn}(u_l^+)} \frac{\left[\bar{\phi}_g^{l-1,mn} - \frac{h_u^{l-1}}{2D_g^{l-1,mn}} \frac{J_{gu}^{mn}(u_l)}{f_{gu,J}^{l-1,mn}(u_l^-)}\right]}{\left[\bar{\phi}_g^{lmn} + \frac{h_u^l}{2D_g^{lmn}} \frac{J_{gu}^{mn}(u_l)}{f_{gu,J}^{lmn}(u_l^+)}\right]}. \qquad (2\text{-}29)$$

We will find this expression quite useful in following section.

2.2.1 Boundary Conditions

The following general notation will be used to specify the reactor boundary conditions,

$$\phi_{gu}^{mn}(u_s) = \Gamma_{gu\pm}^{mn} J_{gu}^{mn}(u_s)\, \hat{l} \cdot \vec{n} \qquad (2\text{-}30)$$

where,

$\phi_{gu}^{mn}(u_s)$ = heterogeneous face-averaged flux at the external boundary u_s,
$J_{gu}^{mn}(u_s)$ = heterogeneous face-averaged current at the external boundary u_s,
u_s = external boundary,
$\vec{n}$ = outgoing unit vector normal to the external reactor boundary,
$\Gamma_{gu\pm}^{mn}$ = albedo.

The following boundary conditions may be specified:

$$
\begin{array}{lll}
\Gamma^{mn}_{gu\pm} & = 0 & \text{zero flux,} \\
 & = 2 & \text{zero incoming current,} \\
 & = \infty & \text{zero current,} \\
 & = 2 + \dfrac{4}{\alpha_g^{-1} - 1} & \text{albedo where, } \alpha_g = \dfrac{J^{in}_{gu}(u_s)}{J^{out}_{gu}(u_s)} .
\end{array}
$$

The LHS boundary condition is

$$\phi^{mn}_{gu}(u_l) = -\,\Gamma^{mn}_{gu-}\,J^{mn}_{gu}(u_l) \,.$$

The LHS component of the u-directed leakage term is obtained by substituting (2-30) into (2-16a) and rearranging,

$$-J^{mn}_{gu}(u_l^+) = \left[\frac{h_u^l}{2D_g^{lmn}} + \frac{f^{lmn}_{gu,J}(u_l^+)}{f^{lmn}_{gu,\phi}(u_l^+)}\,\frac{\Gamma^{mn}_{gu-}}{f^{lmn}_{gu}(u_l^+)}\right]^{-1} \times \bar{\phi}_g^{lmn} \,. \tag{2-31}$$

And the CMFD discontinuity factor term at the LHS boundary is given by,

$$\frac{\Gamma^{mn}_{gu-}}{f^{lmn}_{gu}(u_l^+)} = -\,f^{lmn}_{gu,\phi}(u_l^+)\left[\frac{\bar{\phi}_g^{lmn}}{J^{mn}_{gu}(u_l)} + \frac{1}{f^{lmn}_{gu,J}(u_l^+)}\,\frac{h_u^l}{2D_g^{lmn}}\right] . \tag{2-32}$$

The RHS boundary condition is

$$\phi^{mn}_{gu}(u_{l+1}) = \Gamma^{mn}_{gu+}\,J^{mn}_{gu}(u_{l+1}) \,.$$

The RHS component of the u-directed leakage term is obtained by substituting (2-30) into (2-16b) and rearranging,

$$J^{mn}_{gu}(u^-_{l+1}) = \left[\frac{h_u^l}{2D_g^{lmn}} + \frac{f^{lmn}_{gu,J}(u^-_{l+1})}{f^{lmn}_{gu,\phi}(u^-_{l+1})}\,\frac{\Gamma^{mn}_{gu+}}{f^{lmn}_{gu}(u^-_{l+1})}\right]^{-1} \times \bar{\phi}_g^{lmn} \,. \tag{2-33}$$

And the CMFD discontinuity factor term at the RHS boundary is given by,

$$\frac{\Gamma^{mn}_{gu+}}{f^{lmn}_{gu}(u^-_{l+1})} = f^{lmn}_{gu,\phi}(u^-_{l+1})\left[\frac{\bar{\phi}_g^{lmn}}{J^{mn}_{gu}(u_{l+1})} - \frac{1}{f^{lmn}_{gu,J}(u^-_{l+1})}\,\frac{h_u^l}{2D_g^{lmn}}\right] . \tag{2-34}$$

2.3 POLYNOMIAL NODAL METHOD WITH FLUX AND CURRENT DISCONTINUITY FACTORS

In this section a polynomial nodal method which permits discontinuities in the face-averaged flux and current will be derived. First the transverse-integrated neutron diffusion equation will be derived. Then the polynomial expansion of the transverse-integrated flux will be introduced and the nodal coupling equation will be derived. Finally, a procedure for determining CMFD discontinuity factor ratios will be described.

Discontinuities in the face-averaged flux and current are introduced through a more general set of homogenization parameters (few-group cross sections) which include flux and current discontinuity factors. This nodal method makes two fundemental approximations to the formally exact neutron diffusion equation. First, the transverse-integrated flux is approximated by a polynomial expansion. Second, the transverse-leakage is approximated by a quadratic polynomial.

2.3.1 Transverse-Integrated Neutron Diffusion Equation

Instead of solving the entire coupled 3D neutron diffusion problem, nodal methods typically break the 3D problem into a series of coupled 1D problems and solve each of these 1D problems in turn [F1, L1, S2]. The first step is to integrate the neutron diffusion equations in the directions transverse to the direction of interest. Operating on Equations (2-2) with

$$\frac{1}{h_v^m h_w^n}\int_{v_m^+}^{v_{m+1}^-} dv \int_{w_n^+}^{w_{n+1}^-} dw \ ,$$

yields the transverse-integrated neutron diffusion equation for node (lmn),

$$\frac{d}{du} J_{gu}^{lmn}(u) + \sum_{g'=1}^{G} A_{gg'}^{lmn}\,\phi_{g'u}^{lmn}(u) = \frac{1}{\lambda}\sum_{g'=1}^{G} F_{gg'}^{G}\,\phi_{g'u}^{lmn}(u) + \bar{q}_g^{lmn} - L_{gv}^{lmn}(u) - L_{gw}^{lmn}(u) \quad \text{(2-35a)}$$

$$J_{gu}^{lmn}(u) = - D_g^{lmn}\frac{d}{du}\phi_{gu}^{lmn}(u) \ , \quad u = x,y,z \qquad \text{(2-35b)}$$

where

$$\phi_{gu}^{lmn}(u) = \frac{1}{h_v^m h_w^n}\int_{v_m^+}^{v_{m+1}^-} dv \int_{w_n^+}^{w_{n+1}^-} dw\ \phi_g(u,v,w), \quad u \in (u_l, u_{l+1})$$

$$J_{gu}^{lmn}(u) = \frac{1}{h_v^m h_w^n}\int_{v_m^+}^{v_{m+1}^-} dv \int_{w_n^+}^{w_{n+1}^-} dw\ J_{gu}(u,v,w),$$

$$L_{gv}^{lmn}(u) = \frac{1}{h_v^m h_w^n}\int_{w_n^+}^{w_{n+1}^-} \left[J_{gv}(u,v_{m+1}^-,w) - J_{gv}(u,v_m^+,w)\right] dw,$$

$$L_{gw}^{lmn}(u) = \frac{1}{h_v^m h_w^n}\int_{v_m^+}^{v_{m+1}^-} \left[J_{gw}(u,v,w_{n+1}^-) - J_{gw}(u,v,w_n^+)\right] dv.$$

Note that the transverse-integrated flux is defined such that the node-averaged flux is preserved

$$\frac{1}{h_u^l}\int_{u_l^+}^{u_{l+1}^-} \phi_{gu}^{lmn}(u)\ du \equiv \bar{\phi}_g^{lmn}.$$

Similarly, we define the transverse-integrated v-directed and w-directed leakages such that the node-averaged leakages are preserved

$$\frac{1}{h_u^l}\int_{u_l^+}^{u_{l+1}^-} L_{gv}^{lmn}(u)\ du \equiv \frac{\bar{L}_{gv}^{lmn}}{h_v^m},$$

$$\frac{1}{h_u^l}\int_{u_l^+}^{u_{l+1}^-} L_{gw}^{lmn}(u)\ du \equiv \frac{\bar{L}_{gw}^{lmn}}{h_w^n}.$$

2.3.2 Polynomial Expansion

The 1D transverse-integrated flux for node (lmn) is approximated by a polynomial of the general form [F1,F2]

$$\phi_{gu}^{lmn}(u) \cong \sum_{n=0}^{N} a_{gun}^{lmn} f_n(u), \quad u \in (u_l, u_{l+1}),\ N \geq 2 \qquad (2\text{-}36)$$

where the basis functions are required to satisfy

$$\frac{1}{h_u^l}\int_{u_l^+}^{u_{l+1}^-} f_n(u)\,du = \begin{cases} 1 & n = 0 \\ 0 & n = 1, \ldots, N . \end{cases} \qquad (2\text{-}37)$$

In addition, the higher-order basis functions ($N \geq 3$) basis functions are required to satisfy the additional constraints,

$$f_n(u_l^+) = f_n(u_{l+1}^-) = 0, \quad n = 3, \ldots, N . \qquad (2\text{-}38)$$

The consequence of these constraints on the higher-order basis functions is that the first three expansion coefficients can be expressed in terms of surface and volume averaged fluxes and that an increase in the order of the polynomial approximation does not change these expressions.

The basis functions for $N \leq 4$ (quartic polynomial or less) are given by:

$$\begin{aligned} f_0(u) &= 1 , \\ f_1(u) &= \frac{u - u_l}{h_u^l} - \frac{1}{2} \equiv \xi - \frac{1}{2} , \\ f_2(u) &= 3\xi^2 - 3\xi + \frac{1}{2} , \\ f_3(u) &= \xi(1 - \xi)(\xi - \frac{1}{2}) , \\ f_4(u) &= \xi(1 - \xi)(\xi^2 - \xi + \frac{1}{5}) . \end{aligned} \qquad (2\text{-}39)$$

The expansion coefficients for the first three terms are obtained from Equation (2-36) in terms of the volume averaged and LHS and RHS homogenized face-averaged fluxes,

$$a_{gu0}^{lmn} = \bar{\phi}_g^{lmn} , \qquad (2\text{-}40a)$$

$$a_{gu1}^{lmn} = \phi_{gu}^{lmn}(u_{l+1}^-) - \phi_{gu}^{lmn}(u_l^+) , \qquad (2\text{-}40b)$$

$$a_{gu2}^{lmn} = \phi_{gu}^{lmn}(u_l^+) + \phi_{gu}^{lmn}(u_{l+1}^-) - 2\bar{\phi}_g^{lmn} . \qquad (2\text{-}40c)$$

Substituting Equations (2-39) and (2-40) into the expansion function yields,

$$\phi_{gu}^{lmn}(u) = \phi_{gu}^{lmn}(u_l^+)\left[3\xi^2 - 4\xi + 1\right] + \phi_{gu}^{lmn}(u_{l+1}^-)\left[3\xi^2 - 2\xi\right] + \bar{\phi}_g^{lmn}\left[6\xi - 6\xi^2\right] + \sum_{n=3}^{N} a_{gun}^{lmn} f_n(u) \; .$$

For a quatric polynomial (N = 4) the flux expansion is

$$\begin{aligned}\phi_{gu}^{lmn}(u) = {} & \phi_{gu}^{lmn}(u_l^+)\left[3\xi^2 - 4\xi + 1\right] + \phi_{gu}^{lmn}(u_{l+1}^-)\left[3\xi^2 - 2\xi\right] + \bar{\phi}_g^{lmn}\left[6\xi - 6\xi^2\right] \\ & + a_{gu3}^{lmn}\left[-\xi^3 + \frac{3}{2}\xi^2 - \frac{1}{2}\xi\right] + a_{gu4}^{lmn}\left[-\xi^4 + 2\xi^3 - \frac{6}{5}\xi^2 + \frac{1}{5}\xi\right] .\end{aligned} \tag{2-41}$$

Substituting the quartic flux expansion, Equation (2-41), into Equation (2-35b) yields the quartic approximation to the homogenized u-directed current

$$\begin{aligned}J_{gu}^{lmn}(u) = - \frac{D_g^{lmn}}{h_u^l}\Big[& \phi_{gu}^{lmn}(u_l^+)\left(6\xi - 4\right) + \phi_{gu}^{lmn}(u_{l+1}^-)\left(6\xi - 2\right) + \bar{\phi}_g^{lmn}\left(6 - 12\xi\right) \\ & + a_{gu3}^{lmn}\left(-3\xi^2 + 3\xi - \frac{1}{2}\right) + a_{gu4}^{lmn}\left(-4\xi^3 + 6\xi^2 - \frac{12}{5}\xi + \frac{1}{5}\right)\Big] .\end{aligned} \tag{2-42}$$

Therefore, the homogenized u-directed current at the node faces are

$$J_{gu}^{lmn}(u_l^+) = - \frac{D_g^{lmn}}{h_u^l}\left[-4\phi_{gu}^{lmn}(u_l^+) - 2\phi_{gu}^{lmn}(u_{l+1}^-) + 6\bar{\phi}_g^{lmn} - \frac{1}{2}a_{gu3}^{lmn} + \frac{1}{5}a_{gu4}^{lmn}\right] , \tag{2-43}$$

$$J_{gu}^{lmn}(u_{l+1}^-) = - \frac{D_g^{lmn}}{h_u^l}\left[2\phi_{gu}^{lmn}(u_l^+) + 4\phi_{gu}^{lmn}(u_{l+1}^-) - 6\bar{\phi}_g^{lmn} - \frac{1}{2}a_{gu3}^{lmn} - \frac{1}{5}a_{gu4}^{lmn}\right] . \tag{2-44}$$

By rearranging Equations (2-43) and (2-44), expressions for the homogenized face-averaged fluxes for node (lmn) can be obtained

$$\phi_{gu}^{lmn}(u_l^+) = \bar{\phi}_g^{lmn} - \frac{1}{4}a_{gu3}^{lmn} + \frac{1}{30}a_{gu4}^{lmn} + \frac{h_u^l}{6D_g^{lmn}}\left[2J_{gu}^{lmn}(u_l^+) + J_{gu}^{lmn}(u_{l+1}^-)\right] , \tag{2-45}$$

$$\phi_{gu}^{lmn}(u_{l+1}^-) = \bar{\phi}_g^{lmn} + \frac{1}{4}a_{gu3}^{lmn} + \frac{1}{30}a_{gu4}^{lmn} - \frac{h_u^l}{6D_g^{lmn}}\left[J_{gu}^{lmn}(u_l^+) + 2J_{gu}^{lmn}(u_{l+1}^-)\right] . \tag{2-46}$$

For $N > 2$, the higher-order coefficients a_{gun}^{lmn}, $n \geq 3$, are determined by applying a weighted residual procedure to the transverse-integrated diffusion equation,

$$\frac{d}{du}J_{gu}^{lmn}(u) + \sum_{g'=1}^{G} A_{gg'}^{lmn}\phi_{g'u}^{lmn}(u) = \frac{1}{\lambda}\sum_{g'=1}^{G} F_{gg'}^{G}\phi_{g'u}^{lmn}(u) + \bar{q}_g^{lmn} - L_{gv}^{lmn}(u) - L_{gw}^{lmn}(u) \; .$$

Rearranging and combining terms yields,

$$\frac{d}{du}J_{gu}^{lmn}(u) + \frac{D_g^{lmn}}{\left(h_u^l\right)^2}\sum_{g'=1}^{G}\left(\kappa^2\right)_{gg'}^{lmn}\phi_{g'u}^{lmn}(u) + S_{gu}^{lmn}(u) - \overline{q}_g^{lmn} = 0\ , \tag{2-47}$$

where,

$$\left(\kappa^2\right)_{gg'}^{lmn} = \frac{\left(h_u^l\right)^2}{D_g^{lmn}}\left[A_{gg'}^{lmn} - \frac{1}{\lambda}F_{gg'}^{lmn}\right], \tag{2-48}$$

$$S_{gu}^{lmn}(u) = L_{gv}^{lmn}(u) + L_{gw}^{lmn}(u)\ . \tag{2-49}$$

Multiplying (2-47) by a weight function $w_n(u)$, $n = 0,\ldots, N - 2$, and then integrating over $u \in (u_l, u_{l+1}|)$ yields the moment equation,

$$\left\langle w_n(u), \frac{d}{du}J_{gu}^{lmn}(u)\right\rangle + \frac{D_g^{lmn}}{\left(h_u^l\right)^2}\sum_{g'=1}^{G}\left(\kappa^2\right)_{gg'}^{lmn}\phi_{g'un}^{lmn}(u) + S_{gun}^{lmn} - q_{gun}^{lmn} = 0\ , \tag{2-50}$$

where the inner products are defined by

$$\left\langle w_n(u), \phi_{gu}^{lmn}(u)\right\rangle \equiv \frac{1}{h_u^l}\int_{u_l^+}^{u_{l+1}^-} w_n(u)\,\phi_{gu}^{lmn}(u)\,du \equiv \phi_{gun}^{lmn}\ , \tag{2-51a}$$

$$\left\langle w_n(u), S_{gu}^{lmn}(u)\right\rangle \equiv S_{gun}^{lmn}\ , \tag{2-51b}$$

$$\left\langle w_n(u), \overline{q}_g^{lmn}\right\rangle \equiv q_{gun}^{lmn}\ . \tag{2-51c}$$

We will use the following weight functions

$$w_1(u) = f_1(u) = \xi - \frac{1}{2},$$
$$w_2(u) = f_2(u) = 3\xi^2 - 3\xi + \frac{1}{2}.$$

Note, also, that weighting with $w_0(u) = 1$ yields the nodal balance equation.

Appendix A presents the derivation of the first and second flux and current moments. From Appendix A the first and second flux moments are

$$\phi_{gu1}^{lmn} = -\frac{1}{12}\phi_{gu}^{lmn}(u_l^+) + \frac{1}{12}\phi_{gu}^{lmn}(u_{l+1}^-) + \frac{1}{120}a_{gu3}^{lmn}\ , \tag{2-52a}$$

$$\phi_{gu2}^{lmn} = \frac{1}{20}\phi_{gu}^{lmn}(u_l^+) + \frac{1}{20}\phi_{gu}^{lmn}(u_{l+1}^-) - \frac{1}{10}\overline{\phi}_g^{lmn} + \frac{1}{700}a_{gu3}^{lmn}\ . \tag{2-52b}$$

And, the first and second current moments are

$$\left\langle w_1(u), \frac{d}{du} J_{gu}^{lmn}(u) \right\rangle = \frac{1}{2h_u^l}\left[J_{gu}^{lmn}(u_{l+1}^-) + J_{gu}^{lmn}(u_l^+)\right] + \frac{D_g^{lmn}}{(h_u^l)^2}\left[\phi_{gu}^{lmn}(u_{l+1}^-) - \phi_{gu}^{lmn}(u_l^+)\right], \tag{2-53a}$$

$$\left\langle w_2(u), \frac{d}{du} J_{gu}^{lmn}(u) \right\rangle = \frac{1}{2h_u^l}\left[J_{gu}^{lmn}(u_{l+1}^-) - J_{gu}^{lmn}(u_l^+)\right] + \frac{3D_g^{lmn}}{(h_u^l)^2}\left[\phi_{gu}^{lmn}(u_l^+) + \phi_{gu}^{lmn}(u_{l+1}^-) - 2\overline{\phi}_g^{lmn}\right]. \tag{2-53b}$$

One of the principle approximations used in nodal methods is the quadratic transverse-leakage approximation [B2]. In this approximation, the u-directed transverse-leakage is expanded as a quadratic polynomial which preserves the node-averaged transverse-leakages in the three adjacent nodes,

$$\begin{aligned} S_{gu}^{lmn}(u) &= \overline{S}_{gu}^{lmn} + \left(\overline{S}_{gu}^{l-1,mn} - \overline{S}_{gu}^{lmn}\right)\rho_{u_l}^{l-1}(u) + \left(\overline{S}_{gu}^{l+1,mn} - \overline{S}_{gu}^{lmn}\right)\rho_{u_l}^{l+1}(u) \\ &= \overline{S}_{gu}^{lmn} + \overline{\Delta S}_{gu-}^{lmn}\,\rho_{u_l}^{l-1}(u) + \overline{\Delta S}_{gu+}^{lmn}\,\rho_{u_l}^{l+1}(u) , \end{aligned} \tag{2-54}$$

where

$$\begin{aligned} \rho_{u_l}^{l-1}(u) &= a_{u_l}^- + b_{u_l}^-\xi + c_{u_l}^-\xi^2 , \\ \rho_{u_l}^{l+1}(u) &= a_{u_l}^+ + b_{u_l}^+\xi + c_{u_l}^+\xi^2 . \end{aligned}$$

The transverse-leakage moments are then given by

$$S_{gun}^{lmn} = \frac{1}{h_u^l}\int_{u_l^+}^{u_{l+1}^-} w_n(u)\, S_{gu}^{lmn}(u)\, du .$$

Using $f_1(u)$ and $f_2(u)$ for the weighting functions, the first and second transverse-leakage moments are given by

$$S_{gu1}^{lmn} = \frac{1}{12}\left[(b_{u_l}^- + c_{u_l}^-)\overline{S}_{gu}^{l-1,mn} - (b_{u_l}^- + b_{u_l}^+ + c_{u_l}^- + c_{u_l}^+)\overline{S}_{gu}^{lmn} + (b_{u_l}^+ + c_{u_l}^+)\overline{S}_{gu}^{l+1,mn}\right], \tag{2-55}$$

$$S_{gu2}^{lmn} = \frac{1}{60}\left[c_{u_l}^-\overline{S}_{gu}^{l-1,mn} - (c_{u_l}^- + c_{u_l}^+)\overline{S}_{gu}^{lmn} + c_{u_l}^+\overline{S}_{gu}^{l+1,mn}\right] \tag{2-56}$$

where

$$a_{u_l}^- = \frac{\frac{1}{2}\left(h_u^l + h_u^{l+1}\right)}{h_u^{l-1} + h_u^l + h_u^{l+1}}\,\frac{2h_u^l}{h_u^{l-1} + h_u^l} ,$$

$$b^-_{u_l} = -\frac{2h^l_u + h^{l+1}_u}{h^{l-1}_u + h^l_u + h^{l+1}_u}\frac{2h^l_u}{h^{l-1}_u + h^l_u},$$

$$c^-_{u_l} = \frac{\frac{3}{2}h^l_u}{h^{l-1}_u + h^l_u + h^{l+1}_u}\frac{2h^l_u}{h^{l-1}_u + h^l_u},$$

$$a^+_{u_l} = -\frac{\frac{1}{2}h^{l-1}_u}{h^{l-1}_u + h^l_u + h^{l+1}_u}\frac{2h^l_u}{h^l_u + h^{l+1}_u},$$

$$b^+_{u_l} = \frac{h^{l-1}_u - h^l_u}{h^{l-1}_u + h^l_u + h^{l+1}_u}\frac{2h^l_u}{h^l_u + h^{l+1}_u},$$

$$c^+_{u_l} = \frac{\frac{3}{2}h^l_u}{h^{l-1}_u + h^l_u + h^{l+1}_u}\frac{2h^l_u}{h^l_u + h^{l+1}_u}.$$

Note that these quadratic expansion coefficient are solely dependent upon the nodal mesh spacings. A more detailed derivation of the transverse-leakage moments, for a number of geometries, is presented in Appendix B. Appendix B also discusses the constraints on the application of the quadratic transverse-leakage approximation.

The only remaining term in the moment equations to be determine is the extraneous neutron source moment. Since we have assumed a homogenized (flat) extraneous neutron source, the extraneous neutron source moment is zero except for unity weighting (the nodal balance equation). Therefore, the extraneous neutron source moment is

$$q^{lmn}_{gun} = \begin{cases} \overline{q}^{lmn}_g & n = 0\,, \\ 0 & n = 1,\ldots,N\text{-}2\,. \end{cases}$$

Substituting Equations (2-52a) and (2-53a) into (2-50) and rearranging yields the first moment equation; and similarly, the second moment equation is obtained by substituting Equations (2-52b) and (2-53b) into (2-50)

$$
\begin{aligned}
&\frac{1}{2h_u^l}\left[J_{gu}^{lmn}(u_{l+1}^-) + J_{gu}^{lmn}(u_l^+)\right] + \frac{D_g^{lmn}}{(h_u^l)^2}\left[\phi_{gu}^{lmn}(u_{l+1}^-) - \phi_{gu}^{lmn}(u_l^+)\right] \\
&+ \frac{D_g^{lmn}}{(h_u^l)^2}\sum_{g'=1}^{G} \left(\kappa^2\right)_{gg'}^{lmn}\left[\frac{1}{12}\phi_{g'u}^{lmn}(u_{l+1}^-) - \frac{1}{12}\phi_{g'u}^{lmn}(u_l^+) + \frac{1}{120}a_{g'u3}^{lmn}\right] \\
&+ S_{gu1}^{lmn} = 0\,,
\end{aligned}
\qquad (2\text{-}57a)
$$

$$
\begin{aligned}
&\frac{1}{2h_u^l}\left[J_{gu}^{lmn}(u_{l+1}^-) - J_{gu}^{lmn}(u_l^+)\right] + \frac{3D_g^{lmn}}{(h_u^l)^2}\left[\phi_{gu}^{lmn}(u_l^+) + \phi_{gu}^{lmn}(u_{l+1}^-) - 2\bar{\phi}_{gu}^{lmn}\right] \\
&+ \frac{D_g^{lmn}}{(h_u^l)^2}\sum_{g'=1}^{G} \left(\kappa^2\right)_{gg'}^{lmn}\left[\frac{1}{20}\phi_{g'u}^{lmn}(u_l^+) + \frac{1}{20}\phi_{g'u}^{lmn}(u_{l+1}^-) - \frac{1}{10}\bar{\phi}_{g'u}^{lmn} + \frac{1}{700}a_{g'u4}^{lmn}\right] \\
&+ S_{gu2}^{lmn} = 0\,.
\end{aligned}
\qquad (2\text{-}57b)
$$

In addition, the following identities will be useful

$$
\phi_{gu}^{lmn}(u_{l+1}^-) - \phi_{gu}^{lmn}(u_l^+) = \frac{1}{2}a_{gu3}^{lmn} - \frac{h_u^l}{2D_g^{lmn}}\left[J_{gu}^{lmn}(u_{l+1}^-) + J_{gu}^{lmn}(u_l^+)\right], \qquad (2\text{-}58a)
$$

$$
\phi_{gu}^{lmn}(u_l^+) + \phi_{gu}^{lmn}(u_{l+1}^-) - 2\bar{\phi}_{gu}^{lmn} = \frac{1}{15}a_{gu4}^{lmn} - \frac{h_u^l}{2D_g^{lmn}}\left[J_{gu}^{lmn}(u_{l+1}^-) - J_{gu}^{lmn}(u_l^+)\right]. \qquad (2\text{-}58b)
$$

Substituting Equations (2-58) into Equations (2-57) and rearranging yields expressions for the third and fourth order nodal expansion coefficients in terms of the homogenized u–directed currents and the transverse-leakage moments:

$$
\begin{aligned}
&a_{gu3}^{lmn} + \frac{1}{10}\sum_{g'=1}^{G} \left(\kappa^2\right)_{gg'}^{lmn} a_{g'u3}^{lmn} = \\
&\frac{1}{12}\sum_{g'=1}^{G} \left(\kappa^2\right)_{gg'}^{lmn} \frac{h_u^l}{D_{g'}^{lmn}}\left[J_{g'u}^{lmn}(u_l^+) + J_{g'u}^{lmn}(u_{l+1}^-)\right] - \frac{2(h_u^l)^2}{D_g^{lmn}}S_{gu1}^{lmn}
\end{aligned}
\qquad (2\text{-}59a)
$$

and

$$
\begin{aligned}
&a_{gu4}^{lmn} + \frac{1}{42}\sum_{g'=1}^{G} \left(\kappa^2\right)_{gg'}^{lmn} a_{g'u4}^{lmn} = \\
&\frac{1}{24}\sum_{g'=1}^{G} \left(\kappa^2\right)_{gg'}^{lmn} \frac{h_u^l}{D_{g'}^{lmn}}\left[J_{g'u}^{lmn}(u_l^+) - J_{g'u}^{lmn}(u_{l+1}^-)\right] - \frac{5(h_u^l)^2}{D_g^{lmn}}S_{gu2}^{lmn}\,.
\end{aligned}
\qquad (2\text{-}59b)
$$

Equations (2-59) are not convenient for numerical reasons, expressions in terms of the heterogeneous u-directed current are preferable. Expressions for the third and forth order nodal expansion coefficients in terms of the heterogeneous u-directed current at u_l and u_{l+1} are obtained by applying the current continuity condition, Equation (2-15),

$$a_{gu3}^{lmn} + \frac{1}{10}\sum_{g'=1}^{G} \left(\kappa^2\right)_{gg'}^{lmn} a_{g'u3}^{lmn} = \frac{1}{12}\sum_{g'=1}^{G} \left(\kappa^2\right)_{gg'}^{lmn} \frac{h_u^l}{D_{g'}^{lmn}}\left[\frac{J_{g'u}^{mn}(u_l)}{f_{g'u,J}^{lmn}(u_l^+)} + \frac{J_{g'u}^{mn}(u_{l+1})}{f_{g'u,J}^{lmn}(u_{l+1}^-)}\right] - \frac{2\left(h_u^l\right)^2}{D_g^{lmn}} S_{gu1}^{lmn} \tag{2-60a}$$

and

$$a_{gu4}^{lmn} + \frac{1}{42}\sum_{g'=1}^{G} \left(\kappa^2\right)_{gg'}^{lmn} a_{g'u4}^{lmn} = \frac{1}{24}\sum_{g'=1}^{G} \left(\kappa^2\right)_{gg'}^{lmn} \frac{h_u^l}{D_{g'}^{lmn}}\left[\frac{J_{g'u}^{mn}(u_l)}{f_{gu,J}^{lmn}(u_l^+)} - \frac{J_{g'u}^{mn}(u_{l+1})}{f_{gu,J}^{lmn}(u_{l+1}^-)}\right] - \frac{5\left(h_u^l\right)^2}{D_g^{lmn}} S_{gu2}^{lmn} . \tag{2-60b}$$

Thus, the determination of the third and fourth order nodal expansion coefficients requires the solution of two G× G linear systems which are dependent upon the mesh, the cross sections, the reactor eigenvalue, the heterogeneous u-directed current, and the transverse-leakage moments.

2.3.3 Nodal Coupling Equation

From the flux expansion, the u-directed homogenized currents for node (lmn) are given by

$$J_{gu}^{lmn}(u_l^+) = -\frac{D_g^{lmn}}{h_u^l}\left[-4\phi_{gu}^{lmn}(u_l^+) - 2\phi_{gu}^{lmn}(u_{l+1}^-) + 6\bar{\phi}_g^{lmn} - \frac{1}{2}a_{gu3}^{lmn} + \frac{1}{5}a_{gu4}^{lmn}\right], \tag{2-43}$$

$$J_{gu}^{lmn}(u_{l+1}^-) = -\frac{D_g^{lmn}}{h_u^l}\left[2\phi_{gu}^{lmn}(u_l^+) + 4\phi_{gu}^{lmn}(u_{l+1}^-) - 6\bar{\phi}_g^{lmn} - \frac{1}{2}a_{gu3}^{lmn} - \frac{1}{5}a_{gu4}^{lmn}\right]. \tag{2-44}$$

In order to eliminate $\phi_{gu}^{lmn}(u_{l+1}^-)$ from $J_{gu}^{lmn}(u_l^+)$ we add 2x(2-43) to (2-44) and subtract $\bar{L}_{gu}^{lmn}$, yielding

$$3J_{gu}^{lmn}(u_l^+) = -\frac{D_g^{lmn}}{h_u^l}\left[-6\phi_{gu}^{lmn}(u_l^+) + 6\bar{\phi}_g^{lmn} - \frac{3}{2}a_{gu3}^{lmn} + \frac{1}{5}a_{gu4}^{lmn}\right] - \bar{L}_{gu}^{lmn}. \tag{2-61}$$

Multiplying the neutron balance equation by h_u^l and rearranging yields

$$-\overline{L}_{gu}^{lmn} = \frac{D_g^{lmn}}{h_u^l} \sum_{g'=1}^{G} \left(\kappa^2\right)_{gg'}^{lmn} \overline{\phi}_{g'}^{lmn} + h_u^l \overline{S}_{gu}^{lmn} - h_u^l \overline{q}_g^{lmn}. \tag{2-62}$$

And, substituting (2-62) into (2-61) yields

$$\begin{aligned} 3J_{gu}^{lmn}(u_l^+) = &- \frac{D_g^{lmn}}{h_u^l}\left[-6\phi_{gu}^{lmn}(u_l^+) + 6\overline{\phi}_g^{lmn} - \frac{3}{2}a_{gu3}^{lmn} + \frac{1}{5}a_{gu4}^{lmn}\right] \\ &+ \frac{D_g^{lmn}}{h_u^l} \sum_{g'=1}^{G} \left(\kappa^2\right)_{gg'}^{lmn} \overline{\phi}_{g'}^{lmn} + h_u^l \overline{S}_{gu}^{lmn} - h_u^l \overline{q}_g^{lmn}. \end{aligned} \tag{2-63}$$

For node (l-1,mn) the u-directed currents are

$$J_{gu}^{l-1,mn}(u_{l-1}^+) = -\frac{D_g^{l-1,mn}}{h_u^{l-1}}\left[-4\phi_{gu}^{l-1,mn}(u_{l-1}^+) - 2\phi_{gu}^{l-1,mn}(u_l^-) + 6\overline{\phi}_g^{l-1,mn} - \frac{1}{2}a_{gu3}^{l-1,mn} + \frac{1}{5}a_{gu4}^{l-1,mn}\right], \tag{2-64}$$

$$J_{gu}^{l-1,mn}(u_l^-) = -\frac{D_g^{l-1,mn}}{h_u^{l-1}}\left[2\phi_{gu}^{l-1,mn}(u_{l-1}^+) + 4\phi_{gu}^{l-1,mn}(u_l^-) - 6\overline{\phi}_g^{l-1,mn} - \frac{1}{2}a_{gu3}^{l-1,mn} - \frac{1}{5}a_{gu4}^{l-1,mn}\right]. \tag{2-65}$$

Next we obtain an expression for $J_{gu}^{l-1,mn}(u_l^-)$ in which $\phi_{gu}^{l-1,mn}(u_{l-1}^+)$ has been eliminated by adding 2× (2-65) to (2-64) and add the u-directed leakage for node (l-1,mn)

$$\begin{aligned} 3J_{gu}^{l-1,mn}(u_l^-) = &- \frac{D_g^{l-1,mn}}{h_u^{l-1}}\left[6\phi_{gu}^{l-1,mn}(u_l^-) - 6\overline{\phi}_g^{l-1,mn} - \frac{3}{2}a_{gu3}^{l-1,mn} - \frac{1}{5}a_{gu4}^{l-1,mn}\right] \\ &- \frac{D_g^{l-1,mn}}{h_u^{l-1}} \sum_{g'=1}^{G} \left(\kappa^2\right)_{gg'}^{l-1,mn} \overline{\phi}_{g'}^{l-1,mn} - h_u^{l-1} \overline{S}_{gu}^{l-1,mn} + h_u^{l-1} \overline{q}_g^{l-1,mn}. \end{aligned} \tag{2-66}$$

Multiplying (2-63) by $\frac{h_u^l}{D_g^{lmn}} r_{gu,\phi}^{lmn}(u_l)$, adding (2-66) multiplied by $\frac{h_u^{l-1}}{D_g^{l-1mn}}$, and rearranging yields the u-directed nodal coupling equation for node (lmn)

$$
\begin{aligned}
J_{gu}^{mn}(u_l) &= \left[\frac{3h_u^{l-1}}{D_g^{l-1,mn}} \frac{1}{f_{gu,J}^{l-1,mn}(u_l^-)} + \frac{3h_u^l}{D_g^{lmn}} \frac{r_{gu,J}^{lmn}(u_l)}{f_{gu,J}^{lmn}(u_l^+)} \right]^{-1} \times \\
&\left\{ \left[6\overline{\phi}_g^{l-1,mn} + \frac{3}{2} a_{gu3}^{l-1,mn} + \frac{1}{5} a_{gu4}^{l-1,mn} \right] - r_{gu,\phi}^{lmn}(u_l) \left[6\overline{\phi}_g^{lmn} - \frac{3}{2} a_{gu3}^{lmn} + \frac{1}{5} a_{gu4}^{lmn} \right] \right. \\
&- \sum_{g'=1}^{G} \left(\kappa^2\right)_{gg'}^{l-1,mn} \overline{\phi}_{g'}^{l-1,mn} + r_{gu,\phi}^{lmn}(u_l) \sum_{g'=1}^{G} \left(\kappa^2\right)_{gg'}^{lmn} \overline{\phi}_{g'}^{lmn} \\
&\left. - \frac{(h_u^{l-1})^2}{D_g^{l-1,mn}} \left[\overline{S}_{gu}^{l-1,mn} + \overline{q}_g^{l-1,mn} \right] + r_{gu,\phi}^{lmn}(u_l) \frac{(h_u^{l-1})^2}{D_g^{l-1,mn}} \left[\overline{S}_{gu}^{lmn} - \overline{q}_g^{lmn} \right] \right\} .
\end{aligned}
\tag{2-67}
$$

2.3.3.1 Boundary Conditions

Rearranging Equations (2-63) and (2-66), the homogenized u-directed current on the left and right faces of node (lmn) are

$$
\begin{aligned}
J_{gu}^{lmn}(u_l^+) = &- \frac{2D_g^{lmn}}{h_u^l} \left[-\phi_{gu}^{lmn}(u_l^+) + \overline{\phi}_g^{lmn} - \frac{1}{4} a_{gu3}^{lmn} + \frac{1}{30} a_{gu4}^{lmn} \right] \\
&+ \frac{D_g^{lmn}}{3h_u^l} \sum_{g'=1}^{G} \left(\kappa^2\right)_{gg'}^{lmn} \overline{\phi}_{g'}^{lmn} + \frac{h_u^l}{3} \left[\overline{S}_{gu}^{lmn} - \overline{q}_g^{lmn} \right] ,
\end{aligned}
\tag{2-68}
$$

$$
\begin{aligned}
J_{gu}^{lmn}(u_{l+1}^-) = &- \frac{2D_g^{lmn}}{h_u^l} \left[\phi_{gu}^{lmn}(u_{l+1}^-) - \overline{\phi}_g^{lmn} - \frac{1}{4} a_{gu3}^{lmn} - \frac{1}{30} a_{gu4}^{lmn} \right] \\
&- \frac{D_g^{lmn}}{3h_u^l} \sum_{g'=1}^{G} \left(\kappa^2\right)_{gg'}^{lmn} \overline{\phi}_{g'}^{lmn} - \frac{h_u^l}{3} \left[\overline{S}_{gu}^{lmn} + \overline{q}_g^{lmn} \right] .
\end{aligned}
\tag{2-69}
$$

Using the general external reactor boundary condition, Equation (2-30), the LHS boundary condition is

$$
\phi_{gu}^{mn}(u_l) = - \Gamma_{gu-}^{mn} J_{gu}^{mn}(u_l) .
\tag{2-70}
$$

Substituting (2-70) into (2-68), applying the flux and current continuity conditions, and rearranging yields the LHS nodal coupling equation

$$
\begin{aligned}
J_{gu}^{mn}(u_l) = &\left[\frac{3h_u^l}{D_g^{lmn}} \frac{1}{f_{gu,J}^{lmn}(u_l^+)} + \frac{6\Gamma_{gu-}^{mn}}{f_{gu,\phi}^{lmn}(u_l^+)} \right]^{-1} \times \left\{ \left[-6\overline{\phi}_g^{lmn} + \frac{3}{2} a_{gu3}^{lmn} - \frac{1}{5} a_{gu4}^{lmn} \right] \right. \\
&\left. + \sum_{g'=1}^{G} \left(\kappa^2\right)_{gg'}^{lmn} \overline{\phi}_{g'}^{lmn} + \frac{(h_u^l)^2}{D_g^{lmn}} \left[\overline{S}_{gu}^{lmn} - \overline{q}_g^{lmn} \right] \right\} .
\end{aligned}
\tag{2-71}
$$

Similarly, the RHS external boundary condition for node (lmn) is

$$\phi_{gu}^{mn}(u_{l+1}) = \Gamma_{gu+}^{mn} J_{gu}^{mn}(u_{l+1}) \; . \tag{2-72}$$

Substituting (2-72) into (2-69), applying the flux and current continuity condition, and rearranging yields the RHS nodal coupling equation

$$J_{gu}^{mn}(u_{l+1}) = \left[\frac{3h_u^l}{D_g^{lmn}} \frac{1}{f_{gu,J}^{lmn}(u_{l+1}^-)} + \frac{6\Gamma_{gu+}^{mn}}{f_{gu,\phi}^{lmn}(u_{l+1}^-)} \right]^{-1} \times \left\{ \left[6\overline{\phi}_g^{lmn} + \frac{3}{2} a_{gu3}^{lmn} + \frac{1}{5} a_{gu4}^{lmn} \right] - \sum_{g'=1}^{G} \left(\kappa^2\right)_{gg'}^{lmn} \overline{\phi}_{g'}^{lmn} - \frac{(h_u^l)^2}{D_g^{lmn}} \left[\overline{S}_{gu}^{lmn} - \overline{q}_g^{lmn} \right] \right\} . \tag{2-73}$$

2.3.4 CMFD Discontinuity Factor Ratios

In general, CMFD discontinuity factor ratios may be defined which will permit the CMFD method to reproduce any reference solution [H3]. The CMFD discontinuity factor ratios are in effect correction factors for the CMFD method which provide the additional degrees of freedom which are required in order to match the reference solution. We will used the polynomial nodal method to specify the nodal coupling equation, the reference solution, which will then be used to determine CMFD discontinuity factor ratios. With these CMFD discontinuity factor ratios we may use the CMFD method as the computational engine of our nodal method while retaining the higher-order accuracy of the polynomial nodal method.

We may obtain an expression for the CMFD discontinuity factor ratios at node faces in the interior of the reactor in terms of node-averaged fluxes and heterogeneous face-averaged currents by rearranging Equation (2-17)

$$r_{gu}^{mn}(u_l) = \frac{f_{gu,\phi}^{l-1,mn}(u_l^-)}{f_{gu,\phi}^{lmn}(u_l^+)} \frac{\left[\overline{\phi}_g^{l-1,mn} - \frac{h_u^{l-1}}{2D_g^{l-1,mn}} \frac{J_{gu}^{mn}(u_l)}{f_{gu,J}^{l-1,mn}(u_l^-)} \right]}{\left[\overline{\phi}_g^{lmn} + \frac{h_u^l}{2D_g^{lmn}} \frac{J_{gu}^{mn}(u_l)}{f_{gu,J}^{lmn}(u_l^+)} \right]} . \tag{2-29}$$

In this expression the nodal coupling equation, Equation (2-67), should be used to provide the heterogeneous face-averaged current.

Since CMFD discontinuity factor ratios are not defined at reactor boundaries, different expressions must be used. The CMFD discontinuity factor term at the LHS reactor boundary is given by

$$\frac{\Gamma^{mn}_{gu-}}{f^{lmn}_{gu}(u_l^+)} = - f^{lmn}_{gu,\phi}(u_l^+)\left[\frac{\bar{\phi}^{lmn}_g}{J^{mn}_{gu}(u_l)} + \frac{1}{f^{lmn}_{gu,J}(u_l^+)}\frac{h^l_u}{2D^{lmn}_g}\right], \tag{2-32}$$

where Equation (2-71) is used to provide the heterogeneous face-averaged current at u_l. Similary, the CMFD discontinuity factor term at the RHS reactor boundary is given by

$$\frac{\Gamma^{mn}_{gu+}}{f^{lmn}_{gu}(u^-_{l+1})} = f^{lmn}_{gu,\phi}(u^-_{l+1})\left[\frac{\bar{\phi}^{lmn}_g}{J^{mn}_{gu}(u_{l+1})} - \frac{1}{f^{lmn}_{gu,J}(u^-_{l+1})}\frac{h^l_u}{2D^{lmn}_g}\right], \tag{2-34}$$

where Equation (2-73) is used to provide the heterogeneous face-averaged current at u_{l+1}.

2.4 SUMMARY

In this chapter two numerical methods for solving the static neutron diffusion equation with an extraneous neutron source were derived. Both of these methods permit discontinuities in the face-averaged flux and the face-averaged current at nodal interfaces in order to accommodate new bilinear weighting schemes. First a coarse mesh finite-difference (CMFD) method with flux and current discontinuity factors was derived. Next CMFD discontinuity factor ratios which permit the CMFD method to reproduce a reference solution were defined. Then a polynomial nodal method with flux and current discontinuity factors was derived. Finally, a procedure for obtaining CMFD discontinuity factor ratios using the polynomial nodal method was described.

CHAPTER 3

NUMERICAL CONSIDERATIONS

3.1 INTRODUCTION

In Chapter 2 the CMFD method and a polynomial nodal method, both of which permit discontinuities in the face-averaged flux and current, were derived. In addition, a procedure in which correction factors for the CMFD method (CMFD discontinuity factor ratios) may be determined using the polynomial nodal method was described. The combination of the CMFD method and the procedure for determining the CMFD discontinuity factor ratios results in a hybrid nodal method in which the CMFD method is the computational engine.

In this chapter the numerical properties of the nonlinear iteration scheme used to by this nodal method will be discussed. The iteration strategies used for eigenvalue and source problems will be described. Initially, iterative methods in which all the energy groups are solved simultaneously will be discussed in order to illuminate the numerical properties and behavior of the groupwise methods which will actually be used. The groupwise iterative methods used to solve the eigenvalue and source problems will be developed and described in detail. Finally, issues related to the optimization of the iterative procedure will be discussed.

3.2 NUMERICAL PROPERTIES

The CMFD balance equation, Equation (2-28), can be expressed in a more compact finite-difference-like matrix equation

$$\mathbf{M}(\boldsymbol{\phi},\lambda)\boldsymbol{\phi} = \frac{1}{\lambda}\mathbf{F}\boldsymbol{\phi} + \mathbf{q} \,, \tag{3-1}$$

where,

$\mathbf{M}(\boldsymbol{\phi},\lambda)$ = matrix of dimension (N*G)×(N*G) containing the absorption, scattering, and diffusion terms
$\mathbf{F}$ = matrix of dimension (N*G)×(N*G) containing the fission source terms
$\boldsymbol{\phi}$ = vector of length (N*G) node-averaged fluxes
$\mathbf{q}$ = vector of length (N*G) containing the extraneous neutron source terms
λ = eigenvalue
N = number of nodes
G = number of energy groups.

Note that in the general case the matrix $\mathbf{M}(\boldsymbol{\phi},\lambda)$ depends on the flux and eigenvalue, therefore, the equation is nonlinear. This nonlinearity is introduced through the CMFD discontinuity factor ratios, which are dependent on both the flux and the eigenvalue. Note that if the flux discontinuity factor ratios, current discontinuity factor ratios, and CMFD discontinuity factor ratios are equal to unity then Equation (3-1) reduces to mesh-centered finite difference form of the neutron diffusion equation.

For eigenvalue problems we are interested in solving

$$\mathbf{M}(\boldsymbol{\phi},\lambda)\boldsymbol{\phi} = \frac{1}{\lambda}\mathbf{F}\boldsymbol{\phi} . \tag{3-2}$$

In general, the only properties of $\mathbf{M}(\boldsymbol{\phi},\lambda)$ that we can guarantee is that it is real and irreducible. If any of the discontinuity factor ratios are not equal to unity then $\mathbf{M}(\boldsymbol{\phi},\lambda)$ becomes nonsymmetric. Diagonal dominance may be guaranteed if the diffusion coefficients, the current discontinuity factor ratios, and the product of the flux and CMFD discontinuity factor ratios are positive and bounded [A1]:

$$0 < D_g^{lmn} < \infty ,$$

$$0 < r_{gu,J}^{mn}(u_l) < \infty ,$$

$$0 < r_{gu,\phi}^{mn}(u_l)\, r_{gu}^{mn}(u_l) < \infty .$$

If diagonal dominance is preserved the convergence and stability properties of the iterative solution to Equation (3–2) are guaranteed.

Aragonés and Ahnert [A1] have shown that diagonal dominance may be imposed by adjusting the diffusion coefficients, forcing the discontinuity factor ratios to be positive and bounded. Since, in our derivation, the flux and current discontinuity factor ratios are homogenization parameters this procedure may only be applied to the product of the flux and CMFD discontinuity factor ratios,

$$r_{gu,\phi}^{mn}(u_l)\,r_{gu}^{mn}(u_l) = \frac{\left[\bar{\phi}_g^{l-1,mn} - \frac{h_u^{l-1}}{2D_g^{l-1,mn}}\frac{J_{gu}^{mn}(u_l)}{f_{gu,J}^{l-1,mn}(u_l^-)}\right]}{\left[\bar{\phi}_g^{lmn} + \frac{h_u^{l}}{2D_g^{lmn}}\frac{J_{gu}^{mn}(u_l)}{f_{gu,J}^{lmn}(u_l^+)}\right]} .$$

Diagonal dominance may be imposed by requiring the diffusion coefficients to satisfy the following stability condition,

$$D_g^{lmn} > \frac{h_u^l}{2\bar{\phi}_g^{lmn}}\max\left(-\frac{J_{gu}^{mn}(u_l)}{f_{gu,J}^{lmn}(u_l^+)}, \frac{J_{gu}^{mn}(u_{l+1})}{f_{gu,J}^{lmn}(u_{l+1}^-)}\right) .$$

If this stability condition is not satisfied the diffusion coefficient is arbitrarily increased until it is satisfied. These modified diffusion coefficients are then used in the CMFD balance equation, Equation (2-28), and to calculate the CMFD discontinuity factor ratios, Equation (2-29). The modified diffusion coefficients and CMFD discontinuity factor ratios permit the preservation of the nodal leakage rates while imposing diagonal dominance.

In the limit of infinitely fine mesh spacing all of the discontinuity factor ratios will approach unity. In this case, Equation (3-2) reduces to the mesh-centered finite difference approximation to the neutron diffusion equation and **M** will have the following properties:

1. Real
2. Irreducible
3. Symmetric
4. Diagonally dominant.

Therefore, in the limit of infinitely fine mesh spacing Equation (3-2) will have the following properties [W1]:

1. There will exist a unique real positive eigenvalue, λ_1, which is greater in modulus than all other eigenvalues.
2. The eigenvector corresponding to the eigenvalue λ_1 will be unique and positive.

Thus, in the limit of infinitely fine mesh spacing Equation (3-2) is guaranteed to converge to the exact solution of the neutron diffusion equation [W1]. For larger mesh spacings this behavior is guaranteed only if the product of the flux and CMFD discontinuity factor ratios are positive and bounded, and forcing them to be positive and bounded may require arbitrary changes in the group-diffusion coefficient.

For source problems we are interested in solving

$$\left[\mathbf{M}(\boldsymbol{\phi},\lambda) - \frac{1}{\lambda}\mathbf{F}\right]\boldsymbol{\phi} = \mathbf{q}\ . \tag{3-3}$$

In general, the numerical characteristics of Equation (3-3) are unknown since, as in the case of eigenvalue problems, the only properties of the matrix $\left[\mathbf{M}(\boldsymbol{\phi},\lambda) - \frac{1}{\lambda}\mathbf{F}\right]$ that we can guarantee is that it is real and irreducible. As with eigenvalue problems diagonal dominance may be imposed using the Aragonés and Ahnert procedure [A1]. However, in the limit of infinitely fine mesh spacing we know that the discontinuity factor ratios will approach unity and that Equation (3-3) will approach the exact solution of the neutron diffusion equation.

3.3 ITERATION STRATEGIES FOR EIGENVALUE PROBLEMS

3.3.1 Outer Iterations

The power method [W1] is the simplest method for solving the eigenvalue problem represented by Equation (3-2). The power method algorithm for this problem is

$$\boldsymbol{\phi}^{(p+1)} = \left[\mathbf{M}(\boldsymbol{\phi}^{(p)},\lambda^{(p)})\right]^{-1} \frac{1}{\lambda^{(p)}} \mathbf{F}\boldsymbol{\phi}^{(p)} \tag{3-4a}$$

$$\lambda^{(p+1)} = \lambda^{(p)} \frac{\left(1,\ \mathbf{F}\boldsymbol{\phi}^{(p+1)}\right)}{\left(1,\ \mathbf{F}\boldsymbol{\phi}^{(p)}\right)}, \tag{3-4b}$$

where p is the outer iteration index. Outer iterations are used to calculate the fission source, $(1/\lambda)\mathbf{F}\boldsymbol{\phi}$, and the eigenvalue, λ. Inner iterations are used to invert the matrix $\mathbf{M}(\boldsymbol{\phi},\lambda)$. The nonlinearity in this problem is handled by computing the matrix $\mathbf{M}(\boldsymbol{\phi},\lambda)$ using the solution from the previous iteration. However, the convergence rate of the power method is undesirably slow. This is because successive calculations of the fission source, $(1/\lambda)\mathbf{F}\boldsymbol{\phi}$, vary in the asymptotic limit by an amount governed by the dominance ratio

$$d = \left|\frac{\lambda_2}{\lambda_1}\right|,$$

where λ_1 and λ_2 are the fundamental and first harmonic eigenvalues, respectively, of the matrix $\left[\mathbf{M}(\boldsymbol{\phi},\lambda)\right]^{-1}\mathbf{F}$. This ratio, which in general varies from iteration to iteration, will be close to unity for most problems, resulting in slow convergence.

Wielandt's method of fractional iteration [W1,S2], or eigenvalue shifting, is one method for accelerating the convergence of outer iterations. It accelerates the convergence of the outer iterations by effectively reducing the dominance ratio. Wielandt's method is derived by subtracting $(1/\lambda')\mathbf{F}\boldsymbol{\phi}$ from both sides of Equation (3-2), where λ' is the eigenvalue shift,

$$\left[\mathbf{M}(\boldsymbol{\phi},\lambda) - \frac{1}{\lambda'}\mathbf{F}\right]\boldsymbol{\phi} = \frac{1}{\Lambda}\mathbf{F}\boldsymbol{\phi},$$

and

$$\frac{1}{\Lambda} = \frac{1}{\lambda} - \frac{1}{\lambda'}.$$

The iteration algorithm for Wielandt's method of fractional iteration is

$$\boldsymbol{\phi}^{(p+1)} = \left[\mathbf{M}(\boldsymbol{\phi}^{(p)},\lambda^{(p)}) - \frac{1}{\lambda'}\mathbf{F}\right]^{-1}\frac{1}{\Lambda^{(p)}}\mathbf{F}\boldsymbol{\phi}^{(p)} \tag{3-5a}$$

$$\Lambda^{(p+1)} = \Lambda^{(p)}\frac{\left(1,\,\mathbf{F}\boldsymbol{\phi}^{(p+1)}\right)}{\left(1,\,\mathbf{F}\boldsymbol{\phi}^{(p)}\right)} \tag{3-5b}$$

$$\lambda^{(p+1)} = \frac{\Lambda^{(p+1)}\lambda'}{\Lambda^{(p+1)} + \lambda'}. \tag{3-5c}$$

Note that Wielandt's method requires all of the energy groups to be solved simultaneously. If $1/\lambda'$ is closer to $1/\lambda_1$, than to $1/\lambda_2$, the converged eigenvalue and eigenvector obtained using Equations (3-5) will be identical to that obtained using the power method. In general, since λ_1 will vary throughout the outer iterations, λ' is required to be greater than the largest λ_1. The shifted dominance ratio is given by

$$d_s = \left|\frac{\frac{1}{\lambda_1} - \frac{1}{\lambda'}}{\frac{1}{\lambda_2} - \frac{1}{\lambda'}}\right|,$$

which is clearly smaller than the unshifted dominance ratio if $\lambda' \geq \lambda_1$. Therefore, the convergence of the outer iterations will be accelerated using Wielandt's method. The power method may be obtained from Equations (3-5) by setting the eigenvalue shift, λ', equal to infinity.

There are several important differences between the numerical behavior of the Wielandt method as applied to nodal methods and as applied to finite difference equations. These differences are due to the nonlinear nature of the iteration matrix $\left[\mathbf{M}(\boldsymbol{\phi},\lambda) - \frac{1}{\lambda'}\mathbf{F}\right]^{-1}\frac{1}{\Lambda}\mathbf{F}$. Since the $\mathbf{M}(\boldsymbol{\phi},\lambda)$ matrix depends on the flux solution from the previous iteration, the eigenvalue spectrum of the iteration matrix will change every time

$\mathbf{M}(\phi,\lambda)$ is recomputed. Sutton [S8] found that there can be substantial variations in the fundamental eigenvalue of the iteration matrix as the problem converges. He also found that the net rate of convergence of the Wielandt method was determined by two processes: the rate of convergence of the fission source to the fundamental mode of the iteration matrix, and the rate of convergence of the iteration matrix to one with the same fundamental eigenvalue as the diffusion equation. Only the first of these processes is directly accelerated by the Wielandt method.

The nonlinearity of the problem has several implications on the performance of the Wielandt method. First, it is not possible, in general, to apply a single value of the eigenvalue shift throughout the iteration process that will lead to convergence in a few iterations. This is because the choice of the eigenvalue shift that makes the dominance ratio small early in the iteration may lead to much larger dominance ratios as the problem converges. This is not true of the finite difference equations where the fundamental eigenvalue of the iteration matrix is constant and equal to the converged eigenvalue. In this case, the rate of convergence is due solely to how close the eigenvalue shift, λ', is to the converged eigenvalue, and in the absence of roundoff the number of iterations required to converge the problem approaches one as the difference between λ' and the converged eigenvalue approaches zero. It is not possible to use an eigenvalue shift equal to the converged eigenvalue because the matrix to be inverted in Equation (3-5a) would then become singular. The optimal strategy for handling the nonlinearity present in nodal methods would be to chose a value of λ' at each outer iteration close to the fundamental eigenvalue of the iteration matrix for that iteration. This is not strictly possible because the fundamental eigenvalue of the iteration matrix for the current iteration is not known. However, this optimal strategy may be approximated by setting the eigenvalue shift to a fixed value that minimizes the dominance ratio early in the iteration process and, as the problem converges, by then setting the eigenvalue shift close to the eigenvalue calculated during the previous iteration,

$$\lambda' = \lambda^{(p)} + \delta\lambda\,.$$

The above discussion assumes the simultaneous solution of Equation (3-2) for all the energy groups. However, it will be more convenient to solve Equation (3-2) one group at at time. The groupwise form of Equation (3-2) is,

$$\mathbf{N}_g(\boldsymbol{\phi},\lambda)\boldsymbol{\phi}_g = \frac{1}{\lambda}\sum_{g'=1}^{G} \mathbf{F}_{gg'}\boldsymbol{\phi}_{g'} + \sum_{g'\neq g} \boldsymbol{\Sigma}_{gg'}\boldsymbol{\phi}_{g'}, \quad g=1,\ldots,G \tag{3-6}$$

where,

$\mathbf{N}_g(\boldsymbol{\phi},\lambda)$ = N×N matrix containing diffusion, total cross section, and g→g scattering cross section terms for group g

$\mathbf{F}_{gg'}$ = N×N diagonal matrix containing the fission source terms from group g' to group g

$\boldsymbol{\Sigma}_{gg'}$ = N×N diagonal matrix containing the scattering terms from group g' to group g

$\boldsymbol{\phi}_g$ = vector of length N containing the group g node-averaged fluxes.

As we have previously discussed, the power method is the simplest technique for solving Equation (3-6). The groupwise version of the power method algorithm is

$$\boldsymbol{\phi}_g^{(p+1)} = \left[\mathbf{N}_g(\boldsymbol{\phi}^{(p)},\lambda^{(p)})\right]^{-1} \times \left\{\frac{1}{\lambda}\sum_{g'=1}^{G} \mathbf{F}_{gg'}\boldsymbol{\phi}_{g'}^{(p)} + \sum_{g'\neq g} \boldsymbol{\Sigma}_{gg'}\boldsymbol{\phi}_{g'}^{(p)}\right\}, \quad g=1,\ldots,G \tag{3-7a}$$

$$\lambda^{(p+1)} = \lambda^{(p)}\frac{\left(1,\,\mathbf{F}\boldsymbol{\phi}^{(p+1)}\right)}{\left(1,\,\mathbf{F}\boldsymbol{\phi}^{(p)}\right)}, \tag{3-7b}$$

where p is the outer iteration index.

The rigorous implementation of Wielandt's method requires the simultaneous solution of all the energy groups. However, Sutton [S8] has developed a nonrigorous version of Wielandt's method of fractional iteration. In order to derive Sutton's groupwise version of Wielandt's method we must introduce the $\mathbf{A}_{g'g}$ matrix which is defined as follows:

$\mathbf{A}_{g'g}$ ≡ N×N diagonal matrix containing the ratios $\phi_{g'}/\phi_g$ for each node as the diagonal elements.

$= \left[\mathbf{I}\boldsymbol{\phi}_g\right]^{-1}\boldsymbol{\phi}_{g'}$.

Then the groupwise version of Wielandt's method of fractional iteration is

$$\left[\mathbf{N}_g(\boldsymbol{\phi},\lambda) - \frac{1}{\lambda'}\sum_{g'=1}^{G} \mathbf{F}_{gg'}\mathbf{A}_{g'g}\right]\boldsymbol{\phi}_g = \frac{1}{\Lambda}\sum_{g'=1}^{G} \mathbf{F}_{gg'}\boldsymbol{\phi}_{g'} + \sum_{g'\neq g} \Sigma_{gg'}\boldsymbol{\phi}_{g'} . \tag{3-8}$$

As before, the matrices $\mathbf{N}_g(\boldsymbol{\phi}, \lambda)$ and $\mathbf{A}_{g'g}$ are computed based on the solution from the previous iteration. Also, note that as the problem converges, the rigorous Wielandt method is regained. The groupwise version of the Wielandt method algorithm is

$$\boldsymbol{\phi}_g^{(p+1)} = \left[\mathbf{N}_g(\boldsymbol{\phi}^{(p)},\lambda^{(p)}) - \frac{1}{\lambda'}\sum_{g'=1}^{G} \mathbf{F}_{gg'}\mathbf{A}_{g'g}^{(p)}\right]^{-1} \times \left\{\frac{1}{\Lambda^{(p)}}\sum_{g'=1}^{G} \mathbf{F}_{gg'}\boldsymbol{\phi}_{g'}^{(p)} + \sum_{g'\neq g} \Sigma_{gg'}\boldsymbol{\phi}_{g'}^{(p)}\right\} \tag{3-9a}$$

$$\Lambda^{(p+1)} = \Lambda^{(p)}\frac{\left(1, \mathbf{F}\boldsymbol{\phi}^{(p+1)}\right)}{\left(1, \mathbf{F}\boldsymbol{\phi}^{(p)}\right)} \tag{3-9b}$$

$$\lambda^{(p+1)} = \frac{\Lambda^{(p+1)}\lambda'}{\Lambda^{(p+1)} + \lambda'} . \tag{3-9c}$$

The iteration algorithm described by Equations (3-9) contains three nested levels of iteration. In the outer iteration the fission source $(1/\Lambda)\mathbf{F}\boldsymbol{\phi}$ is calculated using the flux from the previous iteration, and Λ and λ are calculated using the results from the current inner iterations. The inner iterations are used to update the $\mathbf{N}_g(\boldsymbol{\phi},\lambda)$ and $\mathbf{A}_{g'g}$ matrices using the results from the previous iteration. For each inner iteration the nodal coupling equations are solved and the CMFD discontinuity factor ratios are determined in order to update the $\mathbf{N}_g(\boldsymbol{\phi},\lambda)$ matrices. Also the fission plus scattering source is determined for the flux iterations. The inner most level of iteration, the flux iterations, are used to invert the matrix $\left[\mathbf{N}_g(\boldsymbol{\phi},\lambda) - \frac{1}{\lambda'}\sum_{g'=1}^{G} \mathbf{F}_{gg'}\mathbf{A}_{g'g}\right]$ for each energy group.

3.3.2 Inner Iterations

Inner iterations are used to update the $\mathbf{N}_g$ and $\mathbf{A}_{g'g}$ matrices in order to account for the nonlinearity present in Equation (3-8). First a polynomial nodal method calculation is performed to update the face-averaged heterogeneous currents. Using the updated currents the CMFD discontinuity factor ratios may be determined. With the recently updated CMFD discontinuity factor ratios the $\mathbf{N}_g$ matrix may be calculated, and using the group fluxes from the previous iteration the $\mathbf{A}_{g'g}$ matrices may be calculated. The detailed calculation procedure used during the inner iterations is as follows:

1. Face-averaged heterogeneous currents are updated using the CMFD coupling equation (2-20) and the flux from the previous iteration.
2. The higher-order expansion coefficients, a_{gu3} and a_{gu4}, are calculated using Equations (2-60) and the updated heterogeneous currents.
3. The heterogeneous currents are updated again this time using the nodal coupling equation (2-67).
4. The CMFD discontinuity factor ratios are updated using Equation (2-29).
5. The matrix $\mathbf{N}_g(\boldsymbol{\phi}^{(p,q)}, \lambda^{(p)})$ is calculated using the recently updated CMFD discontinuity factor ratios, and the $\mathbf{A}^{(p,q)}_{g'g}$ matrices are calculated using the group fluxes from the previous iteration.
6. The node-averaged group flux vectors are updated through a series of flux iterations. The following matrix problems are solved iteratively,

$$\left[\mathbf{N}_g(\boldsymbol{\phi}^{(p,q)}, \lambda^{(p)}) - \frac{1}{\lambda'}\sum_{g'=1}^{G} \mathbf{F}_{gg'}\mathbf{A}^{(p,q)}_{g'g}\right]\boldsymbol{\phi}_g^{(p,q+1)} =$$
$$\left\{\frac{1}{\Lambda^{(p)}}\sum_{g'=1}^{G} \mathbf{F}_{gg'}\boldsymbol{\phi}_{g'}^{(p)} + \sum_{g'=1}^{g-1} \Sigma_{gg'}\boldsymbol{\phi}_{g'}^{(p,q+1)} + \sum_{g'=g+1}^{G} \Sigma_{gg'}\boldsymbol{\phi}_{g'}^{(p,q)}\right\},\quad g = 1,\ldots,G \tag{3-10}$$

where p and q are the outer and inner iteration indices respectively. Note that upscattering is not explicitly treated during the flux iterations. However, by performing a series of inner or outer iterations upscattering may be adequately modelled.

3.3.3 Flux Iterations

Equation (3-10) is solved using either the Gauss-Seidel (G-S) method or the cyclic Chebyshev semi-iterative (CCSI) method [H1]. CCSI is a variant of the block successive overrelaxation (SOR) method in which the relaxation parameter is varied every iteration in such a way that the average rate of convergence is increased.

During the flux iterations we are actually solving a matrix problem of the form $\mathbf{Au} = \mathbf{b}$ where

$$\mathbf{A} = \mathbf{N}_g(\phi^{(p,q)},\lambda^{(p)}) - \frac{1}{\lambda'}\sum_{g'=1}^{G} \mathbf{F}_{gg'}\mathbf{A}_{g'g}^{(p,q)} \tag{3-11a}$$

$$\mathbf{b} = \frac{1}{\Lambda^{(p)}}\sum_{g'=1}^{G} \mathbf{F}_{gg'}\phi_{g'}^{(p)} + \sum_{g'=1}^{g-1} \Sigma_{gg'}\phi_{g'}^{(p,q+1)} + \sum_{g'=g+1}^{G} \Sigma_{gg'}\phi_{g'}^{(p,q)} \tag{3-11b}$$

$$\mathbf{u} = \phi_g^{(p,q+1)} \tag{3-11c}$$

and p and q are the outer and inner iteration indices respectively. In the CCSI method we impose a red/black (checkerboard) partition on the problem, then matrix $\mathbf{A}$ and vectors $\mathbf{u}$ and $\mathbf{b}$ become

$$\mathbf{A} = \begin{bmatrix} \mathbf{D}_R & \mathbf{H} \\ \mathbf{H}^T & \mathbf{D}_B \end{bmatrix},$$

$$\mathbf{u} = \begin{bmatrix} \mathbf{u}_R \\ \mathbf{u}_B \end{bmatrix},$$

$$\mathbf{b} = \begin{bmatrix} \mathbf{b}_R \\ \mathbf{b}_B \end{bmatrix}.$$

Then the partitioned matrix equation which we are solving is

$$\begin{bmatrix} \mathbf{D}_R & \mathbf{H} \\ \mathbf{H}^T & \mathbf{D}_B \end{bmatrix}\begin{bmatrix} \mathbf{u}_R \\ \mathbf{u}_B \end{bmatrix} = \begin{bmatrix} \mathbf{b}_R \\ \mathbf{b}_B \end{bmatrix}.$$

If we define the following submatrices

$$\begin{aligned} \mathbf{F}_R &\equiv -\mathbf{D}_R^{-1}\mathbf{H} \\ \mathbf{F}_B &\equiv -\mathbf{D}_B^{-1}\mathbf{H}^T \\ \mathbf{c}_R &\equiv \mathbf{D}_R^{-1}\mathbf{b}_R \\ \mathbf{c}_B &\equiv \mathbf{D}_B^{-1}\mathbf{b}_B \end{aligned}$$

the matrix equation becomes

$$\begin{bmatrix} \mathbf{I} & -\mathbf{F}_R \\ -\mathbf{F}_B & \mathbf{I} \end{bmatrix} \begin{bmatrix} \mathbf{u}_R \\ \mathbf{u}_B \end{bmatrix} = \begin{bmatrix} \mathbf{c}_R \\ \mathbf{c}_B \end{bmatrix}. \tag{3-12}$$

Rearranging Equation (3-12) results in the Jacobi method

$$\mathbf{u}^{(r+1)} = \mathbf{B}\mathbf{u}^{(r)} + \mathbf{c}, \tag{3-13}$$

where r is the flux iteration index and $\mathbf{B}$, the Jacobi iteration matrix, is defined by

$$\mathbf{B} \equiv \begin{bmatrix} 0 & \mathbf{F}_R \\ \mathbf{F}_B & 0 \end{bmatrix}.$$

Chebyshev acceleration may be applied to the basic Jacobi method, and if the problem has a red/black partition this results in the CCSI method

$$\mathbf{u}_R^{(r+1)} = \omega_R^{(r+1)}\left(\mathbf{F}_R\mathbf{u}_B^{(r)} + \mathbf{c}_R\right) + \left(1 - \omega_R^{(r+1)}\right)\mathbf{u}_R^{(r)}, \tag{3-14a}$$

$$\mathbf{u}_B^{(r+1)} = \omega_B^{(r+1)}\left(\mathbf{F}_B\mathbf{u}_R^{(r+1)} + \mathbf{c}_B\right) + \left(1 - \omega_B^{(r+1)}\right)\mathbf{u}_B^{(r)}. \tag{3-14b}$$

The initial relaxation parameters are given by

$$\begin{aligned} \omega_R^{(1)} &= 1 \\ \omega_B^{(1)} &= \frac{1}{1 - \frac{1}{2}\rho^2} \end{aligned}$$

and for subsequent iterations the relaxation parameters are given by

$$\begin{aligned} \omega_R^{(r+1)} &= \frac{1}{1 - \frac{1}{4}\rho^2\omega_B^{(r)}} \\ \omega_B^{(r+1)} &= \frac{1}{1 - \frac{1}{4}\rho^2\omega_R^{(r+1)}} \end{aligned}$$

where ρ is the spectral radius of the Jacobi iteration matrix **B**. The Gauss-Seidel method may be obtained from Equation (3-14) by requiring $\omega_R^{(r+1)} = \omega_B^{(r+1)} = 1$. Flux iterations are performed until the following convergence criterion on the group flux is satisfied

$$\frac{1}{1 - \rho_g^2} \frac{\left\| \phi_g^{(r+1)} - \phi_g^{(r)} \right\|_2}{\left\| \phi_g^{(r+1)} \right\|_2} \le \varepsilon_4 , \tag{3-15}$$

or until the flux iteration limit is reached.

The CCSI method requires a good estimate of the spectral radius of the Gauss-Seidel iteration matrix ρ^2. An estimate of ρ^2 may be obtained by performing a series of Gauss-Seidel iterations, where the estimate of the spectral radius for group g is obtained using

$$\rho_g^{2\,(r+1)} = \frac{\left\| \phi_g^{(r+1)} - \phi_g^{(r)} \right\|_1}{\left\| \phi_g^{(r)} - \phi_g^{(r-1)} \right\|_1} . \tag{3-16}$$

3.3.4 General Iteration Strategy

In practice, one does not know the eigenvalue of a problem in advance, and, consequently, it is impossible to choose the optimal value of λ' to be used throughout the calculation. However, the following four-step algorithm has been found to produce near optimal behavior for a wide variety of problems.

1. One or more finite-difference outer iterations are performed to obtain an initial nonflat flux distribution. The first outer iteration is unaccelerated. Subsequent outer iterations are accelerated using the Wielandt method with a constant eigenvalue shift. This constant eigenvalue shift should be significantly larger than converged eigenvalue, a value of 1.5 has been found to be effective. The Gauss-Seidel method is used for the flux iterations. These finite-difference iterations are performed until a coarse convergence criterion (10^{-2}) on the eigenvalue is satisfied,

$$\left|\lambda^{(p)} - \lambda^{(p-1)}\right| \leq \varepsilon_1 . \qquad (3\text{-}17)$$

2. After an initial nonflat flux distribution has been obtained, the polynomial nodal method is used to calculate CMFD discontinuity factor ratios. Outer iterations are accelerated using the constant eigenvalue shift from step one. Flux iterations are performed using the Gauss-Seidel method. Outer iterations are performed until a fine convergence criterion (10^{-3}) on the eigenvalue is satisfied,

$$\left|\lambda^{(p)} - \lambda^{(p-1)}\right| \leq \varepsilon_2 . \qquad (3\text{-}18)$$

3. After the fine eigenvalue convergence criterion has been satisfied the spectral radii of the Gauss-Seidel iteration matrices are estimated. The eigenvalue shift is calculated using the previous eigenvalue estimate plus a constant shift factor (typically 0.02–0.05 for LWRs)

$$\lambda' = \lambda^{(p)} + \delta\lambda . \qquad (3\text{-}19)$$

The spectral radius of the Gauss-Seidel iteration matrix for each energy group is calculated using

$$\rho_g^{2\,(r+1)} = \frac{\left\| \phi_g^{(r+1)} - \phi_g^{(r)} \right\|_1}{\left\| \phi_g^{(r)} - \phi_g^{(r-1)} \right\|_1} \qquad (3\text{-}20)$$

where r is the flux iteration index. A number of flux iterations are performed until the spectral radii convergence criterion is satisfied

$$\left| \rho_g^{2\,(r+1)} - \rho_g^{2\,(r)} \right| \leq \varepsilon_5 \qquad (3\text{-}21)$$

or until the flux iteration limit for the spectral radii calculation is reached. A spectral radii convergence criterion, ε_5, in the range of 10^{-2} to 10^{-3} should be used, and a limit of eight flux iterations should be sufficient.

4. Once a good estimate of the spectral radii has been obtained the CCSI method may be used for the flux iterations. As in step 3 the eigenvalue shift is calculated using the previous eigenvalue estimate and a constant shift factor

$$\lambda' = \lambda^{(p)} + \delta\lambda .$$

Outer iterations are performed until the following eigenvalue, flux, and reactor power convergence criteria have been satisfied:

$$\left|\lambda^{(p+1)} - \lambda^{(p)}\right| \leq \varepsilon_3 \tag{3-22a}$$

$$\frac{1}{1-\rho_g^2}\frac{\left\|\phi_g^{(r+1)} - \phi_g^{(r)}\right\|_2}{\left\|\phi_g^{(r+1)}\right\|_2} \leq \varepsilon_4 , \quad g=1,\ldots,G \tag{3-22b}$$

$$\left|\frac{Q^{(p+1)} - Q^{(p)}}{Q^{(p)}}\right| \leq \varepsilon_6 \tag{3-22c}$$

where Q is the total reactor thermal power. The flux and eigenvalue convergence criteria should be in the range of $10^{-5} - 10^{-6}$ and the power convergence criterion should be in the range of $10^{-3} - 10^{-4}$.

3.4 ITERATION STRATEGIES FOR SOURCE PROBLEMS

This section describes the modifications to the basic iteration strategy described in the previous section that are necessary to solve source problems. In general, only a few minor modifications are required for the basic iteration strategy to apply to both eigenvalue and source problems.

3.4.1 Outer Iterations

The groupwise version of Equation (3-1) is given by

$$\mathbf{N}_g(\boldsymbol{\phi},\lambda)\boldsymbol{\phi}_g = \frac{1}{\lambda}\sum_{g'=1}^{G} \mathbf{F}_{gg'}\boldsymbol{\phi}_{g'} + \sum_{g'\neq g} \boldsymbol{\Sigma}_{gg'}\boldsymbol{\phi}_{g'} + \mathbf{q}_g \tag{3-23}$$

where,

$\mathbf{N}_g(\boldsymbol{\phi},\lambda)$ = N×N matrix containing diffusion, total cross section, and g→g scattering cross section terms for group g

$\mathbf{F}_{gg'}$ = N×N diagonal matrix containing the fission source terms from group g' to group g

$\boldsymbol{\Sigma}_{gg'}$ = N×N diagonal matrix containing the scattering terms from group g' to group g

$\boldsymbol{\phi}_g$ = vector of length N containing the group g node-averaged fluxes

$\mathbf{q}_g$ = vector of length N containing the group g extraneous neutron source terms.

For source problems λ is no longer the eigenvalue of the problem. It is a normalization factor that may be applied to the fission source. For most problems $\lambda = 1$. If λ is not equal to unity, it has a value which forces the reactor to be subcritical.

Moving the fission source term to the LHS and introducing Sutton's $\mathbf{A}_{g'g}$ matrix [S8] yields

$$\left[\mathbf{N}_g(\boldsymbol{\phi},\lambda) - \frac{1}{\lambda}\sum_{g'=1}^{G} \mathbf{F}_{gg'}\mathbf{A}_{g'g}\right]\boldsymbol{\phi}_g = \sum_{g'\neq g} \boldsymbol{\Sigma}_{gg'}\boldsymbol{\phi}_{g'} + \mathbf{q}_g \ . \tag{3-24}$$

Equation (3-24) may also be obtained from (3-8) by adding the source term $\mathbf{q}_g$ to the RHS and setting $\lambda' = \lambda$.

For source problems the outer iterations consist of iterations on the total reactor thermal power Q. The behavior of this global variable will control the logic used in the inner and flux iterations. The total reactor thermal power is given by

$$Q = \mathbf{V}^T \sum_{g'=1}^{G} \frac{\kappa}{\lambda} \boldsymbol{\Sigma}_{fg'} \boldsymbol{\phi}_{g'} \tag{3-25}$$

where,

$\boldsymbol{\Sigma}_{fg}$ = N×N diagonal matrix containing the macroscopic fission cross sections for group g
$\boldsymbol{\phi}_g$ = vector of length N containing the group g node-averaged fluxes
$\mathbf{V}$ = vector of length N containing the node volumes
κ = average energy produced per fission.

For source problems the outer iterations are iterations on the total reactor thermal power. The group fluxes are obtained from a series of inner and outer iterations. The outer iterations may be expressed by

$$\boldsymbol{\phi}_g^{(p+1)} = \left[\mathbf{N}_g(\boldsymbol{\phi}^{(p)},\lambda) - \frac{1}{\lambda} \sum_{g'=1}^{G} \mathbf{F}_{gg'} \mathbf{A}_{g'g}^{(p)} \right]^{-1} \times \left\{ \sum_{g' \neq g} \boldsymbol{\Sigma}_{gg'} \boldsymbol{\phi}_{g'}^{(p)} + \mathbf{q}_g \right\} \tag{3-26a}$$

$$Q^{(p+1)} = \mathbf{V}^T \sum_{g'=1}^{G} \frac{\kappa}{\lambda} \boldsymbol{\Sigma}_{fg'} \boldsymbol{\phi}_{g'}^{(p+1)} \tag{3-26b}$$

where p is the outer iteration index.

3.4.2 Inner Iterations

Inner iterations are used to solve Equation (3-24). The $\mathbf{N}_g$ and $\mathbf{A}_{g'g}$ matrices are updated in order to account for nonlinearity. The detailed calculation procedure used for the inner iterations is as follows:

1. Face-averaged heterogeneous currents are updated using the CMFD coupling equation (2-20) and the flux from the previous iteration.

2. The higher-order expansion coefficients, a_{gu3} and a_{gu4}, are calculated using Equations (2-60) and the updated heterogeneous currents.
3. The heterogeneous currents are updated again this time using the nodal coupling equation (2-67).
4. The CMFD discontinuity factor ratios are updated using Equation (2-29).
5. The matrix $\mathbf{N}_g(\boldsymbol{\phi}^{(p,q)}, \lambda^{(p)})$ is calculated using the recently updated CMFD discontinuity factor ratios. The $\mathbf{A}_{g'g}^{(p,q)}$ matrices are calculated using the group fluxes from the previous iteration.
6. The node-averaged group flux vectors are updated using a series of flux iterations. The following matrix problems are solved iteratively,

$$\left[\mathbf{N}_g(\boldsymbol{\phi}^{(p,q)}, \lambda^{(p)}) - \frac{1}{\lambda}\sum_{g'=1}^{G} \mathbf{F}_{gg'}\mathbf{A}_{g'g}^{(p,q)}\right]\boldsymbol{\phi}_g^{(p,q+1)} = \left\{\sum_{g'=1}^{g-1} \Sigma_{gg'}\boldsymbol{\phi}_{g'}^{(p,q+1)} + \sum_{g'=g+1}^{G} \Sigma_{gg'}\boldsymbol{\phi}_{g'}^{(p,q)} + \mathbf{q}_g\right\}, \quad g=1,\ldots G \tag{3-27}$$

where p and q are the outer and inner iteration indices respectively. Note that upscattering is not explicitly treated during the flux iterations. However, by performing a series of inner or outer iterations upscattering may be adequately modelled.

3.4.3 Flux Iterations

Equation (3-27) will be solved using the CCSI method. The same procedure as described in section 3.3.3 will be used with the following exceptions:

$$\mathbf{A} = \mathbf{N}_g(\boldsymbol{\phi}^{(p,q)}, \lambda^{(p)}) - \frac{1}{\lambda}\sum_{g'=1}^{G} \mathbf{F}_{gg'}\mathbf{A}_{g'g}^{(p,q)} \tag{3-28a}$$

$$\mathbf{b} = \sum_{g'=1}^{g-1} \Sigma_{gg'}\boldsymbol{\phi}_{g'}^{(p,q+1)} + \sum_{g'=g+1}^{G} \Sigma_{gg'}\boldsymbol{\phi}_{g'}^{(p,q)} + \mathbf{q}_g \tag{3-28b}$$

where p and q are the outer and inner iteration indices respectively.

3.4.4 General Iteration Strategies

With a few simple modifications the four-step algorithm used to solve eigenvalue problems may also be used to solve source problems. The following procedure should be used to solve source problems.

1. One or more finite-difference outer iterations are performed to obtain an initial nonflat flux distribution. The eigenvalue shift must be set equal to the reactor eigenvalue, $\lambda' = \lambda = 1$. The Gauss-Seidel method is used for the flux iterations. These finite-difference iterations are performed until a coarse convergence criterion (10^{-2}) on the total reactor thermal power is satisfied,

$$\left| \frac{Q^{(p)} - Q^{(p-1)}}{Q^{(p-1)}} \right| \le \varepsilon_1 \,. \qquad (3\text{-}29)$$

2. After an initial nonflat flux distribution has been obtained, the polynomial nodal method is used to calculate CMFD discontinuity factor ratios. Again the eigenvalue shift must be set equal to the reactor eigenvalue, $\lambda' = \lambda = 1$. Flux iterations are performed using the Gauss-Seidel method. Outer iterations are performed until a fine convergence criterion (10^{-3}) on the total reactor thermal power is satisfied,

$$\left| \frac{Q^{(p)} - Q^{(p-1)}}{Q^{(p-1)}} \right| \le \varepsilon_2 \,. \qquad (3\text{-}30)$$

3. After the fine eigenvalue convergence criterion has been satisfied, the spectral radii of the Gauss-Seidel iteration matrices are estimated. The eigenvalue shift must be set equal to the reactor eigenvalue, $\lambda' = \lambda = 1$. The spectral radius of the Gauss-Seidel iteration matrix for each energy group is calculated using

$$\rho_g^{2\,(r+1)} = \frac{\left\| \phi_g^{(r+1)} - \phi_g^{(r)} \right\|_1}{\left\| \phi_g^{(r)} - \phi_g^{(r-1)} \right\|_1} \qquad (3\text{-}20)$$

where r is the flux iteration index. A number of flux iterations are performed until the spectral radii convergence criterion is satisfied

$$\left| \rho_g^{2\,(r+1)} - \rho_g^{2\,(r)} \right| \leq \varepsilon_5 \tag{3-21}$$

or until the flux iteration limit for the spectral radii calculation is reached. A spectral radii convergence criterion, ε_5, in the range of 10^{-2} to 10^{-3} should be used, and a limit of eight flux iterations should be sufficient.

4. Once a good estimate of the spectral radii has been obtained the CCSI method may be used for the flux iterations. As in steps 1–3 the eigenvalue shift must be set equal to the reactor eigenvalue, $\lambda' = \lambda - 1$. Outer iterations are performed until the following convergence criteria on the flux and total reactor thermal power have been satisfied:

$$\frac{1}{1-\rho_g^2} \frac{\left\| \phi_g^{(r+1)} - \phi_g^{(r)} \right\|_2}{\left\| \phi_g^{(r+1)} \right\|_2} \leq \varepsilon_4\,, \quad g=1,\ldots,G \tag{3-31a}$$

$$\left| \frac{Q^{(p+1)} - Q^{(p)}}{Q^{(p)}} \right| \leq \varepsilon_6 \tag{3-31b}$$

The flux and eigenvalue convergence criteria should be in the range of 10^{-5} – 10^{-6} and the power convergence criterion should be in the range of 10^{-5} – 10^{-6}.

3.5 ITERATION OPTIMIZATION

The description of the iterative method for solving the static nodal diffusion equation, as detailed in Sections 3.3 and 3.4 for eigenvalue and source problems, has largely been completed. There remain three issues which much be addressed before the iterative method is completely specified. These issues are the selection of the number of inner iterations per outer iteration, the selection of the maximum number of flux iterations per inner iteration, and the selection of the eigenvalue shift to be used to accelerate the convergence of the outer iterations in eigenvalue problems.

3.5.1 Inner Iterations

In order to determine the optimum number of inner iterations per outer iteration the 2D IAEA PWR problem [A3] was solved using several inner per outer iteration ratios. Table 3-1 illustrates the effect of the various inner per outer iteration ratios on the iterative solution. Although the use of an inner per outer iteration ratio greater than unity results in a reduction in the total number of outer iterations, it does not result in a corresponding reduction in the total execution time. Consequently, the use of an inner per outer iteration ratio greater than unity is not justified.

The increase in execution time for the solutions with a inner per outer iteration ratio greater than unity may be attributed to the relatively time consuming procedure for updating the nodal currents, which is require for every inner iteration. This procedure consists of the computation of the higher-order expansion coefficients, Equation (2-60), and the currents using the nodal coupling equation, Equation (2-67). These two calculations, which are required in order to update the CMFD discontinuity factor ratios, are the principal time-sinks in the inner iteration. Therefore, in order to minimize the total execution time one should minimize the number of inner iterations.

Table 3-1

Inner Iteration Optimization

2D IAEA PWR Problem
Coarse mesh, 20x20 cm
Number of flux iterations = 16
Flux convergence criteria = 10^{-6}
Eigenvalue convergence criteria = 10^{-6}
Eigenvalue shift = $\lambda + 0.05$

Inner Iterations per Outer	Number of Outer Iterations	Total Execution Time (sec)†	Eigenvalue λ
1	21	26.72	1.029528
2	17	39.05	1.029528
3	18	60.93	1.029528
4	17	75.40	1.029527

†Macintosh SE/30.

Thus, in general, the optimization of the iteration strategy, with one inner iteration per outer iteration, requires the minimization of the number of outer iterations. This may be accomplished in two way: by converging the flux iteration relatively tightly and by accelerating the outer iterations.

3.5.2 Flux Iterations

Flux iterations are used to solve matrix problems of the form $\mathbf{Au} = \mathbf{b}$, for each energy group, during each inner iteration. In general, the degree to which these matrix problems are converged is governed by the maximum number of flux iterations which are permitted during each inner iteration. In order to determine a reasonable limit on the maximum number of flux iterations per inner iteration the 2D IAEA PWR problem [A3] was solved with several flux iteration limits. Table 3-2 shows the effect of the flux iteration limit on the iterative solution. As the flux iteration limit is increased the number of outer iteration required to converge the problem and the total execution time are decreased until a critical number is reached. For this problem it is 14 flux iterations per inner iteration. Above this value no additional outer iterations are required and only a marginal increase in the total execution time is experienced.

These results indicate that, in general, the flux iteration limit should be large enough to completely converge the matrix problems at each inner iteration. Since a convergence criterion on the group flux is used during the flux iterations, the use of a flux iteration limit larger than necessary will not result in an excessive number of flux iterations. Thus, a large flux iteration limit may be used without significantly increasing the execution time. In practice a flux iteration limit of approximately 16–32 iterations has been found to be sufficient for most problems.

Table 3-2

Flux Iteration Optimization

2D IAEA PWR Problem
Coarse mesh, 20x20 cm
Number of inner iterations per outer = 1
Flux convergence criteria = 10^{-6}
Eigenvalue convergence criteria = 10^{-6}
Eigenvalue Shift = $\lambda + 0.05$

Maximum Number of Flux Iterations	Number of Outer Iterations	Total Execution Time (sec)†	Eigenvalue λ
4	37	43.33	1.029529
6	31	36.32	1.029529
8	29	34.48	1.029529
10	26	31.25	1.029529
12	24	29.25	1.029529
14	21	25.78	1.029528
16	21	25.97	1.029528
24	21	26.28	1.029528
32	21	26.32	1.029528

†Macintosh SE/30.

3.5.3 Eigenvalue Shift Optimization

The last remaining issue to be addressed is the selection of the optimum eigenvalue shift, λ', for use in eigenvalue problems. As was shown in Section 3.3.1 the use of Wielandt's method of fractional iteration is an effective method for accelerating the outer iterations. The optimum eigenvalue shift is determined by two competing phenomena. First, the outer iteration convergence rate is maximized when the eigenvalue shift is equal to the true eigenvalue (the dominance ratio is zero) and minimized when the eigenvalue shift is equal to infinity (the power method). Second, the flux iteration convergence rate is minimized when the eigenvalue shift is equal to the true eigenvalue and maximized when the eigenvalue shift is equal to infinity. Therefore, the overall convergence rate is maximized by an eigenvalue shift that balances the outer iteration convergence behavior and flux iteration convergence behavior.

Several numerical experiments were performed in order to gain insight into the phenomena controlling the optimization of the eigenvalue shift. Two different reactor configurations were analyzed using several spatial mesh sizes. The effects of the eigenvalue shift on the iteration process are summarized in Tables 3-3 thru 3-5 for the 2D IAEA PWR problem [A3] with coarse mesh (20x20 cm), fine mesh (10x10 cm), and very-fine mesh (5x5 cm) spacings respectively. The effects on the 2D LRA BWR problem [A3] with coarse mesh (15x15 cm) and fine mesh (7.5x7.5 cm) spacings are summarized in Tables 3-6 and 3-7 respectively. Using the results from these two different reactor configurations we may draw the following general observations regarding the convergence behavior of Wielandt's method in the Hybrid Nodal Method:

1. The spectral radii of the Gauss-Seidel flux iteration matrices increase as the eigenvalue shift is decreased.
2. The spectral radii of the Gauss-Seidel flux iteration matrices increase as the spatial mesh size is decreased.

3. The spectral radii of the unaccelerated Gauss-Seidel flux iteration matrices are very small for problems with assembly sized nodes.
4. The outer iteration convergence rate increases as the eigenvalue shift approaches the optimum eigenvalue shift.
5. The flux iteration convergence rate decreases as the eigenvalue shift decreases.
6. For eigenvalue shifts less than the optimum eigenvalue shift the effect of the decrease in the flux iteration convergence rate exceeds the effect of the increase in the outer iteration convergence rate, resulting in a decrease in the overall convergence rate.
7. The overall iteration is optimized, with respect to total execution time, when the eigenvalue shift exceeds the true eigenvalue by a few percent (typically 0.02–0.05 for LWRs).
8. The optimum eigenvalue shift is not significantly dependent upon the spatial mesh size, despite the fact that the spectral radii of the flux iteration matrices change significantly.

Wielandt's method is effective in accelerating the overall convergence for the following reasons. The current calculation which occurs at each inner iteration is so computationally intensive that we would like to minimize the number of inner iterations that must be performed. By reducing the dominance ratio, eigenvalue shifting increases the convergence rate of the outer iterations reducing the number of outer iterations, and therefore inner iterations, required for convergence. Eigenvalue shifting, by increasing the spectral radii of the flux iteration matrices, results in a reduction in the flux iteration convergence rate, effectively shifting more of the computational burden upon the flux iterations. Eventually, as the eigenvalue shift approaches the true eigenvalue, a point is reached where the computational burden can not be shifted on to the flux iterations without reducing the overall convergence rate. At this point the spectral radii of the flux iteration matrices are so large that the flux iterations are not fully converged which results in a reduction in the outer iteration convergence rate. As the eigenvalue shift is decreased further the incomplete convergence of the flux iterations results in additional outer iterations and an increase in the total execution time.

The application of Wielandt's method to a wide variety of problems in several nodal codes [S2,S5] has led to the following general procedure for implementing eigenvalue shifting. At the start of the problem, since the true eigenvalue is generally unknown, an initial constant value of 1.5 is used for the eigenvalue shift. With this initial eigenvalue shift there is no possibility of converging to the wrong eigenvector as long as the true eigenvalue is less than 1.5. After the eigenvalue has converged to about 10^{-3} (generally only 5–10 outer iterations), the eigenvalue shift λ' is set equal to the estimated eigenvalue λ plus an arbitrary constant $\delta\lambda$ (generally 0.02–0.05 for LWRs),

$$\lambda' = \lambda + \delta\lambda .$$

Thus, the eigenvalue shift follows the eigenvalue estimate and is ultimately near the anticipated optimum eigenvalue shift when the true eigenvalue is determined. This general procedure has been used on a variety of problems without difficulty.

Table 3-3

Eigenvalue Shift Optimization

(Coarse Mesh IAEA PWR)

2D IAEA PWR Problem
Coarse mesh, 20x20 cm
Number of flux iterations = 16
Number of inner iterations per outer = 1
Flux convergence criterion = 10^{-6}
Eigenvalue convergence criterion = 10^{-6}

Eigenvalue Shift λ'	Number of Outer Iterations	Total Execution Time (sec)[†]	Eigenvalue λ	Gauss-Seidel Spectral Radius	
				Group 1	Group 2
∞	118	140.37	1.029501	0.0997	0.0040
$\lambda + 1.0$	57	67.98	1.029515	0.2374	0.0031
$\lambda + 0.5$	43	51.38	1.029520	0.3342	0.0028
$\lambda + 0.2$	24	28.55	1.029529	0.4997	0.0033
$\lambda + 0.1$	21	25.48	1.029535	0.6278	0.0032
$\lambda + 0.05$	21	26.08	1.029528	0.7257	0.0032
$\lambda + 0.02$	24	29.80	1.029528	0.8028	0.0032
$\lambda + 0.01$	28	35.37	1.029528	0.8325	0.0032
$\lambda + 0.005$	32	40.78	1.029528	0.8483	0.0032
$\lambda + 0.002$	50	64.85	1.029528	0.8581	0.0032
$\lambda + 0.001$	80	106.97	1.029528	0.8614	0.0032

[†] Macintosh SE/30.

Table 3-4

Eigenvalue Shift Optimization

(Fine Mesh IAEA PWR)

2D IAEA PWR Problem
Fine mesh, 10x10 cm
Number of flux iterations = 16
Number of inner iterations per outer = 1
Flux convergence criterion = 10^{-6}
Eigenvalue convergence criterion = 10^{-6}

Eigenvalue Shift λ'	Number of Outer Iterations	Total Execution Time (sec)†	Eigenvalue λ	Gauss-Seidel Spectral Radius	
				Group 1	Group 2
∞	118	483.23	1.029547	0.4042	0.1444
$\lambda + 1.0$	63	265.83	1.029560	0.5922	0.1382
$\lambda + 0.5$	48	204.50	1.029565	0.6808	0.1484
$\lambda + 0.2$	30	130.40	1.029568	0.7970	0.1496
$\lambda + 0.1$	21	91.13	1.029570	0.8600	0.1499
$\lambda + 0.05$	17	72.67	1.029574	0.8993	0.1501
$\lambda + 0.02$	23	99.67	1.029573	0.9263	0.1502
$\lambda + 0.01$	24	104.48	1.029573	0.9359	0.1502
$\lambda + 0.005$	31	137.02	1.029573	0.9408	0.1502
$\lambda + 0.002$	84	383.53	1.029572	0.9439	0.1502
$\lambda + 0.001$	160+	737.30	1.029572	0.9449	0.1502

†Macintosh SE/30.

Table 3-5

Eigenvalue Shift Optimization

(Very Fine Mesh IAEA PWR)

2D IAEA PWR Problem
Very fine mesh, 5x5 cm
Number of flux iterations = 16
Number of inner iterations per outer = 1
Flux convergence criterion = 10^{-6}
Eigenvalue convergence criterion = 10^{-6}

Eigenvalue Shift λ'	Number of Outer Iterations	Total Execution Time (sec)†	Eigenvalue λ	Gauss-Seidel Spectral Radius	
				Group 1	Group 2
∞	117	2085.65	1.029543	0.7464	0.5536
$\lambda + 1.0$	67	1217.75	1.029555	0.8732	0.5573
$\lambda + 0.5$	52	959.98	1.029561	0.9101	0.5571
$\lambda + 0.2$	34	634.47	1.029565	0.9492	0.5570
$\lambda + 0.1$	26	484.33	1.029568	0.9678	0.5570
$\lambda + 0.05$	22	407.45	1.029569	0.9786	0.5569
$\lambda + 0.02$	20	393.78	1.029568	0.9858	0.5569
$\lambda + 0.01$	27	509.43	1.029568	0.9882	0.5569
$\lambda + 0.005$	44	831.80	1.029567	0.9895	0.5569
$\lambda + 0.002$	97	1831.93	1.029568	0.9903	0.5569
$\lambda + 0.001$	160+	3023.37	1.029566	0.9905	0.5569

†Macintosh SE/30.

Table 3-6

Eigenvalue Shift Optimization

(Coarse Mesh LRA BWR)

2D LRA BWR Static Problem
Coarse mesh, 15x15 cm
Number of flux iterations = 32
Number of inner iterations per outer = 1
Flux convergence criterion = 10^{-6}
Eigenvalue convergence criterion = 10^{-6}

Eigenvalue Shift λ'	Number of Outer Iterations	Total Execution Time (sec)†	Eigenvalue λ	Gauss-Seidel Spectral Radius	
				Group 1	Group 2
∞	152	308.90	0.996288	0.1258	0.0035
$\lambda + 0.1$	32	68.00	0.996326	0.6731	0.0061
$\lambda + 0.05$	26	56.65	0.996328	0.7772	0.0060
$\lambda + 0.02$	24	55.08	0.996328	0.8606	0.0059
$\lambda + 0.01$	26	61.47	0.996329	0.8843	0.0060
$\lambda + 0.005$	30	71.45	0.996329	0.9011	0.0059
$\lambda + 0.002$	32	76.27	0.996329	0.9115	0.0059
$\lambda + 0.001$	38	92.88	0.996329	0.9150	0.0059

†Macintosh SE/30.

Table 3-7

Eigenvalue Shift Optimization

(Fine Mesh LRA BWR)

2D LRA BWR Static Problem
Fine mesh, 7.5x7.5 cm
Number of flux iterations = 32
Number of inner iterations per outer = 1
Flux convergence criterion = 10^{-6}
Eigenvalue convergence criterion = 10^{-6}

Eigenvalue Shift λ'	Number of Outer Iterations	Total Execution Time (sec)†	Eigenvalue λ	Gauss-Seidel Spectral Radius	
				Group 1	Group 2
∞	149	1264.65	0.996336	0.4727	0.1086
$\lambda + 0.1$	31	291.87	0.996372	0.8944	0.1109
$\lambda + 0.05$	22	207.50	0.996374	0.9278	0.1109
$\lambda + 0.02$	19	181.40	0.996376	0.9500	0.1109
$\lambda + 0.01$	19	175.68	0.996376	0.9580	0.1109
$\lambda + 0.005$	22	206.25	0.996376	0.9621	0.1109
$\lambda + 0.002$	25	237.45	0.996375	0.9646	0.1109
$\lambda + 0.001$	82	833.17	0.996375	0.9655	0.1109

†Macintosh SE/30.

3.6 SUMMARY

In this chapter, the numerical properties of the nodal diffusion equations were examined and the hybrid nodal method was shown to reduce to the mesh-centered finite difference equation in the limit of infinitely fine mesh spacing. As a consequence, it was shown that the hybrid nodal method converges to the exact solution of the neutron diffusion equation in the limit of infinitely fine mesh spacing. For larger mesh spacings the Aragonés and Ahnert stability condition was shown to guarantee the stability of the iterative solution.

The numerical methods used to solve the nodal diffusion equations were also detailed in this chapter. The iterative strategies used to solve both eigenvalue problems and source problems were described. Finally, techniques for optimizing the iterative solution of the nodal diffusion equations were described.

CHAPTER 4

RESULTS

4.1 INTRODUCTION

In Chapter 2 a polynomial nodal method which permits discontinuities in the face-averaged fluxes and currents was derived. This nodal method was based on the assumptions that the transverse-integrated flux may be accurately approximated by a low-order polynomial and that the transverse leakage may be approximated by a quadratic polynomial. In Chapter 3 a multi-level iterative scheme for solving the nodal diffusion equations was described.

In this chapter, the results from the application of this nodal method to several two- and three-dimensional, few-group, static reactor benchmark problems are presented. The spatial convergence rate of the nodal method is also examined. Throughout the chapter the accuracy and computational efficiency of the nodal method are compared to that of conventional finite difference methods and to other nodal methods.

4.2 QUAGMIRE CODE

The methods developed in Chapter 2 and the numerical techniques described in Chapter 3 are incorporated into the QUAGMIRE code. This computer code solves the one-, two- and three-dimensional, few-group, static neutron diffusion problem in Cartesian geometry. QUAGMIRE solves both eigenvalue and source problems.

QUAGMIRE is designed for workstation class computers running the BSD 4.2 or SYS 5.3 "flavors" of the UNIX operating system. QUAGMIRE is written in standard FORTRAN-77, except for several calls to standard UNIX system routines which perform dynamic memory management and return the command line, system time, system date, and execution time. All references to system dependent routines are isolated in a few routines in order to permit easy porting of the code to other computer systems and operating systems. A version of QUAGMIRE also exists for the Macintosh SE/30 and Macintosh II series of personal computers running System 6.0 or higher. All computations are performed in double precision in order to minimize truncation and roundoff errors.

Neutron diffusion problems may be solved using either a polynomial nodal method or a conventional mesh-centered finite difference method. With the polynomial nodal method option, problems may be solved using either a quadratic (second-order), cubic (third-order), or quartic (fourth-order) flux expansion. QUAGMIRE has no limit on the number of energy groups that may be used in problems or the structure of the energy groups. Upscattering is permitted. It uses a more generalized set of homogenization parameters (cross sections) which may include both flux and current discontinuity factors. QUAGMIRE is capable of modelling nonuniform mesh spacings and irregular geometries (jagged boundaries). It also has a control mechanism option which is capable of modelling control mechanisms which enter from the top of the reactor (PWR-type control rods), control mechanisms which enter from the bottom of the reactor (BWR-type control blades), and control drums.

4.2.1 Transverse-Leakage Approximation at the Reactor Boundary

One detail regarding the determination of the cubic and quartic flux expansion coefficients remains to be specified, the shape of the transverse-leakage at external reactor boundaries. In the interior the transverse-leakage is typically expanded as a quadratic polynomial which preserves the node-averaged transverse-leakages in the three adjacent nodes, Finnemann's [B2] quadratic transverse-leakage approximation. This approximation requires the node-averaged transverse-leakages in three adjacent nodes in order to determine the quadratic expansion for the node in the center. This does not present a problem in the interior of the reactor and at internal (zero net-current) reactor boundaries, where we may take advantage of symmetry. However, along the external reactor boundary there is no longer a node adjacent to each side of the boundary node. QUAGMIRE contains options for four different ways in which the shape of the transverse-leakage may be approximated. They are, in order of increasing sophistication:

1. Flat transverse-leakage approximation throughout the reactor.
2. Quadratic transverse-leakage approximation in the fuel-bearing region of the reactor (the reactor core) and a flat transverse-leakage approximation in the reflector and in nodes adjacent to the external boundary.
3. Quadratic transverse-leakage approximation throughout the reactor except for nodes adjacent to the external boundary where a flat transverse-leakage approximation is used.
4. Quadratic transverse-leakage approximation throughout the reactor. For nodes adjacent to the external boundary a lopsided quadratic expansion, which preserves the node-averaged transverse-leakages in the three adjacent nodes, is used.

The first option, a flat transverse-leakage approximation throughout the reactor, tends to result in unacceptably large errors. Its use is not recommended.

Experience has shown that the second boundary node option, a quadratic transverse-leakage approximation in the core and a flat transverse-leakage approximation in the reflector, works best for a large variety of problems. In particular it works best for problems which have a relatively deep reflector, such as the LRA BWR problem (Section C.4). This is because deep within the reflector the flux tends to be relatively small and, therefore, an accurate estimate of the shape of the transverse-leakage in these nodes is not critical. In fact, in the case of the 3D LRA BWR problem, the use of other boundary node treatments produced, during the iterative process, negative node-averaged flux estimates for nodes near the external boundary, and resulted in stability problems. No stability problems have been experienced if the flat transverse-leakage approximation is used in the reflector.

For problems with relatively thin reflectors, such as the IAEA PWR problem (Section C.3), the third boundary node option, the use of the quadratic transverse-leakage approximation for nodes in the interior of the reactor and a flat transverse-leakage approximation for nodes on the external boundary, has also been found to yield accurate results. In particular for the 2D IAEA PWR problems with multiple nodes per assembly this approximation has been found to yield significantly more accurate results. This is because the flux for nodes on the external boundary tends to be relatively small and insensitive to the shape of the transverse-leakage. However, for nodes along the core/reflector interface the flux tends to be relatively large and, as a result, sensitive to the shape of the transverse-leakage, therefore a more accurate approximation of the transverse-leakage shape is desirable.

For problems with fuel-bearing material along the external boundary the fourth boundary node option, the use of the quadratic transverse-leakage approximation throughout the reactor with a lopsided quadratic expansion for nodes along the external boundary, produces the best results. In fact for bare core problems this option is required for accurate results. This is because, for bare core problems, the flux and current along the external boundary tends to be relatively high, necessitating an accurate estimate of the shape of the transverse-leakage in these nodes.

For problems with a deep blanket, such as the LMFBR benchmark problem (Section C.5), either the third or fourth boundary node option may be used. However, the use of a lopsided quadratic expansion for the transverse-leakage in nodes along the external boundary tends to produce slightly more accurate results.

4.2.2 Measurements of Error

The solutions to problems presented in this chapter are compared to reference solutions which are spatially converged. The quantity of principal interest is the nodal power density. The reference nodal power densities and the error in the QUAGMIRE solutions are presented in Appendix D. However for purposes of summarizing these results, tables containing the maximum error, average error, maximum relative error, and average relative error in the normalized nodal power densities are presented in this chapter. With the power density in the ith node represented as P^i, the reference power density represented as P^i_{ref}, and the reference core-averaged power density represented as $\overline{P}_{ref}$, the maximum error in the nodal power density is defined to be

$$\varepsilon_{max} \equiv \underset{\text{over all } i}{\text{maximum}} \left\{ \frac{|P^i - P^i_{ref}|}{\overline{P}_{ref}} \right\} .$$

The average error in the nodal power density is defined to be

$$\overline{\varepsilon} \equiv \frac{1}{V_{core}} \sum_i \left(\frac{|P^i - P^i_{ref}|}{\overline{P}_{ref}} \right) V^i ,$$

where V^i is the volume of node i and V_{core} is the volume of the core. The maximum relative error in the nodal power density is defined to be

$$\varepsilon_{rel} \equiv \underset{\text{over all } i}{\text{maximum}} \left\{ \frac{|P^i - P^i_{ref}|}{P^i_{ref}} \right\} .$$

The average relative error in the nodal power density is defined to be

$$\overline{\varepsilon}_{rel} \equiv \frac{1}{V_{core}} \sum_i \left(\frac{|P^i - P^i_{ref}|}{P^i_{ref}} \right) V^i .$$

And finally, the error in the eigenvalue is defined to be

$$\varepsilon_{\lambda} = \lambda - \lambda_{ref} ,$$

where λ is the reactor eigenvalue and λ_{ref} is the reference eigenvalue. Note that these error measurements apply even when reference core-averaged power densities other than unity are used.

4.2.3 Number of Unknowns

The number of unknowns is dependent upon the dimensions of the problem and the solution method. The QUAGMIRE code has options to use the CMFD method and quadratic, cubic and quartic polynomial nodal methods. The number of unknowns required by these methods are summarized in Table 4-1. For the nodal methods the node-averaged flux, face-averaged currents, and the CMFD discontinuity factor ratios are considered to be unknowns. The CMFD discontinuity factor ratio vectors are equal in length to the current vectors. The higher order flux expansion coefficients are stored in temporary working vectors and therefore are not considered unknowns. The number of unknowns required for the flux and current components, respectively, are

$$\begin{aligned} N_{flux} &= G \times (IJK) \\ N_{cur} &= G \times [(I+1)JK + (J+1)IK + (K+1)IJ] \end{aligned}$$

where I is defined as the number of nodes in the x directions; J is defined as the number of nodes in the y direction; K is defined as the number of nodes in the z direction, and G is defined as the number of energy groups. Thus, the number of unknowns does not increases with the order of the flux expansion.

Table 4-1

Number of Unknowns Required by Nodal Methods

Method	Number of Unknowns
CMFD Method	N_{flux}
Quadratic Nodal Method	$N_{flux} + 2N_{cur}$
Cubic Nodal Method	$N_{flux} + 2N_{cur}$
Quartic Nodal Method	$N_{flux} + 2N_{cur}$

4.2.4 Execution Times

The execution times of computer codes are commonly used to compare their relative performance. Direct comparison of the execution times from different computer codes is often difficult unless they are run on the same computer system, using the same compiler, and under the same conditions because the performance of computer systems tends to vary widely. QUAGMIRE's increased generality, the introduction of flux and current discontinuity factor and the ability to model problems with more than two energy groups, tends to increase its execution time. In addition, QUAGMIRE's use of double precision tends to increase its execution time relative to other codes which use only single precision.

The LINPACK [D1] benchmark has been found to be useful in providing a rough estimate of the floating-point performance of different computer systems. It measures single precision (32-bit) and double precision (64-bit) floating-point performance, in terms of millions of floating-point operations per second (MFLOPS), by solving a linear system of order 100 using the LINPACK LU decomposition routines (SGEFA and SGEFL for single precision and DGEFA and DGEFL for double precision). The LINPACK benchmark simulates the typical computational mix found in many engineering calculations. The single and double precision LINPACK benchmark software may be obtained from `netlib@ornl.gov`[1]. Dongarra [D2] has summarized the full precision (64-bit) LINPACK MFLOPS ratings for a large number of computer systems. A recently updated copy of Dongarra's report summarizing the benchmark

---

[1] The FORTRAN code for the single precision LINPACK benchmark may be obtained by sending the following electronic mail message to `netlib@ornl.gov`:

```
send linpacks from benchmark.
```

The double precision code for the LINPACK benchmark may be obtained by sending:

```
send linpackd from benchmark.
```

results may also be obtained from `netlib@ornl.gov`[2]. Table 4-2 compares the LINPACK MFLOPS ratings for a variety computer systems. The ratio of the MFLOPS ratings may be used to provide a rough comparison of the relative execution times of codes on different computer systems.

---

[2] A Postscript copy of the most recent version of Dongarra's report [D2] summarizing the LINPACK benchmark results for a variety of computer systems may be obtained by sending the following electronic mail message to `netlib@ornl.gov`:

```
send performance from benchmark.
```

Table 4-2

LINPACK MFLOPS Ratings for Several Computer Systems

Computer System	Full Precision	Single MFLOPS	Double MFLOPS
Mainframes			
CDC CYBER 176 [D2]	S	4.6	
CDC 7600 [D2]	S	3.3	
IBM 370/195 [D1]	D	2.4	2.3
CDC CYBER 175 [D2]	S	2.1	
IBM 370/168 [D1]	D	1.2	1.2
CDC 6600 [D2]	S	.48	
Workstations			
IBM RS/6000-550 (41 MHz) [D2]	D		27
HP 9000/730 (66 MHz) [D2]	D		24
SGI 4D/310 (1 proc) 33 MHz [D2]	D		5.0
SUN SPARCstation 2 [D2]	D		4.0
SGI 4D/210 (1 proc) 25 MHz	D	4.8	2.8
SUN SPARCstation 1 [D2]	D		1.4
DEC VS3100	D	0.78	0.49
MicroVAX II	D	0.61	0.39
Apollo DN3500	D	0.23	0.19
Personal Computers			
Apple Macintosh IIfx [D2]	D		0.41
20 MHz 386 w/3167	D	0.49	0.29
25 MHz 386 w/80387	D	0.30	0.27
Apple Macintosh SE/30	D	0.14	0.12

4.3 2D STATIC RESULTS

In this section, the results from several 2D benchmark problems are presented. Most of the benchmark problems use large homogenized regions in which coarse spatial meshes may be used. The geometry and cross sections for these problems are completely specified so that no modelling ambiguities exist. The descriptions of these benchmark problems are presented in Appendix C. Unless otherwise specified all of the results were obtained from QUAGMIRE polynomial nodal method using its quartic flux expansion option. In addition, unless otherwise specified, an eigenvalue and a pointwise flux convergence criteria of 10^{-6} has been used. These are relatively tight eigenvalue and pointwise flux convergence criteria and their use is possible because all computations are performed in double precision.

4.3.1 Two-Group Homogeneous Bare Core Benchmark Problem

This benchmark problem is designed to study the dependence of spatial discritization error on mesh size for the quadratic, cubic, and quartic flux expansion options of the QUAGMIRE nodal code. The benchmark, which is based on one of Myung Kim's [K1] benchmark problems, consists of a small, two-dimensional, two-group, homogeneous bare core with zero flux boundary conditions and zero transverse buckling. The core is 60.0 cm in length in both the x and y dimensions. The benchmark may easily be solved analytically, the flux distribution in both the x and y dimensions are cosines. The complete description of this benchmark problem is given in Section C.1 of Appendix C.

The problem was solved at several spatial mesh sizes using extremely tight flux and eigenvalue convergence criteria (10^{-10}). The results of this study are given in Table 4-3, which presents the eigenvalue error and maximum error in the nodal power density at various mesh sizes for the CMFD method, quadratic nodal method, cubic nodal method, and quartic nodal method options of the QUAGMIRE code. In addition, Figure 4-1 and Figure 4-2 plot the eigenvalue error versus mesh size for coarse and very fine meshes respectively. Figure 4-2 shows that for mesh sizes between 5.0 and 6.0 cm both the cubic and quartic nodal methods overshoot the reference eigenvalue, and then begin to converge to the reference eigenvalue as the mesh size is further refined.

Finite difference methods will exactly reproduce the reference flux distribution of bare core problems for all spatial meshes, however they produce relatively large errors in the eigenvalue when coarse spatial meshes are used. Table 4-3 shows that the quadratic nodal method also exactly reproduces the nodal power density for every spatial mesh size, and it also produces relatively large errors in the eigenvalue when coarse meshes are used. Figure 4-3, which plots the eigenvalue error versus the square of the spatial mesh size (h^2), shows that the spatial discretization error is $O(h^2)$ for both the CMFD method and the quadratic nodal method.

Table 4-3 shows that both the cubic nodal method and the quartic nodal method produce accurate estimates of the nodal power density for all mesh sizes. The maximum error in the nodal power density is less than 0.5% and decreases to zero as the mesh size is refined. Figure 4-4, which plot the eigenvalue error versus h^4, shows that for coarse meshes the spatial discretization error is approximately $O(h^4)$ for both the cubic and quartic nodal methods. Since the quartic nodal method uses a fourth-order polynomial expansion to approximate the transverse-integrated flux the spatial discretization error is expected to be $O(h^4)$. Similarly, the cubic nodal method is expected to have a spatial discretization error of $O(h^3)$. The higher than expected order of the spatial discretization error which is exhibited by the cubic nodal method is due to a fortuitous cancellation of error related to the use of a uniform mesh.

Clearly, the cubic and quartic nodal methods enable the use of significantly larger spatial meshes to produce solutions of similar accuracy than traditional finite difference methods. For example, in order to produce an eigenvalue error of 10^{-4} the quartic nodal method required a 10.0 cm mesh, while the CMFD method required a 1.5 cm mesh.

Table 4-3

Two-Group Bare Core Problem: Errors at Selected Mesh Sizes

	h	CMFD Method		Quadratic Nodal Method	
N	(cm)	ε_λ[a]	ε_{max} (%)	ε_λ	ε_{max} (%)
3	20.0	2.17×10^{-2}	0.00	-2.23×10^{-2}	0.00
4	15.0	1.23×10^{-2}	0.00	-1.25×10^{-2}	0.00
5	12.0	7.91×10^{-3}	0.00	-7.99×10^{-3}	0.00
6	10.0	5.50×10^{-3}	0.00	-5.54×10^{-3}	0.00
8	7.5	3.10×10^{-3}	0.00	-3.11×10^{-3}	0.00
10	6.0	1.99×10^{-3}	0.00	-1.99×10^{-3}	0.00
12	5.0	1.38×10^{-3}	0.00	-1.38×10^{-3}	0.00
16	3.75	7.76×10^{-4}	0.00	-7.77×10^{-4}	0.00
20	3.0	4.97×10^{-4}	0.00	-4.97×10^{-4}	0.00
24	2.5	3.45×10^{-4}	0.00	-3.45×10^{-4}	0.00
30	2.0	2.21×10^{-4}	0.00	-2.21×10^{-4}	0.00
40	1.5	1.24×10^{-4}	0.00	-1.24×10^{-4}	0.00
60	1.0	5.52×10^{-5}	0.00	-5.52×10^{-5}	0.00

	h	Cubic Nodal Method		Quartic Nodal Method	
N	(cm)	ε_λ	ε_{max} (%)	ε_λ	ε_{max} (%)
3	20.0	-2.13×10^{-3}	0.00	-1.91×10^{-3}	0.40
4	15.0	-1.07×10^{-3}	0.27	-9.76×10^{-4}	0.36
5	12.0	-4.01×10^{-4}	0.42	-3.58×10^{-4}	0.45
6	10.0	-1.57×10^{-4}	0.18	-1.35×10^{-4}	0.20
8	7.5	-2.69×10^{-5}	0.07	-1.94×10^{-5}	0.07
10	6.0	-3.82×10^{-6}	0.02	-6.42×10^{-7}	0.03
12	5.0	7.51×10^{-7}	0.02	2.30×10^{-6}	0.02
16	3.75	1.34×10^{-6}	0.01	1.84×10^{-6}	0.01
20	3.0	8.37×10^{-7}	0.01	1.04×10^{-6}	0.01
24	2.5	4.98×10^{-7}	0.01	5.96×10^{-7}	0.01
30	2.0	2.43×10^{-7}	0.00	2.84×10^{-7}	0.00
40	1.5	8.95×10^{-8}	0.00	1.02×10^{-7}	0.00
60	1.0	2.01×10^{-8}	0.00	2.27×10^{-8}	0.00

[a] Reference eigenvalue = 0.946900410386976

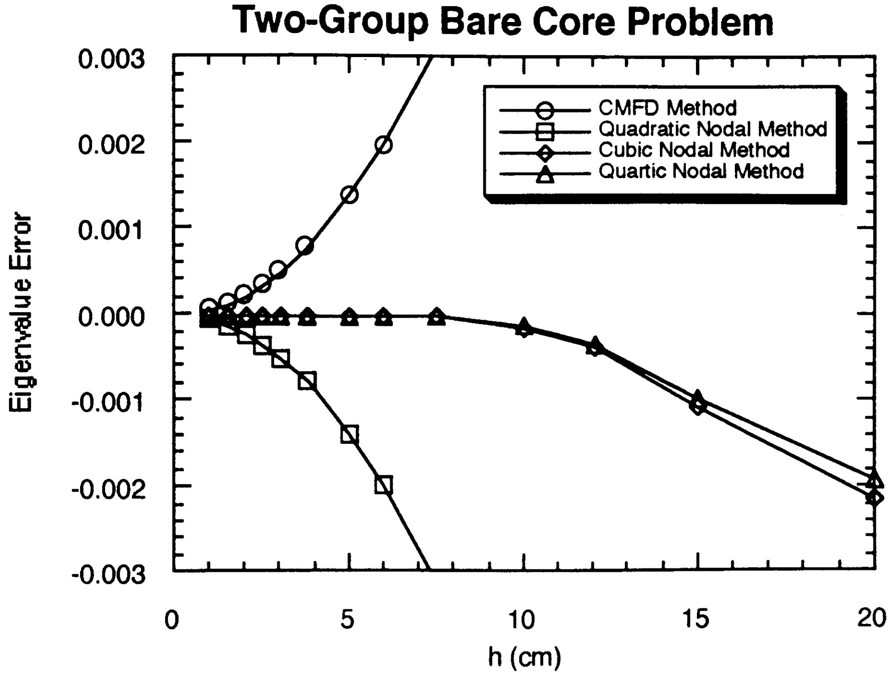

Figure 4-1. Two-Group Bare Core Problem: Eigenvalue Error versus Mesh Size.

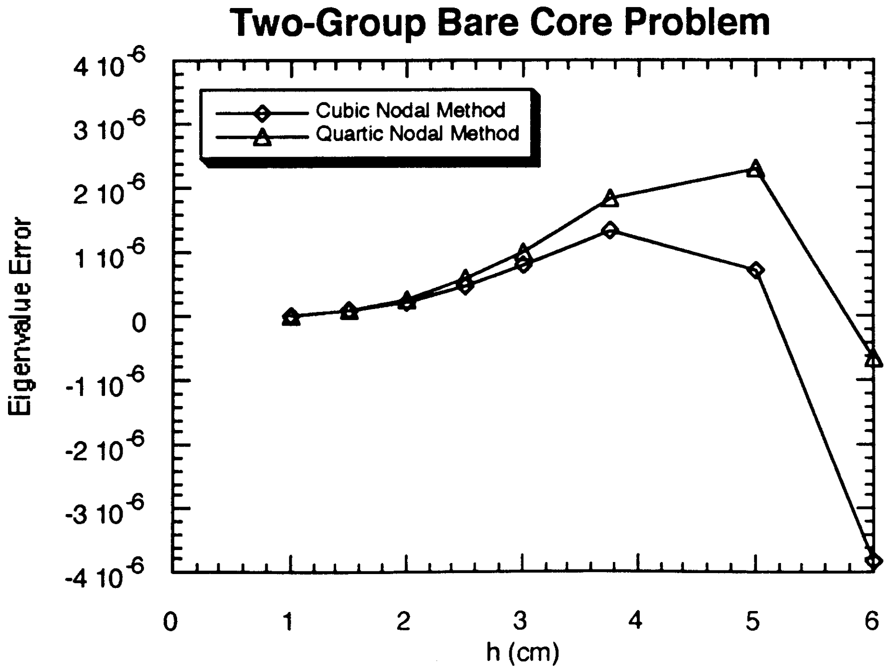

Figure 4-2. Two-Group Bare Core Problem: Eigenvalue Error versus Mesh Size (Very Fine Mesh).

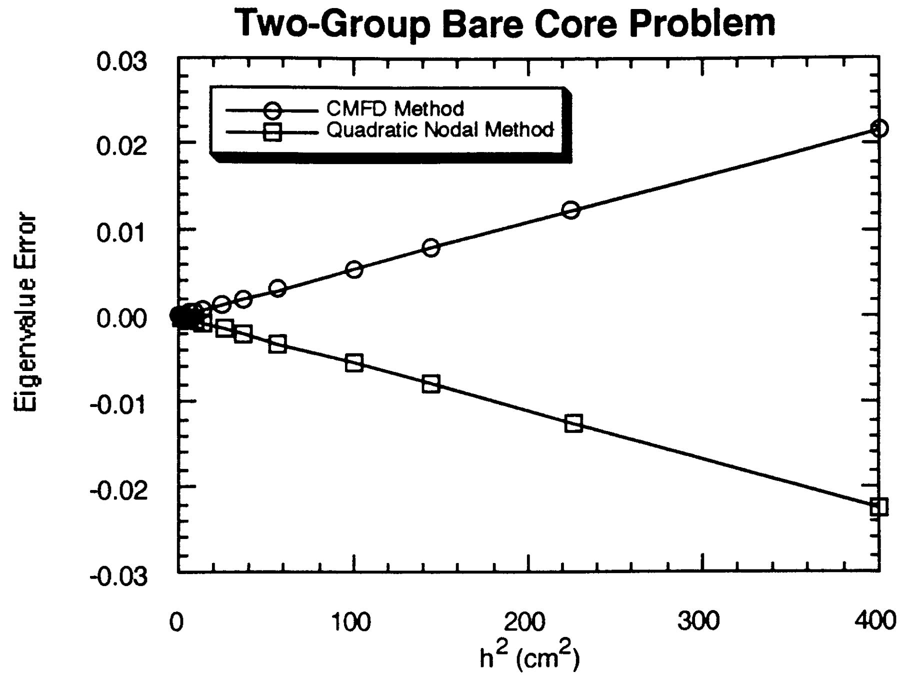

Figure 4-3. Two-Group Bare Core Problem: Eigenvalue Error versus h^2.

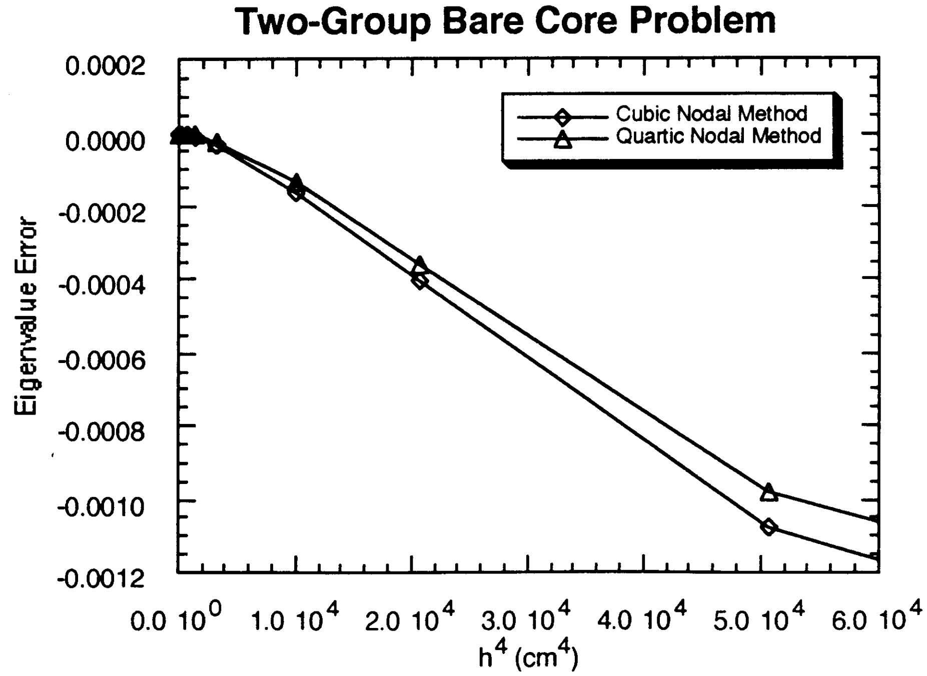

Figure 4-4. Two-Group Bare Core Problem: Eigenvalue Error versus h^4.

4.3.2 Seven-Group Homogeneous Bare Core Benchmark Problem

This problem, BSS-3 from the Argonne Benchmark Book [A2], was originally developed to verify the performance of multigroup finite difference codes. It consists of a quarter core section of a two-dimensional, homogeneous bare core with zero flux external boundary conditions. The quarter core dimensions are 67.5 cm in the x direction and 13.5 cm in the y direction. The 7-group cross sections and energy spectrum are characteristic of graphite moderated reactors and include upscattering. This problem may also be solved analytically. The specifications for this benchmark problem are presented in Section C.2 of Appendix C.

This problem was modelled with 7.5 cm × 4.5 cm nodes using the CMFD method, the quadratic nodal method, the cubic nodal method, and the quartic nodal method. The results are summarized in Table 4-4. The quartic nodal method provides the most accurate estimate of the eigenvalue, the error in the eigenvalue is approximately 9.0×10^{-6}. To achieve a similar error in the reactor eigenvalue a finite difference method would require a uniform mesh 0.2 cm, an increase in the number of unknowns by a factor of 840. The error in the nodal power densities is very low for all of the methods, $\varepsilon_{max} < 0.03\ \%$. A map of the reference nodal power density and the errors in the nodal power density is provided in Figure D-1. These results verify that the groupwise solution method used by the QUAGMIRE code will correctly model problems with upscattering.

A small discrepancy exists for the CMFD method, the nonzero error in nodal power densities is due to the incomplete spectral convergence of the group flux vectors. The group fluxes are converged spatially. However, there is a slight error in the group-to-group flux ratios. The errors are not large enough to warrant serious consideration, however they may be reduced further through the use of a tighter flux convergence criterion and/or two or more inner iterations per outer iteration.

Table 4-4

Summary of Results for the Seven-Group Homogeneous Bare Core Benchmark Problem

	CMFD Method	Nodal Methods		
		Quadratic	Cubic	Quartic
# Unknowns	189	651	651	651
# Outer Iterations[a]	38	39	38	38
Eigenvalue[b]	0.782194	0.766878	0.774502	0.774536
ε_λ	7.65×10^{-3}	-7.67×10^{-3}	-4.32×10^{-5}	-8.97×10^{-6}
ε_{max} (%)	0.02	0.03	0.02	0.02
Execution Time (Mac SE/30)	17.72	30.63	63.77	94.68

[a] Eigenvalue Shift = $\lambda + 0.3$, 1 inner/outer iteration, maximum of 16 flux/inner iterations

[b] Reference: 0.7745451357

4.3.3 2D IAEA PWR Benchmark Problem

The IAEA PWR problem is a highly simplified two- and three-dimensional, two-group static benchmark problem [A3]. The specifications for the IAEA PWR benchmark problem are provided in Section C.3 of Appendix C. The reactor consists of a two-zone core containing 177 fuel assemblies, each having a width of 20 cm. The core is reflected radially and axially by 20 cm of water, and the active core height is 340 cm. Nine fully-inserted control rods are represented as smeared absorbers in single fuel assemblies. In the three-dimensional configuration, four partially inserted control rods are also modelled. The existence of inserted control rods and a water reflector gives this problem severe local flux perturbations, making it a particularly challenging benchmark problem.

The 2D IAEA PWR problem was solved with 20 cm, 10 cm, and 5 cm spatial meshes in quarter-core geometry. Table 4-5 summaries the QUAGMIRE results for these cases. Core maps of the error and relative error in the normalized assembly power density are presented in Figures D-2 and D-3, respectively. The reference solution is a spatially converged 3-1/3 cm IQSBOX calculation by Wagner [W2]. The maximum error and maximum relative error in the assembly power density are 1.18% and 2.01% for assembly-sized nodes. The assembly with the largest relative error in the power density is one of the low power assemblies adjacent to the reflector. Errors in the reactor eigenvalue and assembly power density decrease rapidly as the spatial mesh is reduced. With a 5 cm spatial mesh the solution is nearly spatially converged.

Finite difference methods require a spatial mesh of 1.25 cm to achieve similar accuracy [A3]. Wagner reported that the finite difference code VENTURE required 930 seconds on an IBM 360/91 to solve this problem with a uniform 1.25 cm mesh [W2].

A comparison of results for the 2D IAEA PWR problem from several nodal methods is presented in Table 4-6 and Table 4-7. QPANDA is a quartic polynomial nodal method and the neutronic method used in the SIMULATE-3 code [S5]. QUANDRY [S2] is an analytic nodal method and IQSBOX [W2] is fifth-order nodal expansion method. Table 4-6 summarizes the results for assembly-sized nodes and Table 4-7 summarizes the results for solutions with four nodes per assembly. The accuracy of QUAGMIRE is comparable to the other nodal codes. For solutions with four nodes per assembly the accuracy of QUAGMIRE is superior to the other codes.

Figure 4-5 and Figure 4-6 present traverses of the transverse-integrated, x-directed fast and thermal fluxes, respectively, along the core centerline (j = 1) for several spatial mesh sizes. Figure 4-5 shows that the quartic flux expansion provides a very good approximation to the spatial shape of the fast flux for all of the spatial mesh sizes. Figure 4-6 shows that the quartic flux expansion is a very good approximation to the spatial shape of the thermal flux for the 10×10 cm and 5×5 cm mesh sizes. In general, the quartic flux expansion is also a good approximation to the shape of the thermal flux for the 20×20 cm mesh, except for the node adjacent to the core/reflector interface. In this node the shape of the thermal flux is significantly in error, indicating a smaller mesh size should be used.

Table 4-5

Summary of Results for the 2D IAEA PWR Benchmark Problem

	Mesh Spacing		
	20 x 20 cm	10 x 10 cm	5 x 5 cm
# unknowns	762	2546	9912
# outer iterations [a]	22	18	22
Eigenvalue [b]	1.029528	1.029605	1.029585
ε_{max} (%)	1.18	0.07	0.01
$\bar{\varepsilon}$ (%)	0.69	0.02	0.004
ε_{rel} (%)	2.01	0.10	0.02
$\bar{\varepsilon}_{rel}$ (%)	0.74	0.02	0.004
Execution time (sec SGI 4D/210)	3.16	9.11	50.80

[a] 1 inner/outer iteration, maximum of 16 flux/inner iterations

[b] Reference: 1.029585

Table 4-6

Summary of Results for the 2D IAEA PWR Benchmark Problem

Obtained by Several Nodal Codes with a 20 cm Mesh

	QUAGMIRE	QPANDA [S6]	QUANDRY [S2]	IQSBOX [W2]
Eigenvalue [a]	1.029528	1.02955	1.02962	1.029657
ε_{max} (%)	1.18	2.2	0.56	
$\bar{\varepsilon}$ (%)	0.69	1.0	0.25	
ε_{rel} (%)	2.01	3.2	0.94	1.4
$\bar{\varepsilon}_{rel}$ (%)	0.74	1.1	0.27	
Execution time (sec)	3.16 [b]		1.24 [c]	0.86 [d]
Symmetry	1/4 core	1/8 core	1/8 core	1/8 core

[a] Reference: 1.029585

[b] SGI 4D/210

[c] IBM 370/168

[d] CDC CYBER 175

Table 4-7

Summary of Results for the 2D IAEA PWR Benchmark Problem

Obtained by Several Nodal Codes with a 10 cm Mesh

	QUAGMIRE	QPANDA [S6]	QUANDRY [S2]	IQSBOX [W2]
Eigenvalue [a]	1.029605	1.02962	1.02960	1.029611
ε_{max} (%)	0.07	0.2	0.22	
$\bar{\varepsilon}$ (%)	0.02	0.1	0.10	
ε_{rel} (%)	0.10	0.3	0.32	0.3
$\bar{\varepsilon}_{rel}$ (%)	0.02	0.1	0.11	
Execution time (sec)	9.11[b]		6.7 [c]	1.34 [d]
Symmetry	1/4 core	1/8 core	1/8 core	1/8 core

[a] Reference: 1.029585

[b] SGI 4D/210

[c] IBM 370/168

[d] CDC CYBER 175

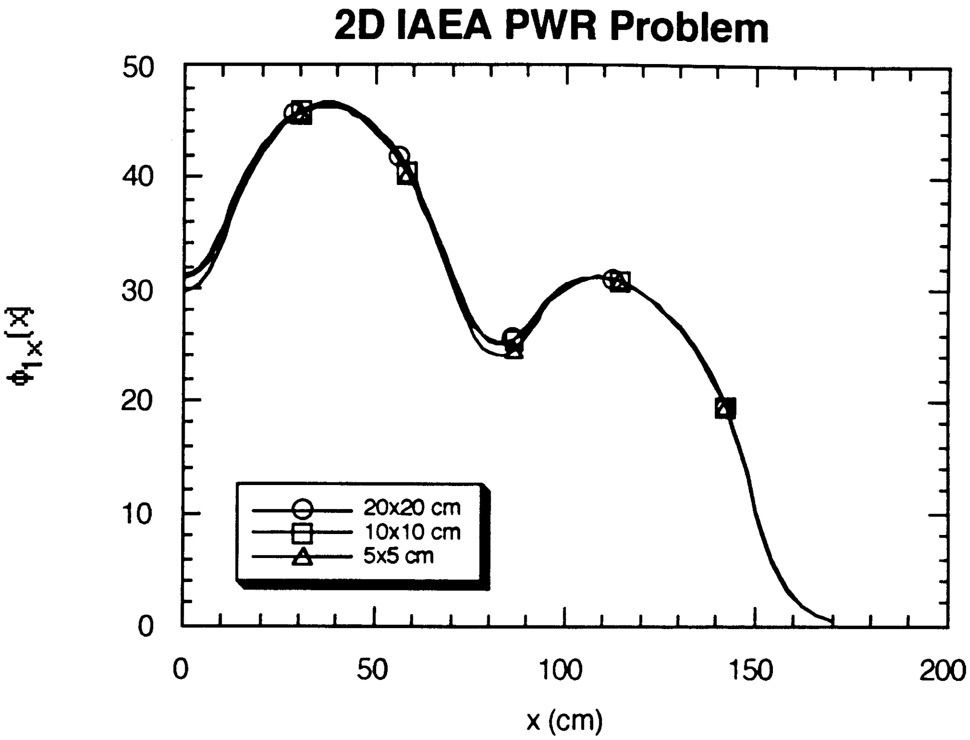

Figure 4-5. 2D IAEA PWR Benchmark Problem: Traverse of the Transverse-Integrated, X-Directed Fast Flux Along the Core Centerline (j = 1) for Several Spatial Mesh Sizes.

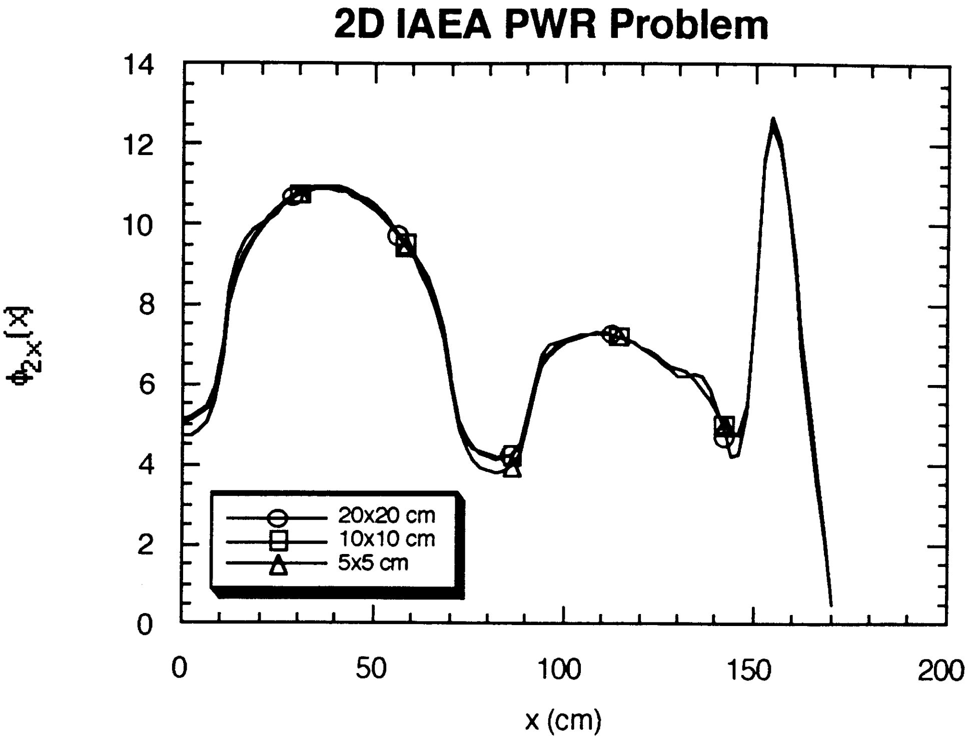

Figure 4-6. 2D IAEA PWR Benchmark Problem: Traverse of the Transverse-Integrated, X-Directed Thermal Flux Along the Core Centerline (j = 1) for Several Spatial Mesh Sizes.

4.3.4 2D LRA BWR Static Benchmark Problem

The LRA BWR static benchmark problem is based on the LRA BWR problem, a highly simplified two- and three-dimensional, two-group kinetics benchmark problem [A3]. The static benchmark problem is described in Section C.4 of Appendix C. The problem consists of a BWR with a two-zone core containing 312 fuel assemblies, each 15 cm wide. The core is reflected both radially and axially by 30 cm of pure water, and the active core height is 300 cm. The control blades are represented as smeared absorbers in the four adjacent fuel assemblies. Nine control blades are modelled in their fully-withdrawn positions. As a result, the flux distribution displays severe local perturbations. Although this problem is unlike a commercial BWR, the severe flux peaking makes this problem more difficult to solve than a real BWR.

The 2D LRA BWR problem was solved with uniform 15 cm, 7.5 cm, and 5 cm spatial meshes in quarter-core geometry. Table 4-8 summarizes the QUAGMIRE results for these solutions. These solutions use a quadratic transverse-leakage approximation in the core and a flat transverse-leakage approximation in the reflector. The error and relative error in the normalized assembly power densities are displayed in Figure D-4 and Figure D-5, respectively. The reference solution is a 16 node per assembly calculation by Shober [S1]. For assembly-sized nodes the maximum error in the assembly power density of 1.18 % occured in one of the uncontrolled assemblies on the diagonal. The maximum relative error of 1.41 % occured in the uncontrolled assembly in the center of the core, a low power region in the core. Both errors are quite reasonable for this problem. The errors decrease rapidly as the mesh size is refined and are effectively negligible for the 4 nodes per assembly case.

The QUAGMIRE results are compared to the results from QUANDRY for assembly-sized nodes in Table 4-9. The errors in the assembly power density from QUANDRY are significantly smaller than from QUAGMIRE. This is believed to be due to the use of the flat transverse-leakage approximation in the reflector. However, empirically it has been found that the use of a flat transverse-leakage approximation in the reflector for problems with deep reflector will prevent negative node-averaged fluxes and guarantee numerical stability.

When comparing the number of unknowns required by different computer codes it is often more illustrative to compare the physical unknowns. The physical unknowns in QUAGMIRE are the node-averaged fluxes and the u-directed face-averaged net-currents. In QUANDRY the physical unknowns are the node-averaged fluxes and the u-directed node-averaged leakages. Thus, QUAGMIRE requires slightly more physical unknowns than QUANDRY, one more per row per direction per group. For the 2D LRA BWR problem with assembly sized nodes Table 4-9 shows that, correcting for the difference in symmetry, the number of physical unknowns required by QUAGMIRE and QUANDRY is approximately equivalent.

Figure 4-7 and Figure 4-8 present traverses of the transverse-integrated, x-directed fast and thermal flux, respectively, along the core centerline ($j = 1$) for several spatial mesh sizes. Figure 4-7 shows that the quartic flux expansion provides a good approximation to the spatial shape of the fast flux for the 7.5x7.5 cm and 5x5 cm mesh sizes. The shape of the fast flux for the 15x15 cm mesh solution is in error in the uncontrolled assemblies. Figure 4-8 shows that the quartic flux expansion is a very good approximation to the shape of the thermal flux for the 7.5x7.5 cm and 5x5 cm mesh sizes. However, for the 15x15 cm mesh, there is a significant error in the shape of the thermal flux in the uncontrolled assemblies, indicating that the quartic flux expansion is not adequate for this mesh size.

Table 4-8

Summary of Results for the 2D LRA BWR Static Benchmark Problem

	Mesh Spacing		
	15 × 15 cm	7.5 × 7.5 cm	5 × 5 cm
# unknowns	1298	5016	11154
# outer iterations [a]	24	19	22
Eigenvalue [b]	0.996328	0.996376	0.996368
ε_{max} (%)	1.18	0.19	0.07
$\bar{\varepsilon}$ (%)	0.39	0.04	0.02
ε_{rel} (%)	1.41	0.14	0.07
$\bar{\varepsilon}_{rel}$ (%)	0.42	0.04	0.02
Execution time (sec SGI 4D/210)	6.50	21.25	58.77

[a] 1 inner/outer iteration, maximum of 32 flux/inner iterations

[b] Reference: 0.99636

Table 4-9

Comparison of Results for the 2D LRA BWR Static Benchmark Problem with Assembly-Sized Nodes

	QUAGMIRE	QUANDRY [S2]
Physical unknowns	770	396
Eigenvalue [a]	0.996328	0.99641
ε_{max} (%)	1.18	0.30
$\bar{\varepsilon}$ (%)	0.39	0.07
ε_{rel} (%)	1.41	0.19
$\bar{\varepsilon}_{rel}$ (%)	0.42	0.07
Execution time (sec)	6.50 [b]	2.7 [c]
Symmetry	1/4 core	1/8 core

[a] Reference: 0.99636

[b] SGI 4D/210

[c] IBM 370/168

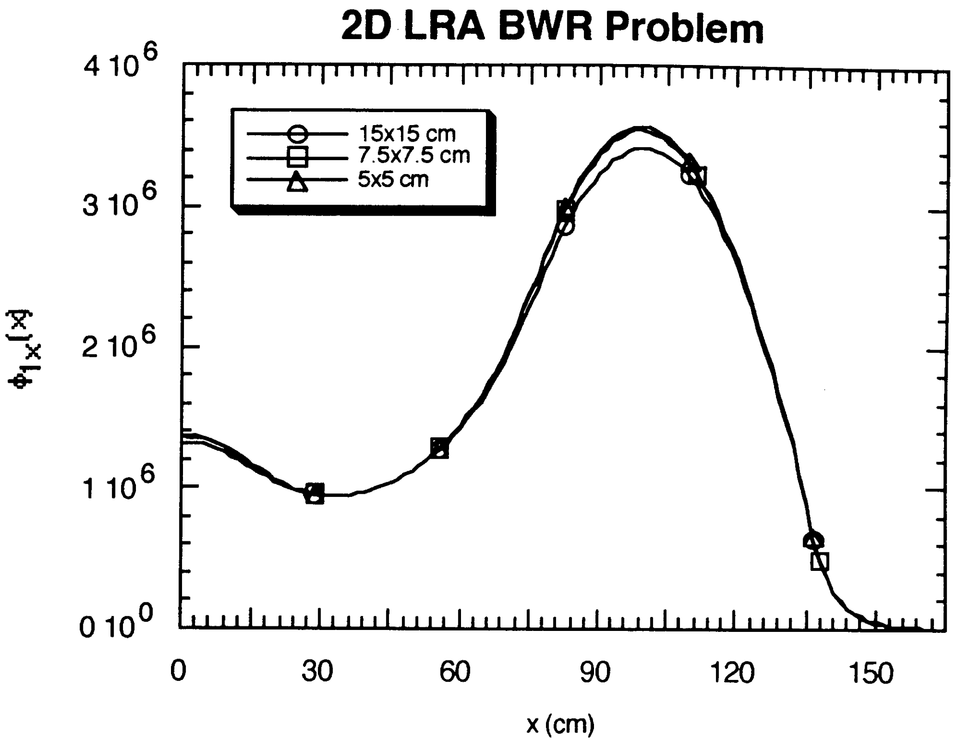

Figure 4-7. 2D LRA BWR Static Benchmark Problem: Traverse of the Transverse-Integrated, X-Directed Fast Flux Along the Core Centerline (j = 1) for Several Spatial Mesh Sizes.

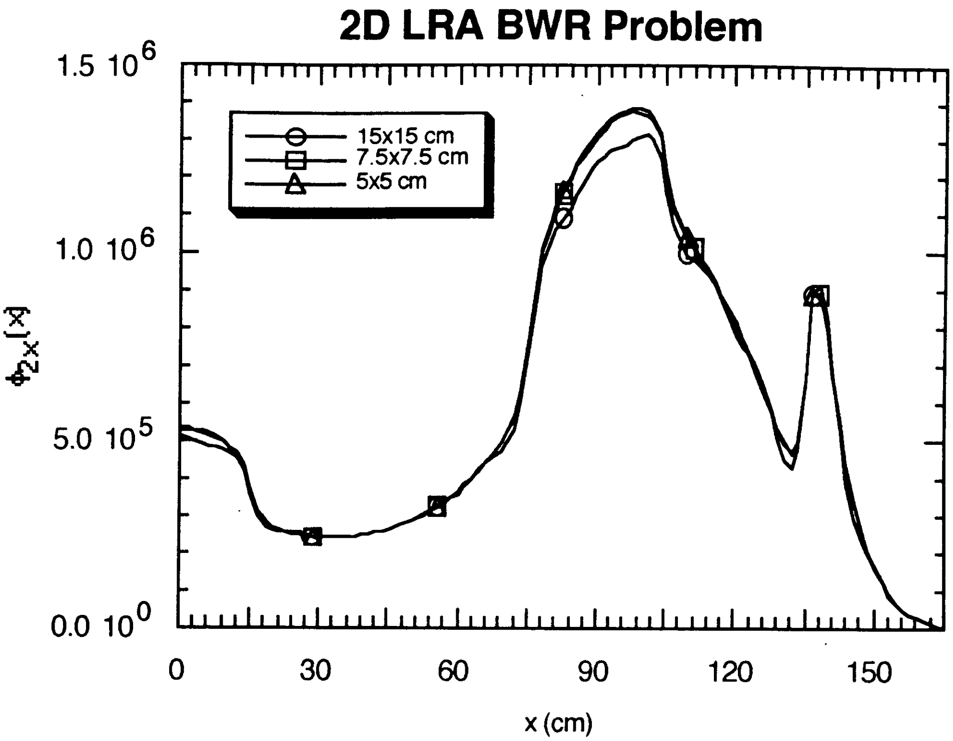

Figure 4-8. 2D LRA BWR Static Benchmark Problem: Traverse of the Transverse-Integrated, X-Directed Thermal Flux Along the Core Centerline (j = 1) for Several Spatial Mesh Sizes.

4.3.5 2D LMFBR Static Benchmark Problem

The LMFBR static benchmark problem is a simplified model of the MARK I core design of the SNR 300 prototype LMFBR at beginning-of-life [A4,B4]. The benchmark is designed to model the physics and geometry that are characteristic of LMFBRs. It consists of two- and three-dimensional, four-group, static neutron diffusion problems in triangular-z and x-y-z geometries. The specifications for the x-y-z version of the benchmark problem are provided in section C.5 of Appendix C. The x-y-z version of the benchmark models a quadrant of the reactor. The benchmark defines materials for the inner core, outer core, radial blanket, axial blanket, control rod, and control rod follower regions. In the 3D problem the control rods in the inner core are modelled in their fully-withdrawn position at the upper core/blanket interface and the control rods in the outer core are partially-inserted. The two-dimensional benchmark models two horizontal slices of the reactor, one of the lower core (rods out) with the control rods in the outer core withdrawn and the other of the upper core (rods in) with the control rods in the outer core inserted.

In this section the results of the 2D LMFBR problem are presented. A uniform spatial mesh of 5.4 cm is used throughout the reactor except along the external boundary where a 8.1 cm spatial mesh is used, 19×19 spatial meshpoints. Table 4-10 summarizes the results for the rods out and rods in problems using quadratic, cubic, and quartic flux expansions. The reference solution for the 2D LMFBR problem was taken to be a finite difference solution by Buckel [A4], obtained using the CITATION code. Buckel actually performed a series of calculations with refined mesh spacings and applied a Richardson extrapolation, assuming that the errors were reduced with the square of the mesh spacing, to obtain a reference solution in which the mesh spacing had been extrapolated to zero. For the quartic flux expansion the eigenvalue error for both the rods out problem, 2.3×10^{-5}, and the rods in problem, 1×10^{-6}, are extremely small. In Table 4-11 the quartic results are compared to the NEMBOX nodal code and the CITATION finite difference code. NEMBOX [F3] is a multigroup version of NEM in which the flux is expanded using fourth-order polynomials. CITATION [F4] is a mesh-centered finite-difference method. The accuracy of QUAGMIRE is slightly superior to NEMBOX. CITATION would require a spatial mesh of approximately 0.25 cm in order to yield similar accuracy.

Table 4-10

Summary of Results for the 2D LMFBR Static Benchmark Problem

		Nodal Methods		
		Quadratic	Cubic	Quartic
Rods Out	# unknowns/group	1881	1881	1881
	# outer iterations [a]	20	20	20
	Eigenvalue	1.246765	1.246763	1.247133
	Eigenvalue error [b]	2.3×10^{-5}	2.1×10^{-5}	3.91×10^{-4}
	Execution time (sec SGI 4D/210)	39.92	32.72	25.45
Rods In	# unknowns/group	1881	1881	1881
	# outer iterations [a]	15	15	15
	Eigenvalue	1.110015	1.110073	1.111325
	Eigenvalue error [b]	1×10^{-6}	5.8×10^{-5}	1.309×10^{-3}
	Execution time (sec SGI 4D/210)	28.29	23.25	17.85

[a] Eigenvalue shift = $\lambda + 1.0$, 1 inner/outer iteration, maximum of 32 flux/inner iterations

[b] Reference: 1.246742 Rods Out, 1.110016 Rods In

Table 4-11

Comparison of Results for the 2D LMFBR Static Benchmark Problem

Problem	Code	Meshpoints	Eigenvalue	Eigenvalue Error	Execution Time (sec)[a]
Rods Out	QUAGMIRE	19x19	1.246765	2.3×10^{-5}	39.92
	NEMBOX [F3]	19x19	1.24677	2.8×10^{-5}	
	CITATION [A4]	20x20	1.248374	1.632×10^{-3}	6
		39x39	1.247148	4.06×10^{-4}	29
		59x59	1.246926	1.84×10^{-4}	82
		79x79	1.246834	9.2×10^{-5}	179
		∞ [b]	1.246742		
Rods In	QUAGMIRE	19x19	1.110016	1×10^{-6}	28.29
	NEMBOX	19x19	1.10998	-3.6×10^{-5}	
	CITATION	20x20	1.116772	6.756×10^{-3}	6
		39x39	1.111857	1.841×10^{-3}	31
		59x59	1.110778	7.62×10^{-4}	85
		79x79	1.110397	3.81×10^{-4}	183
		∞ [b]	1.110016		

[a] QUAGMIRE SGI 4D/210, CITATION IBM 370/168

[b] Richardson extrapolation to $h = 0$

4.3.6 CISE BWR Benchmark Problem

The CISE BWR benchmark problem [B3] is an idealized model of a two-dimensional, two-group BWR which explicitly represents many of the heterogeneities that are present in BWRs. The CISE BWR core consists of 208 fuel assemblies, each 15 cm in width, and is surrounded radially by a 15 cm water reflector. The core is arranged in a checker board pattern with fresh and depleted fuel assemblies. Thirteen control blades are modelled in their inserted positions. The fuel region, control blade, and water gaps are explicitly modelled in each fuel assembly. The major simplification in this benchmark problem is that the actual heterogeneities in the fuel region (enrichment zones, burnable poison rods, and water rods) are not explicitly represented but are modelled homogeneously for the entire fuel region. The specifications for the CISE BWR problem are provided in Section C.6 of Appendix C.

The reference solution to the CISE BWR benchmark problem is a QUANDRY solution [S3] using 64 nodes per assembly (25 in the fuel region, 11 in each quarter of the control blade, and 28 in the water gaps). The heterogeneities in each fuel assembly are explicitly represented in the reference solution. Because it explicitly models many BWR heterogeneities, the CISE BWR problem has been used to benchmark spatial homogenization methods [S3]. Assembly homogenization parameters may be determined by modelling each fuel assembly type using zero net-current boundary conditions [S4]. Assembly homogenized cross sections (AXS) may be determined using the conventional flux-volume weighting procedure. Assembly discontinuity factors (ADFs) for each fuel assembly type may be determined by taking the ratio of the surface-averaged flux to the assembly-averaged flux for each surface of the assembly and each energy group. Smith [S3] used QUANDRY to determine the AXS and ADFs for the CISE BWR problem. The QUANDRY AXS and ADFs for the CISE BWR problem are also provided in Section C.6 of Appendix C.

The CISE BWR problem was solved by QUAGMIRE using AXS and ADFs. The QUAGMIRE solution was performed using a quartic flux expansion with a quadratic transverse-leakage approximation in the core and a flat transverse-leakage approximation in the reflector. The QUAGMIRE solution is summarized in Table 4-12, and it is compared a QUANDRY solution using AXS and ADFs. The error in the normalized assembly power densities is presented in Figure D-6. The QUAGMIRE solution compares well with the QUANDRY solution using AXS and ADFs, however the errors in the eigenvalue and nodal power densities are slightly larger than the equivalent QUANDRY solution.

Table 4-12

Summary of Results for the CISE BWR Benchmark Problem

	QUAGMIRE	QUANDRY [S3]
# outer iterations [a]	21	
Eigenvalue error (%)[b]	-0.060	-0.03
ε_{max} (%)	3.17	2.73
$\bar{\varepsilon}$ (%)	1.06	0.88
ε_{rel} (%)	2.94	3.06
$\bar{\varepsilon}_{rel}$ (%)	1.10	0.90
Execution time (sec SGI 4D/210)	3.44	

[a] Eigenvalue shift = $\lambda + 0.05$, 1 inner/outer iteration, maximum of 32 flux/inner iterations

[b] Reference: 0.95240

4.3.7 HAFAS BWR Benchmark Problem

The HAFAS (Heterogeneously-Arranged Fuel Assembly) BWR problem more accurately models the heterogeneities present in BWR fuel assemblies than the CISE BWR problem. It was originally developed to benchmark assembly homogenization method [S3]. In the HAFAS BWR benchmark problem radial enrichment zones in the fuel region of the assemblies are explicitly represented. Sixteen enrichment zones in each fuel assembly are modelled, each zone consisting of a cluster of four fuel pins with constant enrichment. The radial enrichment zones in each fuel assembly type are modelled using three different fuel enrichments. Both wide and narrow water gaps are explicitly modelled in each fuel assembly. In addition, several of the central fuel assemblies are modelled as partially voided (both 40% and 70% voided).

The HAFAS BWR problem is a two-dimensional, two-group model of a BWR. The reactor core consists of 308 fuel assemblies, each 15.31 cm in width, and the core is surrounded by a 15.31 cm water reflector. The reflector is deeper along the reactor diagonal. The core is arranged in a checker board pattern with fresh and depleted assemblies. Sixteen control blades are modelled in their inserted positions. The specifications for this benchmark problem are provided in Section C.7 of Appendix C.

The reference solution to the HAFAS BWR problem is a QUANDRY [S3] solution using 49 nodes per assembly (16 in the fuel region, 9 in each quarter of a control blade, and 24 in the water gap regions). QUANDRY was also used to determine the assembly homogenization parameters, assembly cross sections (AXS) and assembly discontinuity factors (ADFs), for each fuel assembly type. The QUANDRY assembly homogenization parameters [S3] for this problem are also provided in Section C.7 of Appendix C.

The HAFAS BWR problem was solved by QUAGMIRE using AXS and ADFs. The QUAGMIRE solution was performed using a quartic flux expansion with a quadratic transverse-leakage approximation in the core and a flat transverse-leakage approximation in the reflector. The QUAGMIRE solution is summarized in Table 4-13 and it is compared to a QUANDRY solution using AXS and ADFs. The error in the QUAGMIRE normalized assembly power densities is displayed in Figure D-7. The QUAGMIRE solution compares well to the QUANDRY solution using AXS and ADFs. Is is actually slightly more accurate than the equivalent QUANDRY solution. These results and the results from the CISE BWR problem verify that the flux discontinuity factors have been correctly incorporated into the QUAGMIRE nodal method. In addition, they verify that the polynomial nodal method with a quartic flux expansion used by QUAGMIRE yields results comparable to the analytic nodal method used by QUANDRY.

Table 4-13

Summary of Results for the HAFAS BWR Benchmark Problem

	QUAGMIRE	QUANDRY [S3]
# outer iterations [a]	19	
Eigenvalue error (%)[b]	-0.067	-0.06
ε_{max} (%)	5.84	5.91
$\bar{\varepsilon}$ (%)	1.20	1.22
ε_{rel} (%)	5.23	5.29
$\bar{\varepsilon}_{rel}$ (%)	1.29	1.33
Execution time (sec SGI 4D/210)	4.17	

[a] Eigenvalue shift = $\lambda + 0.02$, 1 inner/outer iteration, maximum of 32 flux/inner iterations

[b] Reference: 1.04420

4.3.8 Two-Group Source Benchmark Problem

The Two-Group Source benchmark problem is a simple model of a two-dimensional, two-group bare core with extraneous neutron sources. This benchmark was originally developed by Jacqmin [J2] to validate a new version of the QUANDRY analytic nodal method [J1] which had been extended to model the effects of extraneous neutron sources. The reactor consists of sixteen assemblies, each 21 cm wide. A uniform extraneous neutron source is present in each assembly, and the reactor has zero flux boundary condition on all external reactor boundaries. The problem may be modelled in quarter core geometry. Specifications for the Two-Group Source benchmark problem are provided in Section C.8 of Appendix C.

The Two-Group Source benchmark problem was solved by QUAGMIRE using 1x1 and 2x2 nodes per assembly. The QUAGMIRE solutions were obtained using a quartic flux expansion and a quadratic transverse-leakage approximation throughout the reactor. The results are summarized in Table 4-14. The reference is a CITATION solution, mesh-centered finite difference method, with a uniform 1.0 cm mesh (21x21 nodes/assembly) [J2]. Table 4-14 also compares the QUAGMIRE results to a 1x1 nodes per assembly QUANDRY solution [J2]. Figure D-8 presents the relative error in the group-1 and group-2 node-averaged flux distributions. With assembly sized nodes QUAGMIRE produces a maximum relative error in the group 1 and group 2 fluxes of 2.15% and 2.38%, respectively. However, the 2x2 nodes per assembly QUAGMIRE solution yields a maximum error in the group-1 and group-2 fluxes of 0.29% and 0.45%, respectively, which is smaller than the 1x1 QUANDRY solution.

Table 4-14

Summary of Results for the Two-Group Source Benchmark Problem

	QUAGMIRE (1×1)	QUAGMIRE (2×2)	QUANDRY [J2] (1×1)
Group-1 Flux, ε_{rel}	2.15 %	0.29 %	0.52 %
Group-1 Flux, $\bar{\varepsilon}_{rel}$	1.80 %	0.13 %	0.22 %
Group-2 Flux, ε_{rel}	2.38 %	0.45 %	0.57 %
Group-2 Flux, $\bar{\varepsilon}_{rel}$	1.83 %	0.21 %	0.22 %

4.4 3D STATIC RESULTS

In this section, results from three 3D static benchmark problems are presented. As with the 2D problems, these problems contain large homogenized regions so that they may be analyzed using coarse spatial meshes. All of the results were obtained from the QUAGMIRE polynomial nodal method using a quartic (fourth-order) flux expansion. In addition, a relatively tight eigenvalue and pointwise flux convergence criteria of 10^{-6} has been used.

4.4.1 3D IAEA PWR Benchmark Problem

The 3D IAEA PWR benchmark problem was introduced in 1971 by Micheelson [M1] and has proven to be a very important standard for the comparison of reactor analysis method. Following the introduction of this benchmark problem, many solutions were obtained, but the large discrepancies in these solutions indicated that many of the existing multi-dimensional calculation methods were inadequate. The specifications for the 3D IAEA PWR benchmark problem are provided in Section C.3 of Appendix C.

The results of the QUAGMIRE solution to the 3D IAEA PWR problem are summarized in Table 4-15 for two different spatial meshes. The coarse mesh solution uses a 20 cm spatial mesh in both the radial and axial directions. The fine mesh solution uses a 10 cm radial mesh and a 20 cm axial mesh, except in the axial reflectors where a 10 cm mesh is used. Both solutions use a quartic flux expansion and a quadratic transverse-leakage approximation in the core and a flat transverse-leakage approximation in the reflector. The error and relative error in the normalized assembly power densities are given in Figure D-9 and Figure D-10, respectively.

The reference eigenvalue was taken from a finite difference solution by Vondy, obtained using the VENTURE code [A3]. Vondy performed a series of calculations with refined mesh spacings and applied a Richardson extrapolation to obtain a reference solution in which the mesh spacing was extrapolated to zero. The finest mesh

VENTURE solution used a 1-2/3 cm radial mesh and contained approximately 1.2 million meshpoints. However, Smith [S2] has indicated that the nodal power density from the extrapolated VENTURE solutions does not appear to be spatially converged. Therefore, the reference nodal power density for the 3D IAEA PWR problem was taken from a fine mesh IQSBOX solution by Finnemann [A3]. The IQSBOX solution used a fifth-order nodal expansion method with a 10x10x20(10) cm spatial mesh.

Table 4-16 presents a comparison between the coarse mesh nodal solutions by QUAGMIRE, QUANDRY, and IQSBOX. The errors in the QUAGMIRE and QUANDRY assembly power densities are comparable. The errors in the IQSBOX assembly power density are approximately half of the QUAGMIRE and QUANDRY solutions. This is consistent with the fact that IQSBOX uses a fifth-order flux expansion and the reference was a fine mesh IQSBOX solution.

As discussed in Section 4.3.4, the physical unknowns in QUAGMIRE are the node-averaged flux and the u-directed net-currents. For QUANDRY the physical unknowns are the node-averaged flux and the u-directed leakages. For IQSBOX the physical unknowns are the node-averaged flux and the u-directed incoming and outgoing partial currents. For the 3D IAEA PWR problem, Table 4-16 shows that, adjusting for differences in symmetry, the number of physical unknowns required by QUAGMIRE and QUANDRY are roughly equal. However, the number of physical unknowns required by IQSBOX is approximately 7/4 more than QUAGMIRE and QUANDRY.

Table 4-15

Summary of Results for the 3D IAEA PWR Benchmark Problem

	20×20×20 cm	10×10×20(10) cm
# unknowns	19998	76674
# outer iterations[a]	20	28
Eigenvalue[b]	1.029031	1.029059
ε_{max} (node, %)	1.32	0.83
$\bar{\varepsilon}$ (node, %)	0.34	0.25
ε_{rel} (node, %)	2.12	1.60
$\bar{\varepsilon}_{rel}$ (node, %)	0.43	0.33
ε_{max} (assembly, %)	0.87	0.57
$\bar{\varepsilon}$ (assembly, %)	0.31	0.21
ε_{rel} (assembly, %)	1.46	0.76
$\bar{\varepsilon}_{rel}$ (assembly, %)	0.33	0.21
Execution time (sec SGI 4D/210)	93.04	520.26

[a] Eigenvalue shift = $\lambda + 0.05$, 1 inner/outer iteration, maximum of 16 flux/inner iterations.

[b] Reference: 1.02903

Table 4-16

Comparison of Coarse Mesh 3D IAEA PWR Benchmark Solutions

	QUAGMIRE	QUANDRY [S2]	IQSBOX [A3]
Physical unknowns	11350	5776	10260
Eigenvalue[a]	1.029031	1.02902	1.02911
ε_{max} (assembly, %)	0.87	0.72	0.40
$\bar{\varepsilon}$ (assembly, %)	0.31	0.27	0.11
ε_{rel} (assembly, %)	1.46	1.18	0.57
$\bar{\varepsilon}_{rel}$ (assembly, %)	0.33	0.30	0.14
Symmetry	1/4 core	1/8 core	1/8 core
Execution time (sec)	93.04[b]	29.0[c]	50[d]

[a] Reference: 1.02903

[b] SGI 4D/210

[c] IBM 370/168

[d] CDC 6600

4.4.2 3D LRA BWR Static Benchmark Problem

The 3D LRA BWR benchmark problem was originally introduced as a full-core kinetics problem and has proven to be an extremely difficult benchmark problem. The static version of this benchmark problem is simply the initial condition of the transient problem. The specifications for the 3D LRA BWR Static benchmark problem are presented in Section C.4 of Appendix C.

A summary of the QUAGMIRE results for the 3D LRA BWR static benchmark problem is presented in Table 4-17. The coarse mesh solution uses a 15 cm radial mesh spacing and a 25 cm axial mesh spacing in the core and a 15 cm axial mesh spacing in the axial reflectors. The fine mesh solution uses a 7.5 cm radial mesh spacing and a 12.5 cm axial mesh spacing in the core and a 7.5 cm axial mesh spacing in the axial reflectors. The reference solution is a very fine mesh QUAGMIRE solution with a 5 cm radial mesh spacing and a 12.5 cm axial mesh spacing in the core and a 7.5 cm axial mesh spacing in the axial reflectors. All of the QUAGMIRE solution used a quartic flux expansion and a quadratic transverse-leakage approximation in the core and a flat transverse-leakage approximation in the reflector. The error and relative error in the normalized assembly power densities are provided in Figure D-11 and Figure D-12, respectively. The errors in the normalized assembly power densities for the 3D LRA BWR problem are similar to the errors in the 2D LRA BWR problem.

The coarse mesh QUAGMIRE and QUANDRY solutions are compared in Table 4-18. The number of physical unknowns, adjusting for the difference in symmetry, required by QUAGMIRE and QUANDRY are roughly equal. The accuracy of the QUANDRY solution is superior to the QUAGMIRE solution of assembly sized nodes. In addition, QUANDRY runs significantly faster than QUAGMIRE for this problem. This is believed to be primarily due to the additional data requirements of QUAGMIRE.

Table 4-17

Summary of Results for the 3D LRA BWR Static Benchmark Problem

	Coarse Mesh 15x15x25(15) cm	Fine Mesh 7.5x7.5x12.5(7.5) cm	Very Fine Mesh 5x5x12.5(7.5) cm
# unknowns	28996	224400	500676
# outer iterations[a]	22	19	22
Eigenvalue	0.996360	0.996391	0.996381
ε_{max} (node, %)	2.16	0.36	Ref.
$\bar{\varepsilon}$ (node, %)	0.39	0.04	Ref.
ε_{rel} (node, %)	1.62	0.19	Ref.
$\bar{\varepsilon}_{rel}$ (node, %)	0.45	0.04	Ref.
ε_{max} (assembly, %)	1.33	0.24	Ref.
$\bar{\varepsilon}$ (assembly, %)	0.36	0.04	Ref.
ε_{rel} (assembly, %)	1.41	0.18	Ref.
$\bar{\varepsilon}_{rel}$ (assembly, %)	0.37	0.04	Ref.
Execution time (sec SGI 4D/210)	154.72	1132.59	3165.07

[a] Eigenvalue shift = $\lambda + 0.02$, 1 inner/outer iteration, maximum of 32 flux/inner iterations.

Table 4-18

Comparison of Coarse Mesh 3D LRA BWR Static Benchmark Solutions

	QUAGMIRE	QUANDRY [S2]
Physical unknowns	16434	8448
Eigenvalue	0.996360	0.99644
ε_{rel} (node, %)	1.62	0.38
ε_{max} (assembly, %)	1.33	0.32
$\bar{\varepsilon}$ (assembly, %)	0.36	0.09
ε_{rel} (assembly, %)	1.41	0.24
$\bar{\varepsilon}_{rel}$ (assembly, %)	0.37	0.08
Symmetry	1/4 core	1/8 core
Execution time (sec)	154.72[a]	18.7[b]

[a] SGI 4D/210

[b] IBM 370/168

4.4.3 3D LMFBR Static Benchmark Problem

The 3D LMFBR static benchmark problem is a simplified model of the MARK I core design of the SNR 300 prototype LMFBR. It is a rather challenging benchmark because it models the physics of a LMFBR using four energy groups. Unfortunately, because it is a relatively new benchmark and because it requires methods which can solve problems with more than two energy groups this problem has relatively few published solutions. The specifications for this benchmark problem are presented in Section C.5 of Appendix C.

The results of the QUAGMIRE solution to the 3D LMFBR static benchmark problem are presented in Table 4-19. The QUAGMIRE solution used a quartic flux expansion and a quadratic transverse-leakage approximation throughout the reactor. The solution used a 5.4 cm radial mesh spacing, 9.5 cm axial mesh spacing in the core, and a 10.0 cm axial mesh spacing in the axial blankets (19x19x18 meshpoints). Table 4-19 also compares the QUAGMIRE solution to a NEMBOX solution by Finnemann [A4]. The NEMBOX solution also uses a quartic flux expansion and the same spatial discretization. The QUAGMIRE solution is believed to be more accurate because it uses a tighter convergence criterion and should be considered the reference for this benchmark.

Table 4-19

Summary and Comparison of Results for the 3D LMFBR Static Benchmark Problem

	QUAGMIRE	NEMBOX [A4]
# unknowns/group	47450	45486
# outer iterations[a]	17	
Eigenvalue	1.013695	1.013746
Execution time (sec)	1014.65[b]	462[c]

[a] Eigenvalue shift = λ + 1.0, 1 inner/outer iterations, maximum 32 flux/inner iterations.

[b] SGI 4D/210

[c] CDC CYBER 176

4.5 STABILITY CONSIDERATIONS

For three-dimensional problems experience has shown that iterative stability problems may arise if the axial and radial mesh sizes are very different. For both the 3D LRA and 3D LMFBR problems stability problems were encountered if the axial mesh size was greater than three times the radial mesh size, $h_z > 3h_{xy}$. However, if the axial and radial mesh sizes were comparable, $h_z < 3h_{xy}$, no stability problems were experienced.

The cause of the instability was traced to the flux expansions for some of the nodes adjacent to the external reactor boundary. In some of these nodes, at some time during the iteration, the u-directed flux expansion became negative in the region adjacent to the external reactor boundary. The negative face-averaged flux estimate on the external reactor boundary resulted in a change of sign of the u-directed current on the external reactor boundary. The change in sign of the u-directed current on the external reactor boundary resulted in a negative CMFD discontinuity factor, refer to Equations (2-32) and (2-34). Unfortunately, the Aragonés and Ahnert procedure (refer to Section 3.2) is not able to correct for the change in sign of the face-averaged currents on the external reactor boundary and the negative CMFD discontinuity factors induced the instability.

In order to demonstrate this phenomena, the z-directed fast and thermal flux for nodes (1,1,k) of the 3D LRA BWR problem with a 7.5×7.5×25(10) cm mesh for the iteration prior to the instability is shown in Figure 4-9. The z-directed fast flux in the lower axial reflector is shown in Figure 4-10. The fast flux clearly becomes negative in the region adjacent to the external reactor boundary. Figure 4-11 shows the thermal flux in the lower axial reflector. The thermal flux also is negative in the region adjacent to the external reactor boundary. The negative face-averaged fast and thermal fluxes on the reactor boundary results in a positive net-current on the boundary. From Equation (2-32) we see that the positive net-current produces a negative CMFD discontinuity factor.

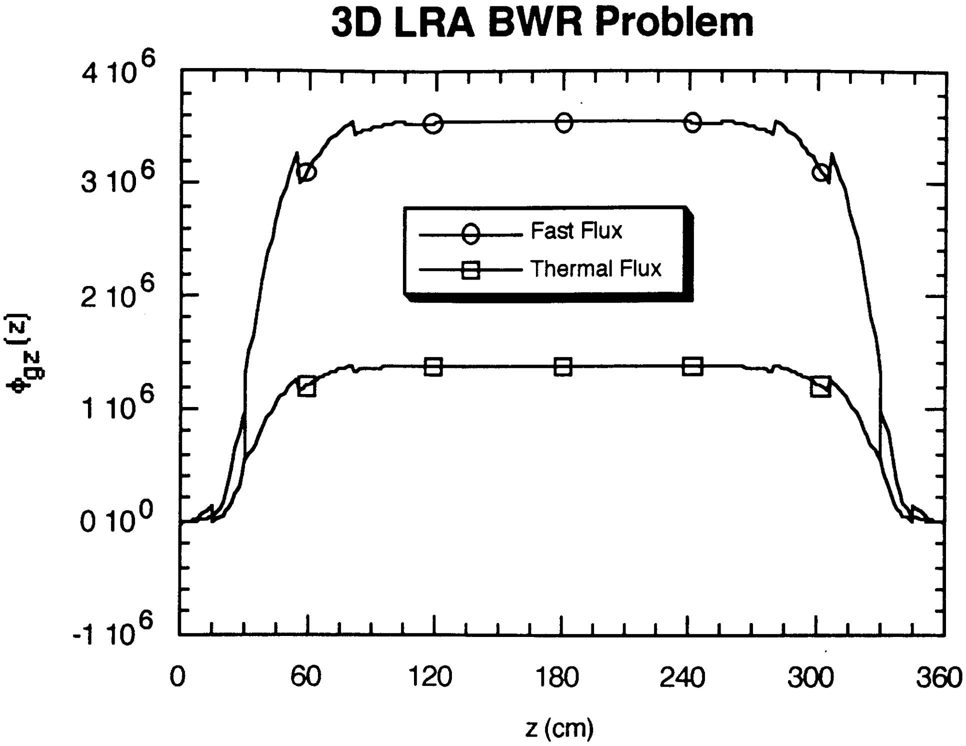

Figure 4-9. 3D LRA BWR Static Benchmark Problem: Z-Directed Fast and Thermal Flux Traverse for Nodes (1,1,k) Prior to Instability, 7.5x7.5x25(10) cm Spatial Mesh.

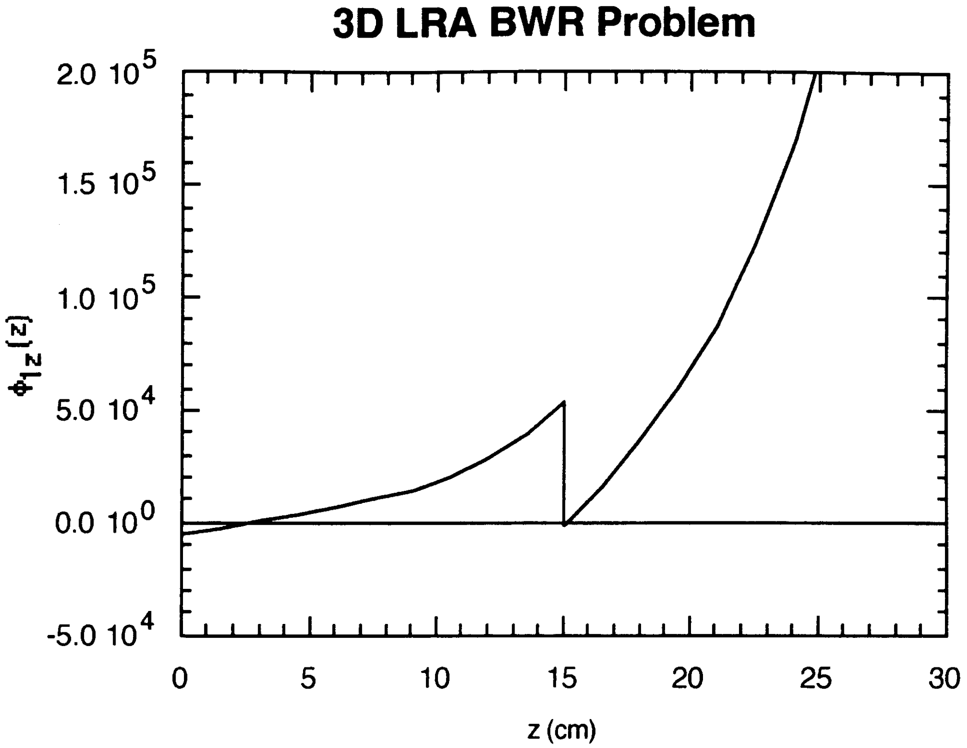

Figure 4-10. 3D LRA BWR Static Benchmark Problem: Z-Directed Fast Flux Traverse in the Lower Axial Reflector for Nodes (1,1,k) Prior to Instability, 7.5×7.5×25(10) cm Spatial Mesh.

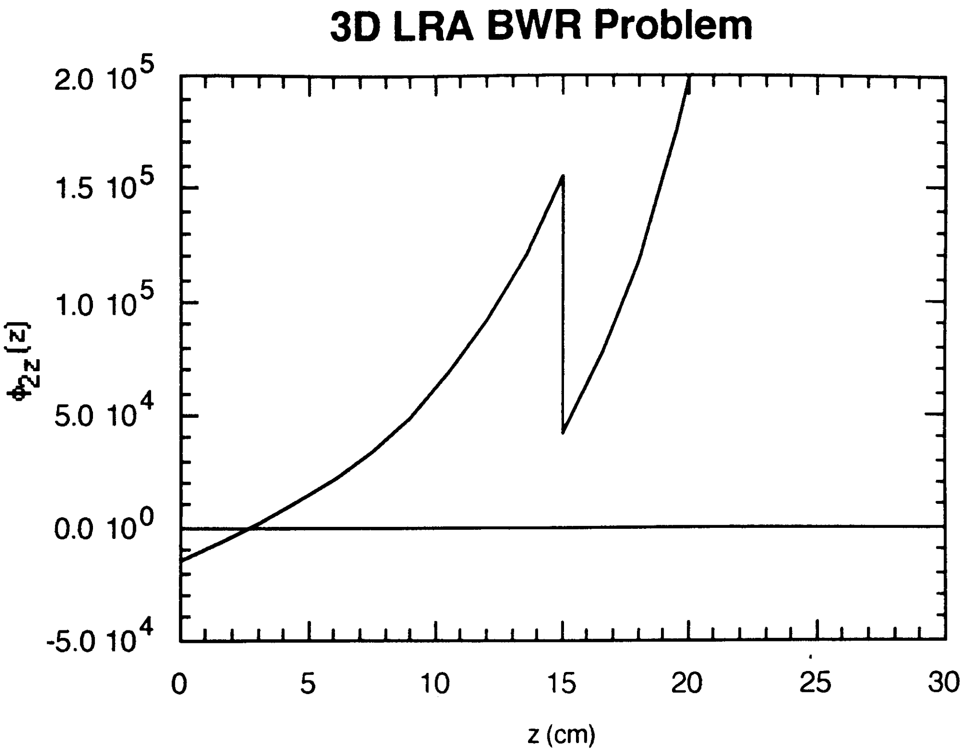

Figure 4-11. 3D LRA BWR Static Benchmark Problem: Z-Directed Thermal Flux Traverse in the Lower Axial Reflector for Nodes (1,1,k) Prior to Instability, 7.5x7.5x25(10) cm Spatial Mesh.

4.6 SUMMARY

In this chapter, the results of several two- and three-dimensional static reactor benchmark problems were presented. The QUAGMIRE polynomial nodal method was shown to be an accurate and efficient method for solving the multidimensional, few-group static neutron diffusion equation, provided that the reactor can be homogenized over large spatial regions (nodes).

The QUAGMIRE Polynomial Nodal Method was shown to require significantly fewer unknowns than finite difference methods to achieve equivalent accuracy. The QUAGMIRE Polynomial Nodal Method was shown to be approximately two orders of magnitude more computationally efficient than finite difference methods. The accuracy of QUAGMIRE was found to be comparable to other nodal methods. However, QUAGMIRE requires more unknowns than the Analytic Nodal Method and the Nodal Expansion Method. The computational efficiency of QUAGMIRE was shown to be slightly lower than the Analytic Nodal Method and the Nodal Expansion Method. The relatively higher numbers of unknown and lower computational efficiency of the QUAGMIRE nodal method compared to other nodal methods is directly related to its increased generality. The QUAGMIRE Polynomial Nodal Method permits more than two energy groups and discontinuities in both the face-averaged fluxes and currents. In order to guarantee stability, three-dimensional problems require similar axial and radial mesh spacings, $h_z < 3h_{xy}$.

CHAPTER 5

SUMMARY

5.1 OVERVIEW OF THE INVESTIGATION

The objective of this thesis was the development of an efficient, general purpose polynomial nodal method for solving the multidimensional, few-group, static neutron diffusion equation. Discontinuities in both the face-averaged flux and net-current were permitted in order to support future research in advanced spatial homogenization methods. The number of energy groups or the structure of the energy groups was not restricted. The nodal method also models the presence of extraneous neutrons sources. Thus, both eigenvalue and source problem may be solved.

A novel nonlinear iteration scheme based on the coarse mesh finite-difference (CMFD) method was developed. The polynomial nodal method is used to determine the inter-nodal coupling and to determine CMFD discontinuity factor ratios. The CMFD discontinuity factor ratios are defined such that they permit the CMFD method to reproduce the solution of the higher-order polynomial nodal method.

In Chapter 2 the CMFD method and the polynomial nodal method both which permit discontinuities in the face-averaged flux and net-current were derived. First the CMFD method was derived. CMFD discontinuity factor ratios which permit the CMFD method to reproduce a reference solution were defined. A polynomial nodal method which permits discontinuities in the face-averaged flux and net-current was derived. Finally, a procedure for determining CMFD discontinuity factor ratios from the polynomial nodal method solution was described.

In Chapter 3 the numerical properties of the nodal method were discussed. A procedure for guaranteeing the stability of the iterative solution was presented. The iterative schemes used to solve eigenvalue and source problems were described. Finally, issues regarding the optimization of the iterative solution were discussed.

In Chapter 4 the QUAGMIRE code was described. QUAGMIRE solutions for several two-dimensional and three-dimensional benchmark problems were presented and compared to other nodal methods and finite-difference methods. The accuracy of the QUAGMIRE code was found to be consistent with other nodal codes. The computational efficiency of QUAGMIRE was found to be slightly less than other nodal methods. For three-dimensional problems it has been found, empirically, that in order to guarantee stability an additional constraint must be placed on the axial mesh size. The axial mesh size must be less than three times the radial mesh size, $h_z < 3h_{xy}$. In practice this constraint will not place an undo restriction on the problems being modelled.

5.2 CONCLUSIONS AND RECOMMENDATIONS

An efficient general purpose polynomial nodal method for solving the multidimensional, few-group, static neutron diffusion equation has been developed. The nodal method is capable of solving problems with any number of energy groups and permits upscattering. The nodal method also models discontinuities in both the face-averaged flux and net-current, permitting the use of advanced spatial homogenization methods. The accuracy of the nodal method was found to be comparable to other nodal methods. The computational efficiency of the nodal method was found to be slightly lower than other nodal methods. The lower computational efficiency is believed to be a consequense the increased generality of the nodal method. The nonlinear iteration scheme was effective in reducing the number of unknowns. For three-dimensional problems the axial mesh size should be comparable to the radial mesh size. Empirically it has been found that the axial mesh size must be less than three time the radial mesh size, $h_z < 3h_{xy}$.

5.2.1 Removing Axial Mesh Restriction

The instability experienced by three-dimensional problems with axial mesh sizes greater than three times the radial mesh size is believed to be due to a nonlinear interaction between the polynomial nodal method and the CMFD method. As discussed in Chapter 3, Aragonés and Ahnert [A1] have shown that the stability of the CMFD method can be guaranteed if the CMFD discontinuity factor ratios are positive. They also have proposed a stability condition which may be used to force the CMFD discontinuity factor ratios to be positive. However, the Aragonés and Ahnert procedure breaks down on the external reactor boundary if the face-averaged flux is negative. Two possible approaches for removing the axial mesh size restriction are proposed.

The first approach is to increase the coupling to the boundary conditions during the third-order and fourth-order expansion coefficient calculation. This may be accomplished by substituting the polynomial nodal coupling equation, Equation (2-67), into Equations (2-60). This will result in two tridiagonal systems of equations for each row, energy group, and direction. This revised expression for the expansion coefficients should have the additional advantage of being more computationally efficient.

Another, more general, approach would be to place an addition constraint on the nodal flux expansions. The flux expansions could formally be required to be positive or equal to zero,

$$\phi_{gu}^{lmn}(u) \geq 0\,, \quad u = x,\, y,\, z.$$

If this constraint were developed it could be applied to all polynomial nodal methods.

5.2.2 Conjugant Gradient Methods

The cyclic Chebyshev semi-iterative (CCSI) method, which is used in the flux iterations, requires an accurate estimate of the spectral radius of the Gauss-Seidel iteration matrix in order to achieve its optimal convergence rate. In nodal methods the spectral radii of the group iteration matrices tends to vary widely as the problem converges. Consequently, most nodal methods tend to use unaccelerated iterations techniques, such as the Gauss-Seidel method, until a coarse eigenvalue convergence criterion has been satisfied. Once the coarse eigenvalue convergence criterion has been satisfied the spectral radii of the Gauss-Seidel iteration matrices are estimated and the CCSI method may be used. The selection of the proper coarse eigenvalue convergence criterion tends to be difficult and, as a result, the overall convergence rate of the flux iterations tends to be significantly lower than the optimal convergence rate. In general this problem will apply to all the iteration methods which use Chebyshev acceleration.

One may achieve significantly higher overall convergence rates by using iterative techniques, for example conjugant gradient method, which do not require estimates of the spectral radii of the iteration matrices. The convergence rate of the conjugant gradient and CCSI methods are equivalent [H1]. The convergence rate of the cyclic conjugant gradient method, a red/black version of the basic conjugant gradient method, is superior to the CCSI method [H1]. The use of conjugant gradient methods is strongly recommended.

5.2.3 Thermal-Hydraulic Feedback

The nodal method should be extended to include thermal-hydraulic feedback. Ideally, the thermal-hydraulic model or models should be general enough to accurately represent the thermal-hydraulic conditions present in light water reactors, gas cooled reactors, and liquid metal cooled reactors. It would also be useful to include a more general model of the dependence of the cross sections and discontinuity factors on thermal-hydraulic parameters.

5.2.4 Time Dependence

The neutronic and thermal-hydraulic models of the nodal method should be extended to permit time dependence. For the neutronic model options should exist for solving time-dependent problems using the frequency transform method and a fully-implicit time differencing method.

5.2.5 Other Coordinate Systems

Finally, a useful enhancement would be the extension of the nodal method to coordinate systems other than Cartesian. Extension to the cylindrical (r-θ-z) and hexagonal-z coordinate systems should be sufficient to model all of the currently proposed reactor designs.

REFERENCES

A1. J. M. Aragonés and Carol Ahnert, "A Linear Discontinuous Finite Difference Formulation for Synthetic Coarse-Mesh Few-Group Diffusion Calculations, *Nuclear Science and Engineering*, **94**, 309–322 (1986).

A2. "Argonne Code Center: Benchmark Problem Book," ANL–7416, Argonne National Laboratory (February 1968).

A3. "Argonne Code Center: Benchmark Problem Book," ANL–7416, Supplement 2, Argonne National Laboratory (June 1977).

A4. "National Energy Software Center: Benchmark Problem Book," ANL–7416, Supplement 3, Argonne National Laboratory (December 1985).

B1. F. Bennewitz, H. Finnemann and H. Moldaschl, "Solution of the Multidimensional Neutron Diffusion Equation by Nodal Expansion," *Proc. ANS Topl. Mtg. Computational Methods in Nuclear Engineering*, Vol. I, 99, Charleston, SC (April 1975).

B2. F. Bennewitz, H. Finnemann and M. R. Wagner, "Higher-Order Corrections in Nodal Reactor Calculations," *Transactions of the American Nuclear Society*, **22**, 250 (1975).

B3. G. P. Bottoni, R. Guandalini, G. Vimercati, and P. Peroni, "Neutronic Aspects of the LWR Core Simulator CETRA," ANS/ENS (May 1979).

B4. G. Buckel, K. Küfner, and B. Stehle, "Benchmark Calculations for a Sodium-Cooled Breeder Reactor by Two- and Three-Dimensional Diffusion Methods," *Nuclear Science and Engineering*, **64**, 75–89 (1977).

B5. G. Buckel et al., *Nuclear Science and Engineering*, **67**, 257 (1978).

C1. W. R. Cadwell, "PDQ-7: A Program for the Solution of the Neutron Diffusion Equations in Two Dimensions," WAPD-TM-678, Bettis Atomic Power Laboratory (1967).

D1. J. J. Dongarra, J. R. Bunch, C. B. Moler, and G. W. Stewart, *LINPACK User's Guide*, SIAM, Philadelphia, PA (1979).

D2. J. J. Dongarra, "Performance of Various Computers Using Standard Linear Equations Software," CS-89-85, University of Tennessee Computer Science Department (December 1991).

F1. H. Finnemann and M. R. Wagner, "The Nodal Expansion Method: A New Computational Technique for the Solution of Multidimensional Neutron Diffusion Problems," *Intl. Spec. Mtg. Methods of Neutron Transport Theory in Reactor Calculations*, Bologna, Italy (November 1975).

F2. H. Finnemann, F. Bennewitz and M. R. Wagner, "Interface Current Techniques for Multidimensional Reactor Calculations," *Atomkernenergie*, **30**, 123 (1977).

F3. H. Finnemann and W. Gundlach, "Space-Time Kinetics Code IQSBOX for PWR and BWR. Part I: Description of Physical and Thermo-Hydraulic Models," *Atomkernenergie Kerntechnik*, **37**, 176–182 (1981).

F4. T. B. Fowler, D. R. Vondy, and G. W. Cunningham, "Nuclear Reactor Analysis Code: CITATION," ORNL-TM-2496, Oak Ridge National Laboratory (1971).

H1. L. A. Hageman and D. M. Young, *Applied Iterative Methods*, Academic Press, San Diego, CA (1981).

H2. A. F. Henry, *Nuclear Reactor Analysis*, MIT Press, Cambridge, MA (1975).

H3. A. F. Henry, "Derivation of Nodal Equations Having the Finite-Difference Form," Course Notes, 22.213, Massachusetts Institute of Technology (Fall 1986).

J1. R. P. Jacqmin, "Implementation of a Fixed-Source Option in the QUANDRY Nodal Code," Internal Report, Massachusetts Institute of Technology, Nuclear Engineering Department (January 1989).

J2. R. P. Jacqmin, personal communication (1989).

K1. M. H. Kim, "The Use of Bilinearly Weighted Cross Sections for Few-Group Transient Analysis," PhD Thesis, Nuclear Engineering Department, Massachusetts Institute of Technology (June 1988).

L1. R. D. Lawrence, "Progress in Nodal Methods for the Solution of the Neutron Diffusion and Transport Equations," *Progress in Nuclear Energy*, **17**, 271–301 (1986).

M1. B. Micheelson and H. Neltrup, "The 3-D IAEA Benchmark Problem," RISO-M-1572 (1973).

S1. R. A. Shober, "A Nodal Method for Solving Transient Few-Group Neutron Diffusion Equations," ANL-78-51, Argonne National Laboratory (June 1978).

S2. K. S. Smith, "An Analytic Nodal Method for Solving the Two-Group, Multidimensional, Static and Transient Neutron Diffusion Equations," NE and SM Thesis, Nuclear Engineering Department, Massachusetts Institute of Technology (March 1979).

S3. K. S. Smith, "Spatial Homogenization Methods for Light Water Reactor Analysis," PhD Thesis, Nuclear Engineering Department, Massachusetts Institute of Technology (June 1980).

S4. K. S. Smith, "Assembly Homogenization Techniques for Light Water Reactors," *Progress in Nuclear Energy*, **17**, 303–335 (1986).

S5. K. S. Smith and K. R. Rempe, "Testing and Applications of the QPANDA Nodal Method," *Nuclear Science and Engineering*, **100**, 324–331 (1988).

S6. K. S. Smith, personal communication (1991).

S7. B. Stehle, "D3D, Ein FORTRAN-Programm zur Loesung der stationaeren dreidimensionalen Multigruppendiffusionsgleichungen," KFK 2118, Kernforschungszentrum Karlsruhe (February 1975).

S8. T. M. Sutton, "Wielandt Iteration as Applied to the Nodal Expansion Method," *Nuclear Science and Engineering*, **98**, 169 (1988).

T1. F. A. Tarantino, "The Development of Cross Sections from Bilinear Variational Theory for use in Few-Group Transient Analysis," PhD Thesis, Nuclear Engineering Department, Massachusetts Institute of Technology (June 1990).

V1. D. R. Vondy, T. B. Fowler, and G. W. Cunningham, "VENTURE: A Code Block for Solving Multigroup Neutronics Problems Applying the Finite-Difference Diffusion-Theory Approximation to Neutron Transport," ORNL-5062, Oak Ridge National Laboratory (1975).

W1. E. L. Wachspress, *Iterative Solution to Elliptic Systems*, Prentice-Hall, Englewood, NJ (1966).

W2. M. R. Wagner, H. Finnemann, K. Koebke, and H. J. Winter, "Validation of the Nodal Expansion Method and the Depletion Program MEDIUM–2 by Benchmark Calculations and Direct Comparison with Experiment," *Atomkernenergy*, **30**, 129 (1977).

APPENDIX A

DERIVATION OF THE FLUX AND CURRENT MOMENTS

In this Appendix the flux and current moment are derived. The flux and current moments are required by the weighted residual procedure used to determine the higher-order ($N \geq 3$) flux expansion coefficients. The transverse-integrated flux is expanded as a low order polynomial. For a fourth-order polynomial ($N = 4$) the flux expansion for node (lmn) is

$$\begin{aligned}\phi_{gu}^{lmn}(u) = \phi_{gu}^{lmn}(u_l^+)\left[3\xi^2 - 4\xi + 1\right] + \phi_{gu}^{lmn}(u_{l+1}^-)\left[3\xi^2 - 2\xi\right] + \bar{\phi}_g^{lmn}\left[6\xi - 6\xi^2\right] \\ + a_{gu3}^{lmn}\left[-\xi^3 + \frac{3}{2}\xi^2 - \frac{1}{2}\xi\right] + a_{gu4}^{lmn}\left[-\xi^4 + 2\xi^3 - \frac{6}{5}\xi^2 + \frac{1}{5}\xi\right],\end{aligned} \tag{A-1}$$

where,

$$\xi \equiv \frac{u - u_l}{h_u^l}.$$

Before we begin the derivation of the flux and current moments, the definition of the following identities will prove to be useful:

$$\begin{aligned}
\int_0^1 \left(\xi - \frac{1}{2}\right) d\xi &= 0 \\
\int_0^1 \left(\xi - \frac{1}{2}\right) \xi \, d\xi &= \frac{1}{12} \\
\int_0^1 \left(\xi - \frac{1}{2}\right) \xi^2 d\xi &= \frac{1}{12} \\
\int_0^1 \left(\xi - \frac{1}{2}\right) \xi^3 d\xi &= \frac{3}{40} \\
\int_0^1 \left(\xi - \frac{1}{2}\right) \xi^4 d\xi &= \frac{1}{15}
\end{aligned}$$

$$\begin{aligned}
\int_0^1 \left(3\xi^2 - 3\xi + \frac{1}{2}\right) d\xi &= 0 \\
\int_0^1 \left(3\xi^2 - 3\xi + \frac{1}{2}\right) \xi \, d\xi &= 0 \\
\int_0^1 \left(3\xi^2 - 3\xi + \frac{1}{2}\right) \xi^2 d\xi &= \frac{1}{60} \\
\int_0^1 \left(3\xi^2 - 3\xi + \frac{1}{2}\right) \xi^3 d\xi &= \frac{1}{40} \\
\int_0^1 \left(3\xi^2 - 3\xi + \frac{1}{2}\right) \xi^4 d\xi &= \frac{1}{35}
\end{aligned}$$

The flux moments are defined by

$$\left\langle w_n(u),\, \phi_{gu}^{lmn}(u) \right\rangle \equiv \frac{1}{h_u^l} \int_{u_l^+}^{u_{l+1}^-} w_n(u)\, \phi_{gu}^{lmn}(u)\, du$$

$$\equiv \int_0^1 w_n(\xi)\, \phi_{gu}^{lmn}(\xi)\, d\xi \qquad \text{(A-2)}$$

$$\equiv \phi_{gun}^{lmn} \ ,$$

where $w_n(u)$ this the weighting function. For the first flux moment, the weighting function is set equal to the first-order basis function, $w_1(u) = f_1(u) = \xi - \frac{1}{2}$. The first flux moment is obtained by substituting Equation (A-1) into Equation (A-2),

$$\phi_{gu1}^{lmn} = \phi_{gu}^{lmn}(u_l^+) \int_0^1 \left(\xi - \frac{1}{2}\right)\left(3\xi^2 - 4\xi + 1\right) d\xi$$

$$+ \phi_{gu}^{lmn}(u_{l+1}^-) \int_0^1 \left(\xi - \frac{1}{2}\right)\left(3\xi^2 - 2\xi\right) d\xi$$

$$+ \bar{\phi}_g^{lmn} \int_0^1 \left(\xi - \frac{1}{2}\right)\left(6\xi - 6\xi^2\right) d\xi$$

$$+ a_{gu3}^{lmn} \int_0^1 \left(\xi - \frac{1}{2}\right)\left(-\xi^3 + \frac{3}{2}\xi^2 - \frac{1}{2}\xi\right) d\xi$$

$$+ a_{gu4}^{lmn} \int_0^1 \left(\xi - \frac{1}{2}\right)\left(-\xi^4 + 2\xi^3 - \frac{6}{5}\xi^2 + \frac{1}{5}\xi\right) d\xi \ ,$$

and after some algebra we get

$$\phi_{gu1}^{lmn} = \frac{1}{12}\phi_{gu}^{lmn}(u_{l+1}^-) - \frac{1}{12}\phi_{gu}^{lmn}(u_l^+) + \frac{1}{120} a_{gu3}^{lmn} \ . \qquad \text{(A-3)}$$

An equivalent expression for the first flux moment in terms of the first-order and third-order expansion coefficients may be obtained by substituting Equation (2-40b) into Equation (A-3),

$$\phi_{gu1}^{lmn} = \frac{1}{12} a_{gu1}^{lmn} + \frac{1}{120} a_{gu3}^{lmn} \ . \tag{A-4}$$

Similarly, for the second flux moment the weighting function equal to the second-order basis function, $w_2(u) = f_2(u) = 3\xi^2 - 3\xi + \frac{1}{2}$. The second flux moment is obtained by substituting Equation (A-1) into Equation (A-2),

$$\begin{aligned}
\phi_{gu2}^{lmn} = \ & \phi_{gu}^{lmn}(u_l^+) \int_0^1 \left(3\xi^2 - 3\xi + \frac{1}{2}\right)\left(3\xi^2 - 4\xi + 1\right) d\xi \\
& + \phi_{gu}^{lmn}(u_{l+1}^-) \int_0^1 \left(3\xi^2 - 3\xi + \frac{1}{2}\right)\left(3\xi^2 - 2\xi\right) d\xi \\
& + \bar{\phi}_g^{lmn} \int_0^1 \left(3\xi^2 - 3\xi + \frac{1}{2}\right)\left(6\xi - 6\xi^2\right) d\xi \\
& + a_{gu3}^{lmn} \int_0^1 \left(3\xi^2 - 3\xi + \frac{1}{2}\right)\left(-\xi^3 + \frac{3}{2}\xi^2 - \frac{1}{2}\xi\right) d\xi \\
& + a_{gu4}^{lmn} \int_0^1 \left(3\xi^2 - 3\xi + \frac{1}{2}\right)\left(-\xi^4 + 2\xi^3 - \frac{6}{5}\xi^2 + \frac{1}{5}\xi\right) d\xi \ ,
\end{aligned}$$

and after some algebra we get

$$\phi_{gu2}^{lmn} = \frac{1}{20}\phi_{gu}^{lmn}(u_l^+) + \frac{1}{20}\phi_{gu}^{lmn}(u_{l+1}^-) - \frac{1}{10}\bar{\phi}_g^{lmn} + \frac{1}{700} a_{gu3}^{lmn} \ . \tag{A-5}$$

The equivalent expression for the second flux moment in terms of the second-order and fourth-order expansion coefficients may be obtained by substituting Equation (2-40c) into Equation (A-5),

$$\phi_{gu2}^{lmn} = \frac{1}{20} a_{gu2}^{lmn} + \frac{1}{700} a_{gu4}^{lmn} \ . \tag{A-6}$$

The current moments are defined by

$$\left\langle w_n(u), \frac{d}{du}J_{gu}^{lmn}(u)\right\rangle \equiv \frac{1}{h_u^l}\int_{u_l^+}^{u_{l+1}^-} w_n(u)\,\frac{d}{du}J_{gu}^{lmn}(u)\,du\,. \tag{A-7}$$

The first current moment is obtained by setting the weighting function equal to the first-order basis function and then integrating Equation (A-7) by parts,

$$\begin{aligned}
\left\langle w_1(u), \frac{d}{du}J_{gu}^{lmn}(u)\right\rangle &= \frac{1}{h_u^l}\int_{u_l^+}^{u_{l+1}^-}\left(\xi - \frac{1}{2}\right)\frac{d}{du}J_{gu}^{lmn}(u)\,du \\
&= \frac{1}{h_u^l}J_{gu}^{lmn}(u)\left[\frac{u - u_l^+}{h_u^l} - \frac{1}{2}\right]\Bigg|_{u_l^+}^{u_{l+1}^-} - \frac{1}{(h_u^l)^2}\int_{u_l^+}^{u_{l+1}^-} J_{gu}^{lmn}(u)\,du \\
&= \frac{1}{2h_u^l}\left[J_{gu}^{lmn}(u_{l+1}^-) + J_{gu}^{lmn}(u_l^+)\right] + \frac{D_g^{lmn}}{(h_u^l)^2}\int_{u_l^+}^{u_{l+1}^-}\frac{d}{du}\phi_{gu}^{lmn}(u)\,du \\
&= \frac{1}{2h_u^l}\left[J_{gu}^{lmn}(u_{l+1}^-) + J_{gu}^{lmn}(u_l^+)\right] + \frac{D_g^{lmn}}{(h_u^l)^2}\left[\phi_{gu}^{lmn}(u_{l+1}^-) - \phi_{gu}^{lmn}(u_l^+)\right]
\end{aligned} \tag{A-8}$$

Substituting Equation (2-40b) into Equation (A-8) yields an alternate expression for the first current moment

$$\left\langle w_1(u), \frac{d}{du}J_{gu}^{lmn}(u)\right\rangle = \frac{1}{2h_u^l}\left[J_{gu}^{lmn}(u_{l+1}^-) + J_{gu}^{lmn}(u_l^+)\right] + \frac{D_g^{lmn}}{(h_u^l)^2}a_{gul}^{lmn}\,. \tag{A-9}$$

The second current moment is obtained by setting the weighting function equal to the second-order basis function and integrating Equation (A-7) by parts twice,

$$\begin{aligned}\left\langle w_2(u), \frac{d}{du}J_{gu}^{lmn}(u)\right\rangle &= \frac{1}{h_u^l}\int_{u_l^+}^{u_{l+1}^-}\left(3\xi^2 - 3\xi + \frac{1}{2}\right)\frac{d}{du}J_{gu}^{lmn}(u)\,du \\ &= \frac{1}{h_u^l}J_{gu}^{lmn}(u)\left[3\xi^2 - 3\xi + \frac{1}{2}\right]\Bigg|_{u_l^+}^{u_{l+1}^-} - \frac{1}{\left(h_u^l\right)^2}\int_{u_l^+}^{u_{l+1}^-}\left(6\xi - 3\right)J_{gu}^{lmn}(u)\,du \\ &= \frac{1}{2h_u^l}\left[J_{gu}^{lmn}(u_{l+1}^-) - J_{gu}^{lmn}(u_l^+)\right] + \frac{6D_g^{lmn}}{\left(h_u^l\right)^2}\int_{u_l^+}^{u_{l+1}^-}\left(\xi - \frac{1}{2}\right)\frac{d}{du}\phi_{gu}^{lmn}(u)\,du \\ &= \frac{1}{2h_u^l}\left[J_{gu}^{lmn}(u_{l+1}^-) + J_{gu}^{lmn}(u_l^+)\right] + \frac{3D_g^{lmn}}{\left(h_u^l\right)^2}\left[\phi_{gu}^{lmn}(u_{l+1}^-) + \phi_{gu}^{lmn}(u_l^+) - 2\overline{\phi}_g^{lmn}\right].\end{aligned} \tag{A-10}$$

Substituting Equation (2-40c) into Equation (A-10) yields an alternate equation for the second current moment,

$$\left\langle w_2(u), \frac{d}{du}J_{gu}^{lmn}(u)\right\rangle = \frac{1}{2h_u^l}\left[J_{gu}^{lmn}(u_{l+1}^-) - J_{gu}^{lmn}(u_l^+)\right] + \frac{3D_g^{lmn}}{\left(h_u^l\right)^2}a_{gu2}^{lmn} \; . \tag{A-11}$$

APPENDIX B

DERIVATION OF TRANSVERSE-LEAKAGE MOMENTS

In this Appendix the transverse-leakage moments will be derived. The u-directed transverse-leakage moment for node (lmn) is defined as

$$S_{gun}^{lmn} \equiv \frac{1}{h_u^l} \int_{u_l^+}^{u_{l+1}^-} w_n(u)\, S_{gu}^{lmn}(u)\, du\ , \tag{B-1}$$

where $w_n(u)$ is the weight function. The weight functions we will consider are the first-order and second-order basis functions:

$$w_1(u) = \xi - \frac{1}{2} \tag{B-2a}$$

$$w_2(u) = 3\xi^2\ 3\xi + \frac{1}{2}\quad . \tag{B-2b}$$

where,

$$\xi = \frac{u - u_l}{h_u^l}.$$

Several approximations of the shape of the u-directed transverse-leakage within a node will be considered. These approximations are:

1. Quadratic Transverse-Leakage Approximation,
2. LHS-Biased Quadratic Transverse-Leakage Approximation,
3. RHS-Biased Quadratic Transverse-Leakage Approximation,
4. Flat Transverse-Leakage Approximation.

In the quadratic transverse-leakage approximation the shape of the u-directed transverse-leakage in three adjacent nodes is fit to a quadratic polynomial centered on the node in the middle. In addition, the quadratic fit is required to preserve the average transverse-leakages in each of the three adjacent nodes. The quadratic transverse-leakage approximation may be used for any node in the interior of the reactor. However, for nodes adjacent to the external reactor boundary there is insufficient information to determine a quadratic fit for the central node. In this case a biased quadratic fit may be used. Finally, the crudest approximation that may be made regarding the shape of the transverse-leakage is that it is flat. Typically, the flat transverse-leakage approximation is used in nodes adjacent to the external reactor boundary.

B.1 QUADRATIC TRANSVERSE-LEAKAGE APPROXIMATION

In the Quadratic Transverse-Leakage Approximation we approximate the u-directed transverse-leakage in node (lmn) using the following a quadratic function,

$$\begin{aligned} S_{gu}^{lmn}(u) &\cong \overline{S}_{gu}^{lmn} + \left(\overline{S}_{gu}^{l-1,mn} - \overline{S}_{gu}^{lmn}\right)\rho_{u_l}^{l-1}(u) + \left(\overline{S}_{gu}^{l+1,mn} - \overline{S}_{gu}^{lmn}\right)\rho_{u_l}^{l+1}(u) \\ &= \overline{S}_{gu}^{lmn} + \overline{\Delta S}_{gu-}^{lmn}\,\rho_{u_l}^{l-1}(u) + \overline{\Delta S}_{gu+}^{lmn}\,\rho_{u_l}^{l+1}(u)\ , \end{aligned} \tag{B-3}$$

where

$\overline{S}_{gu}^{lmn} h_u^l h_v^m h_w^m$ ≡ average net-rate at which neutrons leave node (lmn) through the faces transverse to direction u,

and

$$\rho_{u_l}^{l-1}(u) = a_{u_l}^- + b_{u_l}^- \xi + c_{u_l}^- \xi^2\ , \tag{B-4a}$$

$$\rho_{u_l}^{l+1}(u) = a_{u_l}^+ + b_{u_l}^+ \xi + c_{u_l}^+ \xi^2\ . \tag{B-4b}$$

In addition, we require the quadratic transverse-leakage expansion, Equation (B-3), to preserve the average transverse-leakages in each of the three adjacent nodes. Thus, we require the following constrains on Equations (B-4a) and (B-4b):

$$\begin{aligned}
\frac{1}{h_u^{l-1}}\int_{u_{l-1}^+}^{u_l^-} \rho_{u_l}^{l-1}(u)\,du &= 1\,, \\
\frac{1}{h_u^{l}}\int_{u_{l}^+}^{u_{l+1}^-} \rho_{u_l}^{l-1}(u)\,du &= 0\,, \\
\frac{1}{h_u^{l+1}}\int_{u_{l+1}^+}^{u_{l+2}^-} \rho_{u_l}^{l-1}(u)\,du &= 0\,,
\end{aligned} \tag{B-5a}$$

$$\begin{aligned}
\frac{1}{h_u^{l-1}}\int_{u_{l-1}^+}^{u_l^-} \rho_{u_l}^{l+1}(u)\,du &= 0\,, \\
\frac{1}{h_u^{l}}\int_{u_{l}^+}^{u_{l+1}^-} \rho_{u_l}^{l+1}(u)\,du &= 0\,, \\
\frac{1}{h_u^{l+1}}\int_{u_{l+1}^+}^{u_{l+2}^-} \rho_{u_l}^{l+1}(u)\,du &= 1\,.
\end{aligned} \tag{B-5b}$$

Integrating Equation (B-3) over the three adjacent nodes and applying the constraints, Equations (B-5a) and (B-5b), yields the coefficients of the transverse-leakage expansion:

$$\begin{aligned}
a_{u_l}^- &= \frac{h(h+h_p)}{(h_m+h+h_p)(h_m+h)} \\
b_{u_l}^- &= -\frac{2h(2h+h_p)}{(h_m+h+h_p)(h_m+h)} \\
c_{u_l}^- &= \frac{3h^2}{(h_m+h+h_p)(h_m+h)} \\
a_{u_l}^+ &= -\frac{h\,h_m}{(h_m+h+h_p)(h+h_p)} \\
b_{u_l}^+ &= \frac{2h(h_m-h)}{(h_m+h+h_p)(h+h_p)} \\
c_{u_l}^+ &= \frac{3h^2}{(h_m+h+h_p)(h+h_p)}
\end{aligned} \tag{B-6}$$

where

$$h_m = h_u^{l-1}$$
$$h = h_u^{l}$$
$$h_p = h_u^{l+1} .$$

Note that the transverse-leakage expansion coefficients are functions of only the reactor geometry. For equal-sized nodes, $h_m = h_p = h$, the expansion coefficients are:

$$a_{u_l}^{-} = \frac{1}{3}, \qquad a_{u_l}^{+} = -\frac{1}{6},$$
$$b_{u_l}^{-} = -1, \qquad b_{u_l}^{+} = 0,$$
$$c_{u_l}^{-} = \frac{1}{2}, \qquad c_{u_l}^{+} = \frac{1}{2}.$$

An equivalent, and more convenient, expression for the quadratic transverse-leakage expansion may be obtained by rearranging Equation (B-3) to isolate the flat, linear, and quadratic term

$$S_{gu}^{lmn}(u) = \overline{S}_{gu,f}^{lmn} + \overline{S}_{gu,l}^{lmn}\xi + \overline{S}_{gu,q}^{lmn}\xi^2 , \tag{B-7}$$

where

$$\overline{S}_{gu,f}^{lmn} = \overline{S}_{gu}^{lmn} + a_{u_l}^{-}\overline{\Delta S}_{gu-}^{lmn} + a_{u_l}^{+}\overline{\Delta S}_{gu+}^{lmn} ,$$
$$\overline{S}_{gu,l}^{lmn} = b_{u_l}^{-}\overline{\Delta S}_{gu-}^{lmn} + b_{u_l}^{+}\overline{\Delta S}_{gu+}^{lmn} ,$$
$$\overline{S}_{gu,q}^{lmn} = c_{u_l}^{-}\overline{\Delta S}_{gu-}^{lmn} + c_{u_l}^{+}\overline{\Delta S}_{gu+}^{lmn} .$$

The transverse-leakage moments are then obtained by substituting Equation (B-7) into Equation (B-1),

$$S_{gun}^{lmn} = \int_0^1 w_n(\xi)\left[\overline{S}_{gu,f}^{lmn} + \overline{S}_{gu,l}^{lmn}\xi + \overline{S}_{gu,q}^{lmn}\xi^2\right]d\xi . \tag{B-8}$$

After some algebra and applying the identities given in Appendix A, the first and second transverse-leakage moments are obtained

$$S_{gu1}^{lmn} = \frac{1}{12}\left(\overline{S}_{gu,l}^{lmn} + \overline{S}_{gu,q}^{lmn}\right) , \tag{B-9}$$

$$S_{gu2}^{lmn} = \frac{1}{60}\overline{S}_{gu,q}^{lmn} . \tag{B-10}$$

Expanding the linear and quadratic terms yield the first and second transverse-leakage moments for the quadratic transverse-leakage approximation

$$S_{gu1}^{lmn} = \frac{1}{12}\left[\left(b_{u_l}^{-} + c_{u_l}^{-}\right)\overline{S}_{gu}^{l-1,mn} - \left(b_{u_l}^{-} + c_{u_l}^{-} + b_{u_l}^{+} + c_{u_l}^{+}\right)\overline{S}_{gu}^{lmn} + \left(b_{u_l}^{+} + c_{u_l}^{+}\right)\overline{S}_{gu}^{l+1,mn}\right] \quad \text{(B-11)}$$

$$S_{gu2}^{lmn} = \frac{1}{60}\left[c_{u_l}^{-}\overline{S}_{gu}^{l-1,mn} - \left(c_{u_l}^{-} + c_{u_l}^{+}\right)\overline{S}_{gu}^{lmn} + c_{u_l}^{+}\overline{S}_{gu}^{l+1,mn}\right]. \quad \text{(B-12)}$$

B.2 LHS-BIASED QUADRATIC TRANSVERSE-LEAKAGE APPROXIMATION

For nodes adjacent to the LHS external reactor boundary, we may approximate the u-directed transverse-leakage in node (lmn) using the following biased quadratic function,

$$\begin{aligned} S_{gu}^{lmn}(u) &\cong \overline{S}_{gu}^{lmn} + \left(\overline{S}_{gu}^{l+1,mn} - \overline{S}_{gu}^{lmn}\right)\rho_{u_l}^{l+1}(u) + \left(\overline{S}_{gu}^{l+2,mn} - \overline{S}_{gu}^{lmn}\right)\rho_{u_l}^{l+2}(u) \\ &= \overline{S}_{gu}^{lmn} + \overline{\Delta S}_{gu+}^{lmn}\rho_{u_l}^{l+1}(u) + \overline{\Delta S}_{gu++}^{lmn}\rho_{u_l}^{l+2}(u)\ , \end{aligned} \quad \text{(B-13)}$$

where

$$\rho_{u_l}^{l+1}(u) = a_{u_l}^{+} + b_{u_l}^{+}\left(\frac{u - u_l}{h_u^l}\right) + c_{u_l}^{+}\left(\frac{u - u_l}{h_u^l}\right)^2 , \quad \text{(B-14a)}$$

$$\rho_{u_l}^{l+2}(u) = a_{u_l}^{++} + b_{u_l}^{++}\left(\frac{u - u_l}{h_u^l}\right) + c_{u_l}^{++}\left(\frac{u - u_l}{h_u^l}\right)^2 , \quad \text{(B-14b)}$$

Rearranging Equation (B-13) and combining its flat, linear, and quadratic terms yield an alternate expression for the LHS-biased transverse-leakage expansion

$$S_{gu}^{lmn}(u) = \overline{S}_{gu,f}^{lmn} + \overline{S}_{gu,l}^{lmn}\left(\frac{u - u_l}{h_u^l}\right) + \overline{S}_{gu,q}^{lmn}\left(\frac{u - u_l}{h_u^l}\right)^2 \quad \text{(B-15)}$$

where

$$\begin{aligned} \overline{S}_{gu,f}^{lmn} &= \overline{S}_{gu}^{lmn} + a_{u_l}^{+}\overline{\Delta S}_{gu+}^{lmn} + a_{u_l}^{++}\overline{\Delta S}_{gu++}^{lmn}\ , \\ \overline{S}_{gu,l}^{lmn} &= b_{u_l}^{+}\overline{\Delta S}_{gu+}^{lmn} + b_{u_l}^{++}\overline{\Delta S}_{gu++}^{lmn}\ , \\ \overline{S}_{gu,q}^{lmn} &= c_{u_l}^{+}\overline{\Delta S}_{gu+}^{lmn} + c_{u_l}^{++}\overline{\Delta S}_{gu++}^{lmn}\ . \end{aligned}$$

In addition, we require the LHS-biased quadratic transverse-leakage expansion to preserve the average transverse-leakages in nodes (lmn), (l+1,mn), and (l+2,mn). Therefore, we place the following constraints on Equations (B-14a) and (B-14b):

$$
\begin{aligned}
\frac{1}{h_u^l}\int_{u_l^+}^{u_{l+1}^-} \rho_{u_l}^{l+1}(u)\,du &= 0 &\qquad \frac{1}{h_u^l}\int_{u_l^+}^{u_{l+1}^-} \rho_{u_l}^{l+2}(u)\,du &= 0 \\
\frac{1}{h_u^{l+1}}\int_{u_{l+1}^+}^{u_{l+2}^-} \rho_{u_l}^{l+1}(u)\,du &= 1 &\qquad \frac{1}{h_u^{l+1}}\int_{u_{l+1}^+}^{u_{l+2}^-} \rho_{u_l}^{l+2}(u)\,du &= 0 \\
\frac{1}{h_u^{l+2}}\int_{u_{l+2}^+}^{u_{l+3}^-} \rho_{u_l}^{l+1}(u)\,du &= 0 &\qquad \frac{1}{h_u^{l+2}}\int_{u_{l+2}^+}^{u_{l+3}^-} \rho_{u_l}^{l+2}(u)\,du &= 1\,.
\end{aligned}
$$

The expansion coefficients are obtained by integrating Equation (B-15) over h_u^l, h_u^{l+1}, and h_u^{l+2} and applying the above constraints. The coefficients for the LHS-biased quadratic transverse-leakage expansion are:

$$
\begin{aligned}
a_{u_l}^{+} &= -\frac{h\left[h(h+4h_p+2h_{pp})+3h_p(h_p+h_{pp})+h_{pp}^2\right]}{(h+h_p)(h_p+h_{pp})(h+h_p+h_{pp})} \\
b_{u_l}^{+} &= \frac{2h\left[h(2h+6h_p+3h_{pp})+3h_p(h_p+h_{pp})+h_{pp}^2\right]}{(h+h_p)(h_p+h_{pp})(h+h_p+h_{pp})} \\
c_{u_l}^{+} &= -\frac{3h^2(h+2h_p+h_{pp})}{(h+h_p)(h_p+h_{pp})(h+h_p+h_{pp})} \\
a_{u_l}^{++} &= \frac{h(h+h_p)}{(h_p+h_{pp})(h+h_p+h_{pp})} \\
b_{u_l}^{++} &= -\frac{2h(2h+h_p)}{(h_p+h_{pp})(h+h_p+h_{pp})} \\
c_{u_l}^{++} &= \frac{3h^2}{(h_p+h_{pp})(h+h_p+h_{pp})}
\end{aligned}
\qquad \text{(B-16)}
$$

where

$$
\begin{aligned}
h &= h_u^l \\
h_p &= h_u^{l+1} \\
h_{pp} &= h_u^{l+2}\,.
\end{aligned}
$$

For equal sized nodes, $h = h_p = h_{pp}$, the expansion coefficients are:

$$a^{+}_{u_l} = -\frac{7}{6}, \qquad a^{++}_{u_l} = \frac{1}{3},$$

$$b^{+}_{u_l} = 3, \qquad b^{++}_{u_l} = -1,$$

$$c^{+}_{u_l} = -1, \qquad c^{++}_{u_l} = \frac{1}{2}.$$

Substituting Equation (B-15) into Equation (B-1) and solving the resulting equations yields the first and second transverse-leakage moments for the LHS-biased transverse-leakage approximation

$$S^{lmn}_{gu1} = \frac{1}{12}\left[\left(b^{+}_{u_l} + c^{+}_{u_l}\right)\overline{S}^{l+1,mn}_{gu} - \left(b^{+}_{u_l} + c^{+}_{u_l} + b^{++}_{u_l} + c^{++}_{u_l}\right)\overline{S}^{lmn}_{gu} + \left(b^{++}_{u_l} + c^{++}_{u_l}\right)\overline{S}^{l+2,mn}_{gu}\right] \tag{B-17}$$

$$S^{lmn}_{gu2} = \frac{1}{60}\left[c^{+}_{u_l}\overline{S}^{l+1,mn}_{gu} - \left(c^{+}_{u_l} + c^{++}_{u_l}\right)\overline{S}^{lmn}_{gu} + c^{++}_{u_l}\overline{S}^{l+2,mn}_{gu}\right]. \tag{B-18}$$

B.3 RHS-BIASED QUADRATIC TRANSVERSE-LEAKAGE APPROXIMATION

Similarly, for nodes adjacent to the RHS external reactor boundary, we may approximate the u-directed transverse-leakage in node (lmn) using the following biased quadratic function,

$$\begin{aligned} S^{lmn}_{gu}(u) &\cong \overline{S}^{lmn}_{gu} + \left(\overline{S}^{l-1,mn}_{gu} - \overline{S}^{lmn}_{gu}\right)\rho^{l-1}_{u_l}(u) + \left(\overline{S}^{l-2,mn}_{gu} - \overline{S}^{lmn}_{gu}\right)\rho^{l-2}_{u_l}(u) \\ &= \overline{S}^{lmn}_{gu} + \overline{\Delta S}^{lmn}_{gu-}\,\rho^{l-1}_{u_l}(u) + \overline{\Delta S}^{lmn}_{gu--}\,\rho^{l-2}_{u_l}(u)\ , \end{aligned} \tag{B-19}$$

where

$$\rho^{l-1}_{u_l}(u) = a^{-}_{u_l} + b^{-}_{u_l}\left(\frac{u - u_l}{h^l_u}\right) + c^{-}_{u_l}\left(\frac{u - u_l}{h^l_u}\right)^2 , \tag{B-20a}$$

$$\rho^{l-2}_{u_l}(u) = a^{--}_{u_l} + b^{--}_{u_l}\left(\frac{u - u_l}{h^l_u}\right) + c^{--}_{u_l}\left(\frac{u - u_l}{h^l_u}\right)^2 . \tag{B-20b}$$

Rearranging Equation (B-19) and combining its flat, linear, and quadratic terms yield an alternate expression for the LHS-biased transverse-leakage expansion

$$S^{lmn}_{gu}(u) = \overline{S}^{lmn}_{gu,f} + \overline{S}^{lmn}_{gu,l}\left(\frac{u - u_l}{h^l_u}\right) + \overline{S}^{lmn}_{gu,q}\left(\frac{u - u_l}{h^l_u}\right)^2 \tag{B-21}$$

where

$$\overline{S}^{lmn}_{gu,f} = \overline{S}^{lmn}_{gu} + a_{u_l^-}\overline{\Delta S}^{lmn}_{gu-} + a_{u_l^{--}}\overline{\Delta S}^{lmn}_{gu--} ,$$

$$\overline{S}^{lmn}_{gu,l} = b_{u_l^-}\overline{\Delta S}^{lmn}_{gu-} + b_{u_l^{--}}\overline{\Delta S}^{lmn}_{gu--} ,$$

$$\overline{S}^{lmn}_{gu,q} = c_{u_l^-}\overline{\Delta S}^{lmn}_{gu-} + c_{u_l^{--}}\overline{\Delta S}^{lmn}_{gu--} .$$

In addition, we require the RHS-biased quadratic transverse-leakage expansion to preserve the average transverse-leakages in nodes (lmn), (l-1,mn), and (l-2,mn). Therefore, we place the following constraints on Equations (B-20a) and (B-20b):

$$\frac{1}{h_u^l}\int_{u_l^+}^{u_{l+1}^-} \rho_{u_l}^{l-1}(u)\,du = 0 \qquad \frac{1}{h_u^l}\int_{u_l^+}^{u_{l+1}^-} \rho_{u_l}^{l-2}(u)\,du = 0$$

$$\frac{1}{h_u^{l-1}}\int_{u_{l-1}^+}^{u_l^-} \rho_{u_l}^{l-1}(u)\,du = 1 \qquad \frac{1}{h_u^{l-1}}\int_{u_{l-1}^+}^{u_l^-} \rho_{u_l}^{l-2}(u)\,du = 0$$

$$\frac{1}{h_u^{l-2}}\int_{u_{l-2}^+}^{u_{l-1}^-} \rho_{u_l}^{l-1}(u)\,du = 0 \qquad \frac{1}{h_u^{l-2}}\int_{u_{l+2}^+}^{u_{l-1}^-} \rho_{u_l}^{l-2}(u)\,du = 1 .$$

The expansion coefficients are obtained by integrating Equation (B-21) over h_u^l, h_u^{l-1}, and h_u^{l-2} and applying the above constraints. The coefficients for the RHS-biased quadratic transverse-leakage expansion are:

$$\begin{aligned}
a_{u_l^-} &= \frac{h[h_{mm}(h_{mm} + 3h_m + h) + h_m(3h_m + 2h)]}{(h_m + h)(h_{mm} + h_m)(h_{mm} + h_m + h)} \\
b_{u_l^-} &= -\frac{2h[h_{mm}(h_{mm} + 3h_m) + 3h_m^2 - h^2]}{(h_m + h)(h_{mm} + h_m)(h_{mm} + h_m + h)} \\
c_{u_l^-} &= -\frac{3h^2(h_{mm} + 2h_m + h)}{(h_m + h)(h_{mm} + h_m)(h_{mm} + h_m + h)} \\
a_{u_l^{--}} &= -\frac{h\,h_m}{(h_{mm} + h_m)(h_{mm} + h_m + h)} \\
b_{u_l^{--}} &= \frac{2h(h_m - h)}{(h_{mm} + h_m)(h_{mm} + h_m + h)} \\
c_{u_l^{--}} &= \frac{3h^2}{(h_{mm} + h_m)(h_{mm} + h_m + h)}
\end{aligned} \qquad \text{(B-22)}$$

where

$$h = h_u^l$$

$$h_m = h_u^{l-1}$$

$$h_{mm} = h_u^{l-2} .$$

For equal sized nodes, $h = h_m = h_{mm}$, the expansion coefficients are:

$$a_{u^-_l} = \frac{5}{6}, \qquad a_{u^{--}_l} = -\frac{1}{6},$$

$$b_{u^-_l} = -1 , \qquad b_{u^{--}_l} = 0 ,$$

$$c_{u^-_l} = -1 , \qquad c_{u^{--}_l} = \frac{1}{2} .$$

Substituting Equation (B-21) into Equation (B-1) and solving the resulting equations yields the first and second transverse-leakage moments for the RHS-biased transverse-leakage approximation

$$S_{gu1}^{lmn} = \frac{1}{12}\left[\left(b_{u^-_l} + c_{u^-_l}\right)\overline{S}_{gu}^{l-1,mn} - \left(b_{u^-_l} + c_{u^-_l} + b_{u^{--}_l} + c_{u^{--}_l}\right)\overline{S}_{gu}^{lmn} + \left(b_{u^{--}_l} + c_{u^{--}_l}\right)\overline{S}_{gu}^{l-2,mn}\right] \quad \text{(B-23)}$$

$$S_{gu2}^{lmn} = \frac{1}{60}\left[c_{u^-_l}\overline{S}_{gu}^{l-1,mn} - \left(c_{u^-_l} + c_{u^{--}_l}\right)\overline{S}_{gu}^{lmn} + c_{u^{--}_l}\overline{S}_{gu}^{l-2,mn}\right] . \quad \text{(B-24)}$$

B.4 FLAT TRANSVERSE-LEAKAGE APPROXIMATION

In the Flat Transverse-Leakage Approximation, the shape of the u-directed transverse-leakage is assumed to be spatially uniform (flat) and equal to the node-averaged u-directed transverse-leakage,

$$S_{gu}^{lmn}(u) = \overline{S}_{gu}^{lmn} . \quad \text{(B-25)}$$

Since the u-directed transverse-leakage is uniform, both the first and second transverse-leakage moments are equal to zero,

$$S_{gu1}^{lmn} = 0 \quad \text{(B-26)}$$

$$S_{gu2}^{lmn} = 0 . \quad \text{(B-27)}$$

APPENDIX C

DESCRIPTION OF BENCHMARK PROBLEMS

C.1 TWO-GROUP HOMOGENEOUS BARE CORE BENCHMARK PROBLEM

Geometry:

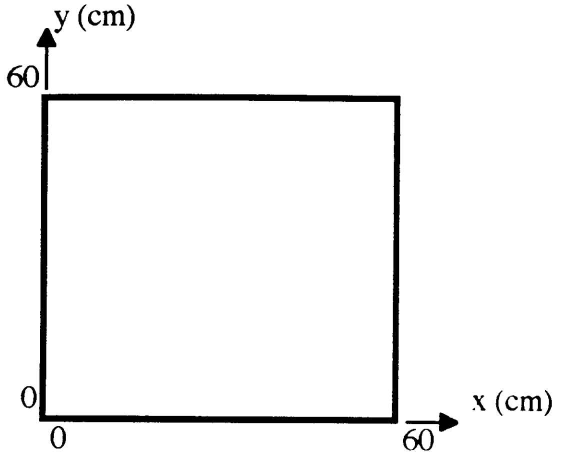

$\phi_g = 0$ boundary conditions on all external boundaries.

Material Properties:

Group, g	D_g (cm)	Σ_{ag} (cm^{-1})	$\nu\Sigma_{fg}$ (cm^{-1})	Σ_{g1} (cm^{-1})	Σ_{g2} (cm^{-1})
1	1.4176	0.00855	0.00536	0.5	0.0
2	0.37336	0.06630	0.10433	0.01742	1.25

$\nu = 2.43$

$\chi_1 = 1.0,\ \chi_2 = 0.0$

$B_z^2 = 0.0\ \text{cm}^{-2}$

The flux is normalized such that,

$$\frac{1}{V_{Core}} \int_{V_{Core}} \sum_{g=1}^{G} \nu\Sigma_{fg}\, \phi_g \, dV = 1 \ .$$

The reference reactor eigenvalue, $\lambda_{ref} = 0.946900410386976$

C.2 SEVEN-GROUP HOMOGENEOUS BARE CORE BENCHMARK PROBLEM

Geometry:

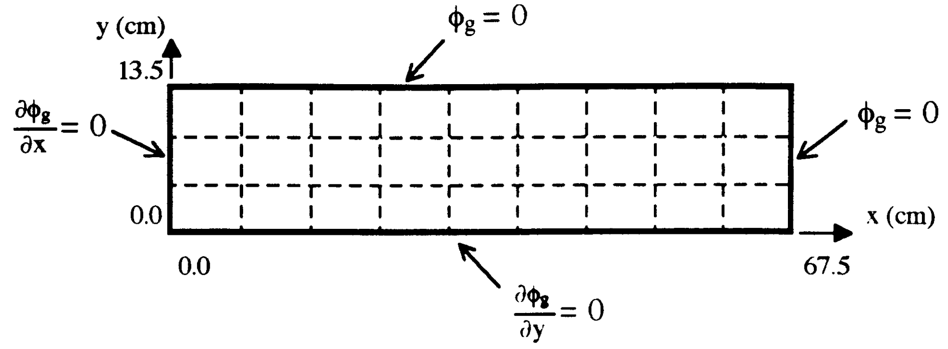

y (cm)
13.5
$\phi_g = 0$
$\frac{\partial \phi_g}{\partial x} = 0$
$\phi_g = 0$
0.0
x (cm)
0.0
67.5
$\frac{\partial \phi_g}{\partial y} = 0$

Material Properties:

g	D_g	Σ_{ag}	$\nu\Sigma_{fg}$	χ_g	Σ_{g1}	Σ_{g2}	Σ_{g3}	Σ_{g4}	Σ_{g5}	Σ_{g6}	Σ_{g7}
1	1.6	0.01	0.02	0.90	0.0	0.0	0.0	0.0	0.0	0.0	0.0
2	1.4	0.02	0.01	0.09	0.015	0.0	0.0	0.0	0.0	0.0	0.0
3	1.2	0.03	0.02	0.01	0.01	0.02	0.0	0.0	0.0	0.0	0.0
4	1.0	0.10	0.04	0.0	0.01	0.02	0.02	0.0	0.0	0.0	0.0
5	0.8	0.05	0.10	0.0	0.005	0.01	0.02	0.03	0.0	0.02	0.02
6	0.6	0.07	0.12	0.0	0.0	0.01	0.01	0.02	0.05	0.0	0.06
7	0.4	0.09	0.15	0.0	0.0	0.0	0.01	0.01	0.03	0.08	0.0

$B_z^2 = 0.0 \text{ cm}^{-2}$

The flux is normalized such that,

$$\frac{1}{V_{Core}} \int_{V_{Core}} \sum_{g=1}^{G} \nu\Sigma_{fg}\, \phi_g \, dV = 1 \, .$$

The reference reactor eigenvalue, $\lambda_{ref} = 0.7745451357$

C.3 IAEA PWR BENCHMARK PROBLEM

Geometry:

Quadrant of Reactor Horizontal Cross Section, Axial Midplane

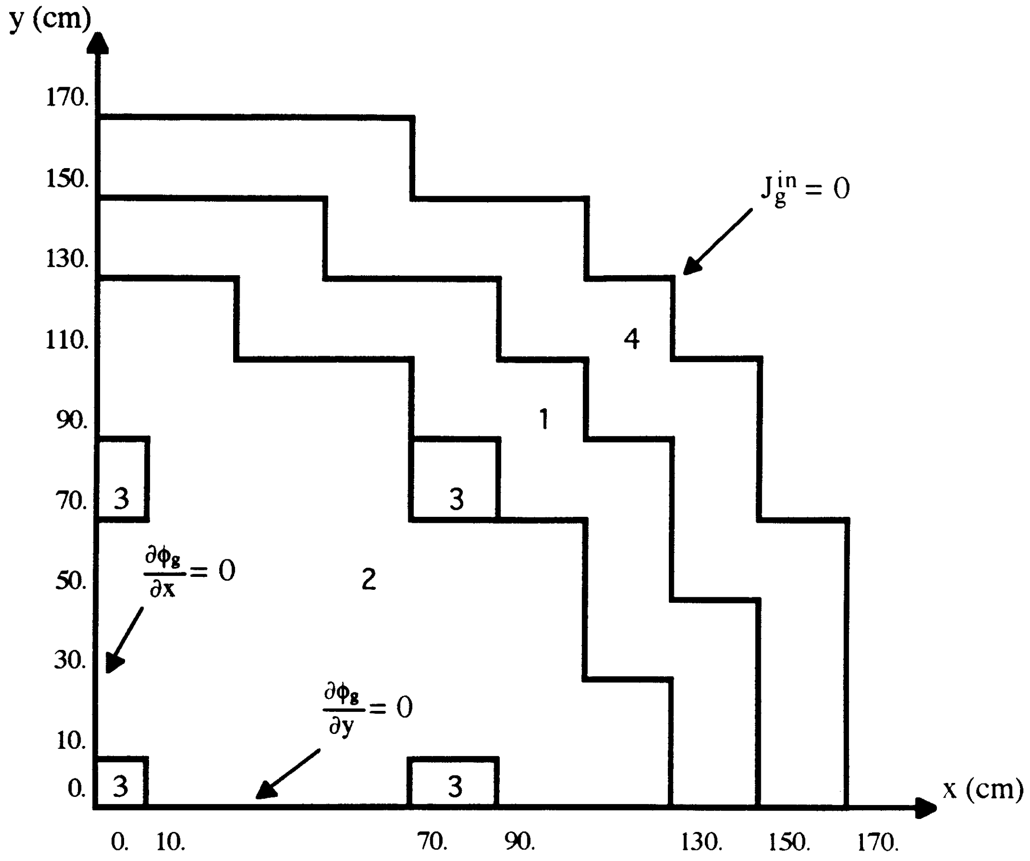
y (cm)
170.
150.
130.
110.
90.
70.
50.
30.
10.
0.
$J_g^{in} = 0$
4
1
3
3
2
$\frac{\partial \phi_g}{\partial x} = 0$
$\frac{\partial \phi_g}{\partial y} = 0$
3
3
x (cm)
0.
10.
70.
90.
130.
150.
170.

Vertical Reactor Cross Section, y = 0

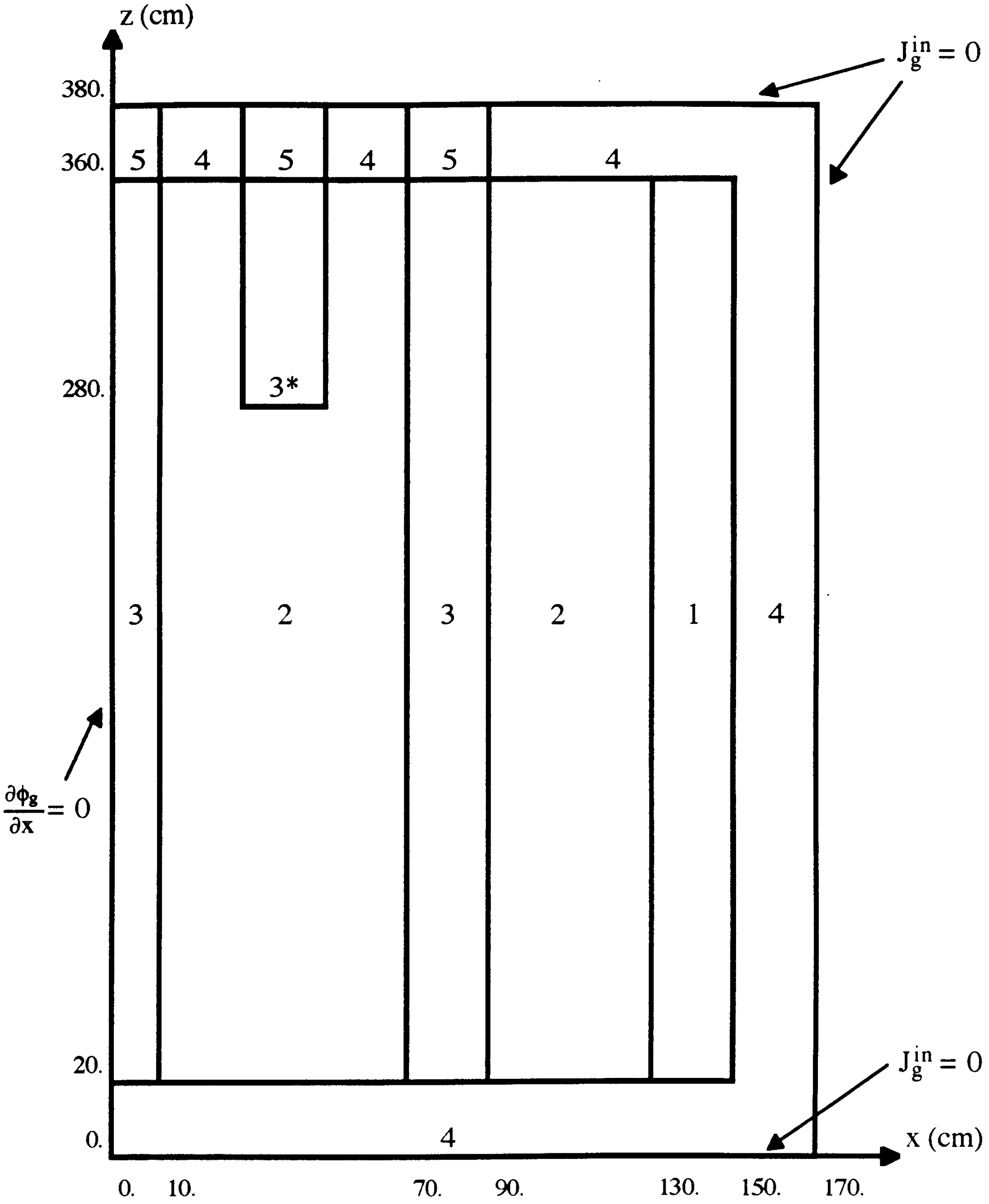
z (cm)
$J_g^{in} = 0$
380.
360.
5
4
5
4
5
4
280.
3*
3
2
3
2
1
4
$\frac{\partial \phi_g}{\partial x} = 0$
20.
$J_g^{in} = 0$
0.
4
x (cm)
0.
10.
70.
90.
130.
150.
170.

*Position of partially-inserted rod: $30.0 < x < 50.0$, $30.0 < y < 50.0$

Material Properties:

Region	Material	Group g	D_g (cm)	Σ_{ag} (cm^{-1})	$\nu\Sigma_{fg}$ (cm^{-1})	Σ_{21} (cm^{-1})
1	Fuel 1	1	1.5	0.01	0.0	0.02
		2	0.4	0.08	0.135	
2	Fuel 2	1	1.5	0.01	0.0	0.02
		2	0.4	0.085	0.135	
3	Fuel 2 + Rod	1	1.5	0.01	0.0	0.02
		2	0.4	0.13	0.135	
4	Reflector	1	2.0	0.0	0.0	0.04
		2	0.3	0.01	0.0	
5	Reflector + Rod	1	2.0	0.0	0.0	0.04
		2	0.3	0.055	0.0	

Axial buckling of 0.8×10^{-4} cm^{-2} for all regions in the 2D problem.

$\chi_1 = 1.0, \chi_2 = 0.0$

Normalization:

The flux is normalized such that

$$\frac{1}{V_{Core}} \int_{V_{Core}} \sum_{g=1}^{G} \nu\Sigma_{fg}\, \phi_g \, dV = 1 \, .$$

C.4 LRA BWR STATIC BENCHMARK PROBLEM

Geometry:

Quadrant of Reactor Horizontal Cross Section

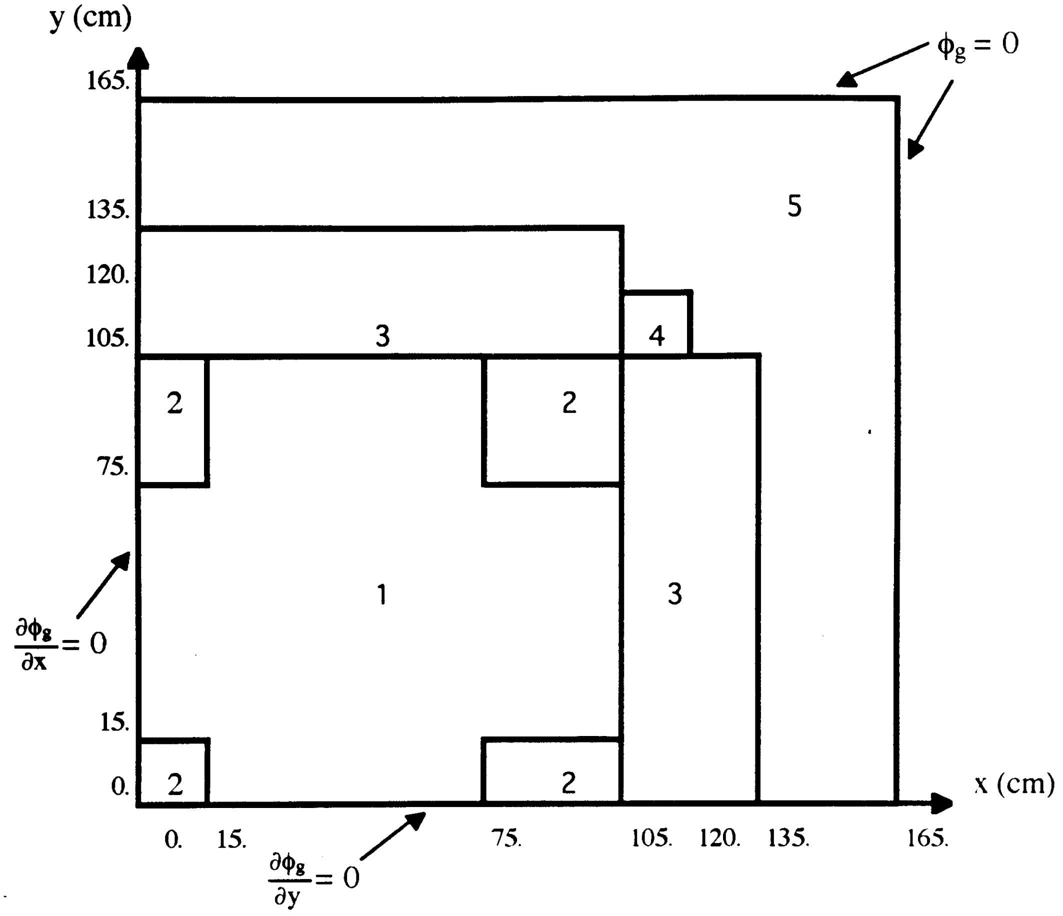
y (cm)
165.
135.
120.
105.
75.
15.
0.
$\phi_g = 0$
5
3
4
2
2
1
3
2
2
$\frac{\partial \phi_g}{\partial x} = 0$
x (cm)
0.
15.
75.
105.
120.
135.
165.
$\frac{\partial \phi_g}{\partial y} = 0$

Vertical Cross Section, y = 0

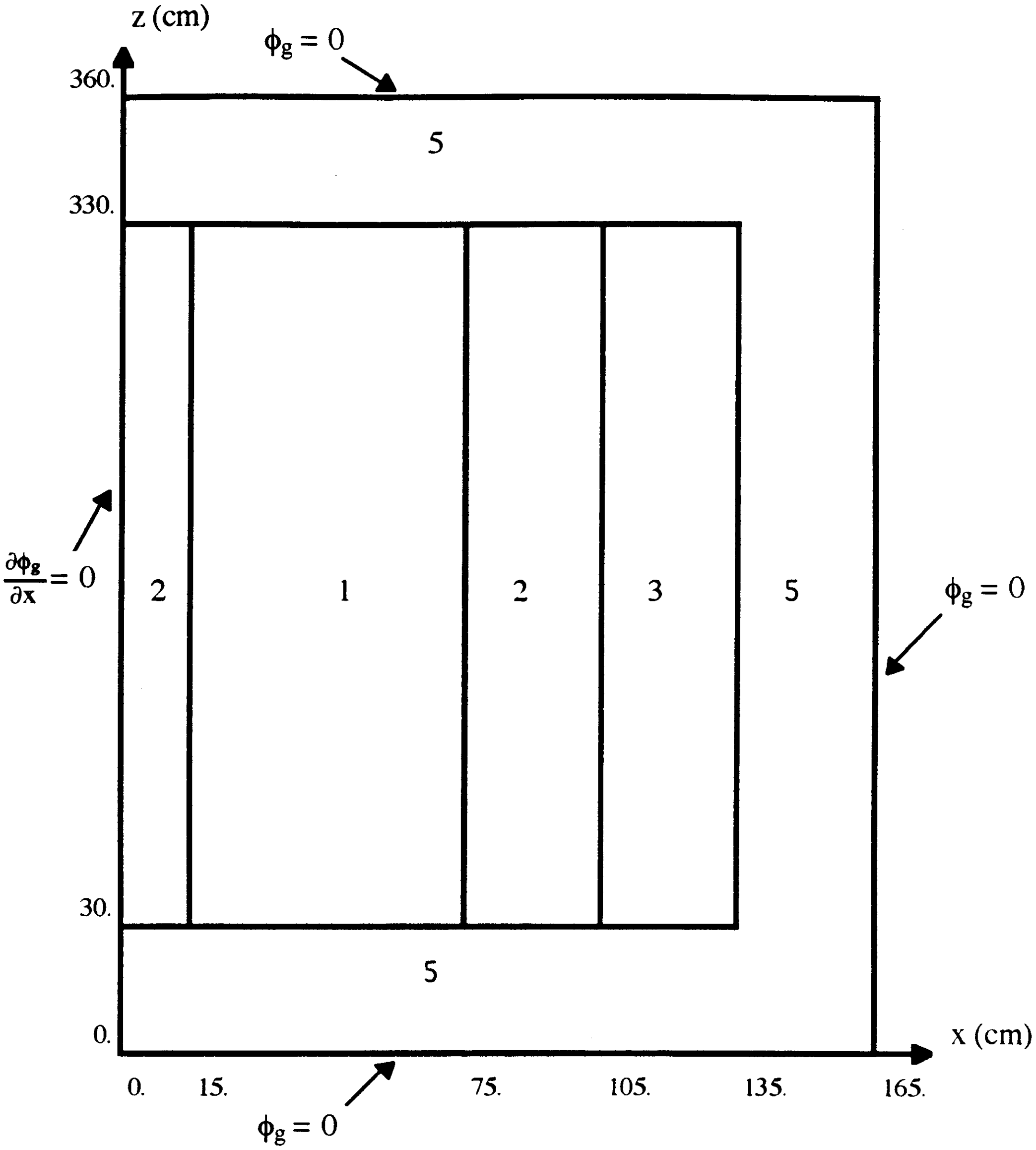
z (cm)
$\phi_g = 0$
360.
330.
30.
0.
5
2
1
2
3
5
5
$\frac{\partial \phi_g}{\partial x} = 0$
$\phi_g = 0$
x (cm)
0.
15.
75.
105.
135.
165.
$\phi_g = 0$

Material Properties:

Region	Material	Group g	D_g (cm)	Σ_{ag} (cm^{-1})	$\nu\Sigma_{fg}$ (cm^{-1})	Σ_{21} (cm^{-1})
1	Fuel 1 (controlled)	1	1.255	0.008252	0.004620	0.02533
		2	0.211	0.1003	0.1091	
2	Fuel 1 (uncontrolled)	1	1.268	0.007181	0.004609	0.02767
		2	0.1902	0.07047	0.08675	
3	Fuel 2 (controlled)	1	1.259	0.008002	0.004663	0.02617
		2	0.2091	0.08344	0.1021	
4	Fuel 2 (uncontrolled)	1	1.259	0.008002	0.004663	0.02617
		2	0.2091	0.0073324	0.1021	
5	Reflector	1	1.257	0.0006034	0.0	0.04754
		2	0.1592	0.01911	0.0	

Axial buckling of 10^{-4} cm^{-2} for all regions in the 2D problem.

$\chi_1 = 1.0, \chi_2 = 0.0$

$\nu = 2.43$

Normalization:

The Flux is normalized to produce a core-averaged power density of 1.0 Wm^{-3},

$$\overline{q}''' = \frac{\varepsilon \times 10^6 \frac{cm^3}{m^3}}{V_{Core}} \int_{V_{Core}} \sum_{g=1}^{G} \Sigma_{fg}\, \phi_g \, dV = 1.0 \ Wm^{-3} ,$$

where

$\varepsilon = 3.204 \times 10^{-11}$ J/fission.

C.5 LMFBR STATIC BENCHMARK PROBLEM

Geometry:

⬚ Inner Core Region [M1]

■ Outer Core Region [M2]

□ Radial Blanket Region [M3]

▨ Axial Blanket Region [M4]

▦ Absorber Region [M5]

▧ Follower Region [M6]

Horizontal cross section of the lower core (rods out):

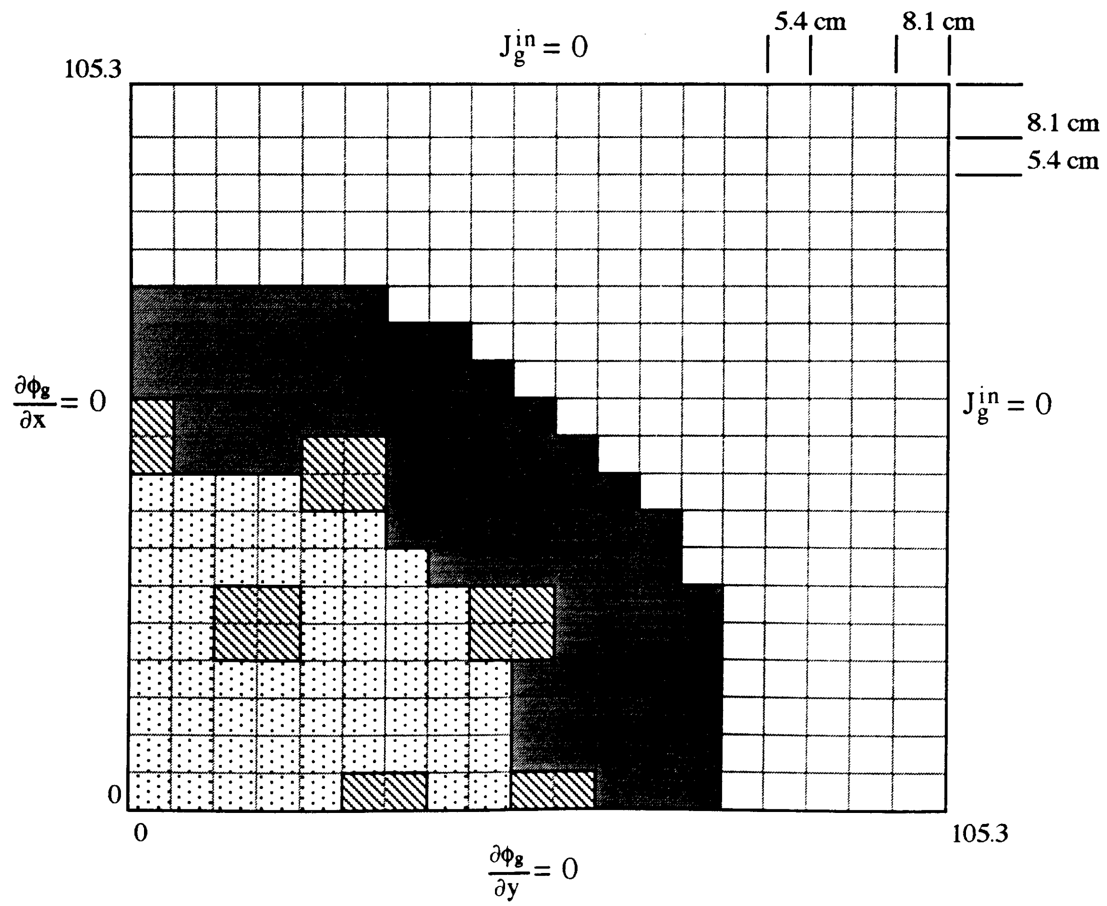

5.4 cm
8.1 cm
$J_g^{in} = 0$
105.3
8.1 cm
5.4 cm
$\frac{\partial \phi_g}{\partial x} = 0$
$J_g^{in} = 0$
0
0
105.3
$\frac{\partial \phi_g}{\partial y} = 0$

Horizontal cross section of the upper core (rods in):

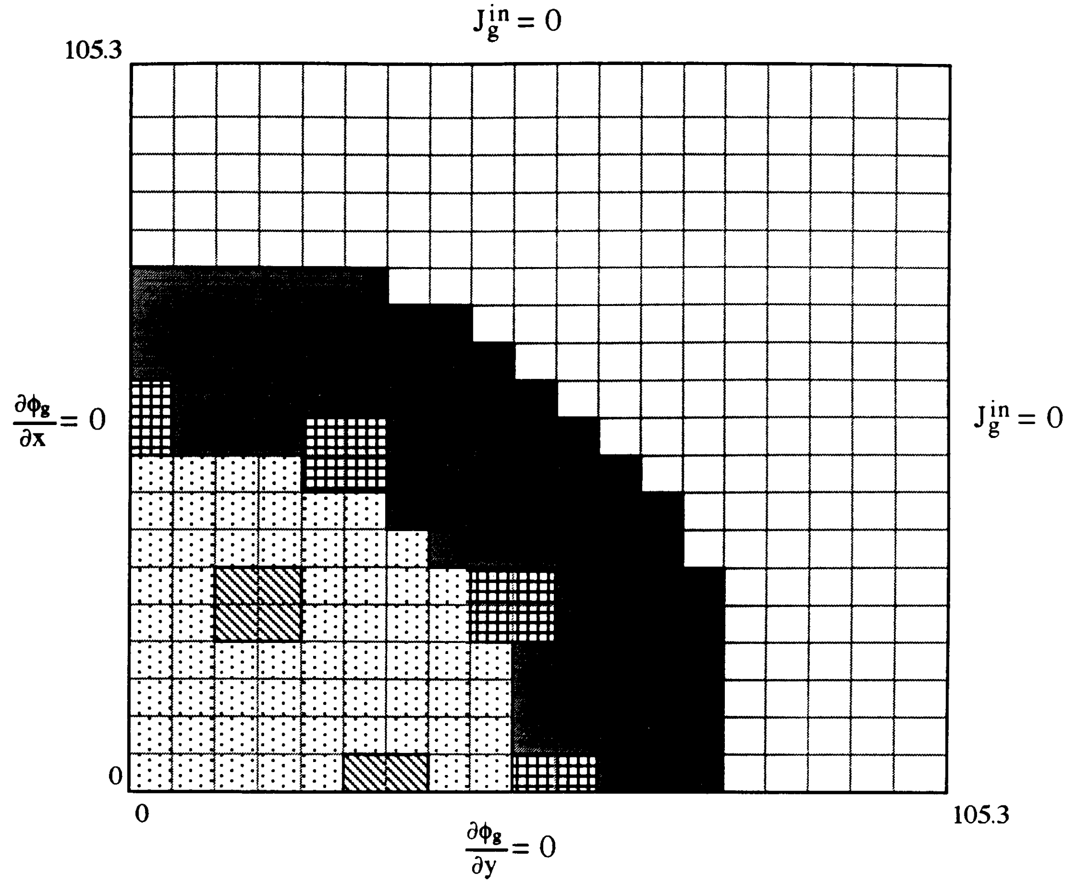

$J_g^{in} = 0$
105.3
$\frac{\partial \phi_g}{\partial x} = 0$
$J_g^{in} = 0$
0
0
105.3
$\frac{\partial \phi_g}{\partial y} = 0$

Axial cross section at y = 0:

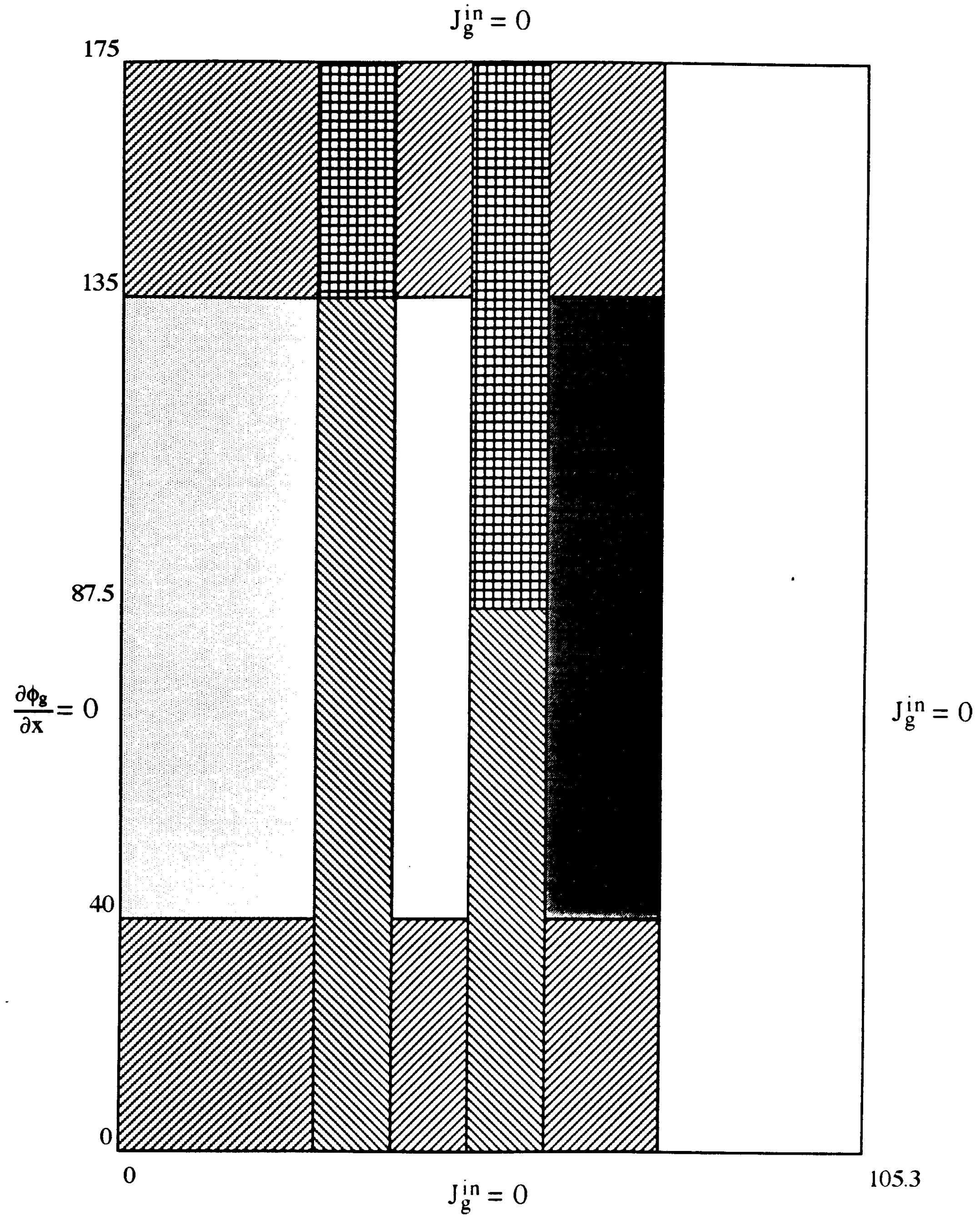

$J_g^{in} = 0$
175
135
87.5
$\frac{\partial \phi_g}{\partial x} = 0$
$J_g^{in} = 0$
40
0
0
105.3
$J_g^{in} = 0$

Material Properties:

Material	Group, g	D_g	Σ_{rg}	$\nu\Sigma_{fg}$	Σ_{fg}
1	1	2.8768	2.8204×10^{-2}	1.1878×10^{-2}	3.9123×10^{-3}
	2	1.5708	5.2747×10^{-3}	5.3252×10^{-3}	1.8286×10^{-3}
	3	0.72249	1.7612×10^{-2}	1.0471×10^{-2}	3.6334×10^{-3}
	4	0.96420	2.6546×10^{-2}	2.6611×10^{-2}	9.2415×10^{-3}
2	1	2.8765	2.8782×10^{-2}	1.4943×10^{-2}	4.8531×10^{-3}
	2	1.5714	6.0491×10^{-3}	7.6887×10^{-3}	2.6377×10^{-3}
	3	0.71271	1.9510×10^{-2}	1.4809×10^{-2}	5.1332×10^{-3}
	4	0.94298	3.3714×10^{-2}	3.8159×10^{-2}	1.3238×10^{-2}
3	1	2.2856	3.5959×10^{-2}	7.7427×10^{-3}	2.7688×10^{-3}
	2	1.1719	5.8855×10^{-3}	1.0825×10^{-4}	4.4347×10^{-5}
	3	0.63248	1.6041×10^{-2}	2.9742×10^{-4}	1.2274×10^{-4}
	4	0.81836	1.3349×10^{-2}	8.4687×10^{-4}	3.4952×10^{-4}
4	1	2.7167	2.9093×10^{-2}	5.4279×10^{-3}	1.9453×10^{-3}
	2	1.4409	4.4909×10^{-3}	7.5857×10^{-5}	3.1065×10^{-5}
	3	0.72035	1.3082×10^{-2}	2.1218×10^{-4}	8.7566×10^{-5}
	4	0.98768	9.9562×10^{-3}	5.7592×10^{-4}	2.3769×10^{-4}
5	1	2.5031	2.4814×10^{-2}	0.0	0.0
	2	1.3147	1.6412×10^{-2}	0.0	0.0
	3	0.57428	7.2122×10^{-2}	0.0	0.0
	4	0.61537	1.6868×10^{-1}	0.0	0.0
6	1	4.6164	1.3159×10^{-2}	0.0	0.0
	2	2.9018	1.4559×10^{-3}	0.0	0.0
	3	1.0212	4.6001×10^{-3}	0.0	0.0
	4	1.7296	7.8660×10^{-4}	0.0	0.0

Material Properties: (continued)

Material	Group g	Σ_{g1}	Σ_{g2}	Σ_{g3}	Σ_{g4}
1	1	0.0	0.0	0.0	0.0
	2	2.3597×10^{-2}	0.0	0.0	0.0
	3	4.0791×10^{-6}	1.6153×10^{-3}	0.0	0.0
	4	4.4493×10^{-8}	4.2309×10^{-8}	4.6838×10^{-3}	0.0
2	1	0.0	0.0	0.0	0.0
	2	2.3262×10^{-2}	0.0	0.0	0.0
	3	4.6451×10^{-6}	1.5718×10^{-3}	0.0	0.0
	4	4.9968×10^{-8}	4.0724×10^{-8}	4.3414×10^{-3}	0.0
3	1	0.0	0.0	0.0	0.0
	2	3.2071×10^{-2}	0.0	0.0	0.0
	3	3.8880×10^{-6}	2.7776×10^{-3}	0.0	0.0
	4	4.5039×10^{-8}	9.0018×10^{-8}	5.8971×10^{-3}	0.0
4	1	0.0	0.0	0.0	0.0
	2	2.6322×10^{-2}	0.0	0.0	0.0
	3	2.8907×10^{-6}	2.2889×10^{-3}	0.0	0.0
	4	3.3248×10^{-8}	6.2133×10^{-8}	5.3536×10^{-3}	0.0
5	1	0.0	0.0	0.0	0.0
	2	2.2946×10^{-2}	0.0	0.0	0.0
	3	1.0320×10^{-6}	3.7687×10^{-3}	0.0	0.0
	4	1.0489×10^{-8}	7.0361×10^{-12}	8.6815×10^{-3}	0.0
6	1	0.0	0.0	0.0	0.0
	2	1.2942×10^{-2}	0.0	0.0	0.0
	3	6.8780×10^{-7}	1.2871×10^{-3}	0.0	0.0
	4	6.9903×10^{-9}	4.3633×10^{-12}	3.4533×10^{-3}	0.0

Note:

$$\Sigma_{rg} = \Sigma_{tg} - \Sigma_{gg}$$

Zero axial buckling for all material regions in the 2D problems.

Normalization:

The flux is normalized such that

$$\frac{1}{V_{Core}} \int_{V_{Core}} \sum_{g=1}^{G} \nu\Sigma_{fg}\, \phi_g \, dV = 1 \ .$$

In this expression the core is considered to be all fuel bearing material in the reactor.

C.6 CISE BWR BENCHMARK PROBLEM

Geometry:

Quadrant of the 2D Reactor

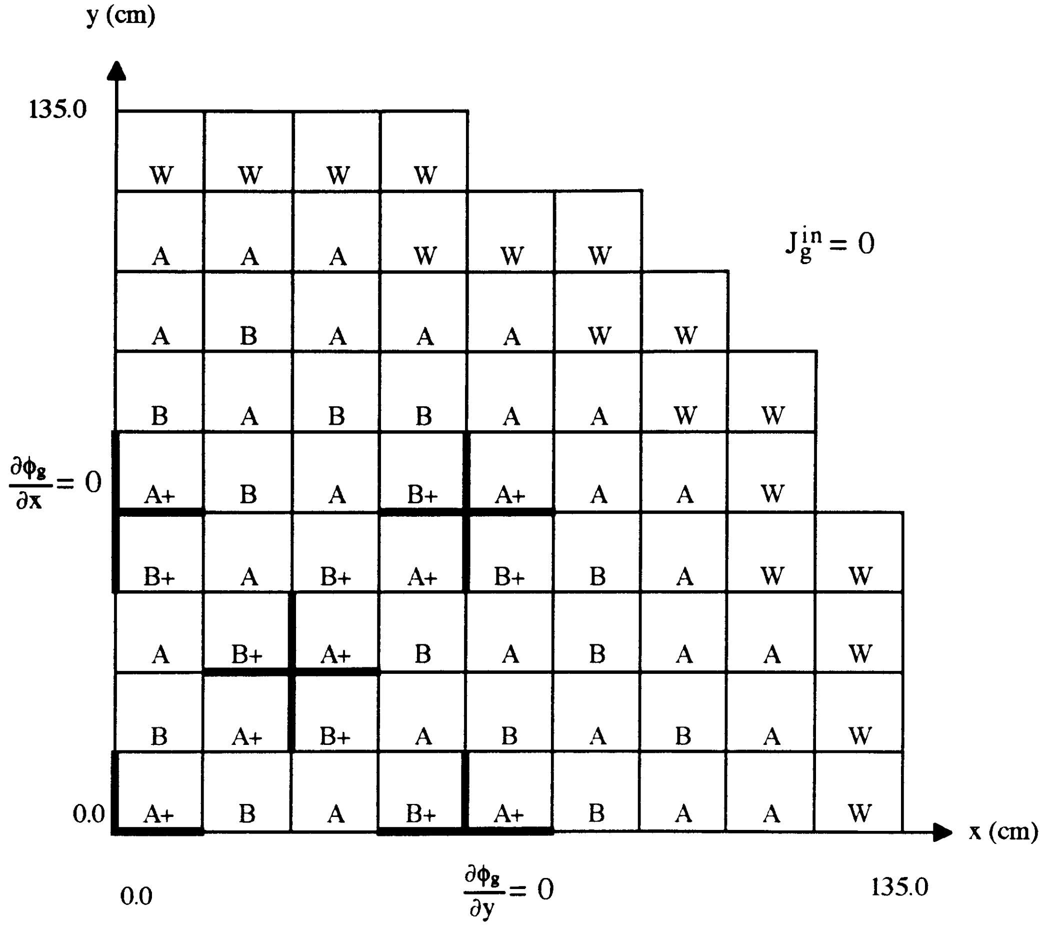
y (cm)
135.0
$J_g^{in} = 0$
$\frac{\partial \phi_g}{\partial x} = 0$
0.0
0.0
$\frac{\partial \phi_g}{\partial y} = 0$
135.0
x (cm)

W	W	W	W					
A	A	A	W	W	W			
A	B	A	A	A	W	W		
B	A	B	B	A	A	W	W	
A+	B	A	B+	A+	A	A	W	
B+	A	B+	A+	B+	B	A	W	W
A	B+	A+	B	A	B	A	A	W
B	A+	B+	A	B	A	B	A	W
A+	B	A	B+	A+	B	A	A	W

Axial Buckling of 0.0 cm^{-2} for all materials.

Fuel Assembly Description by Zone:

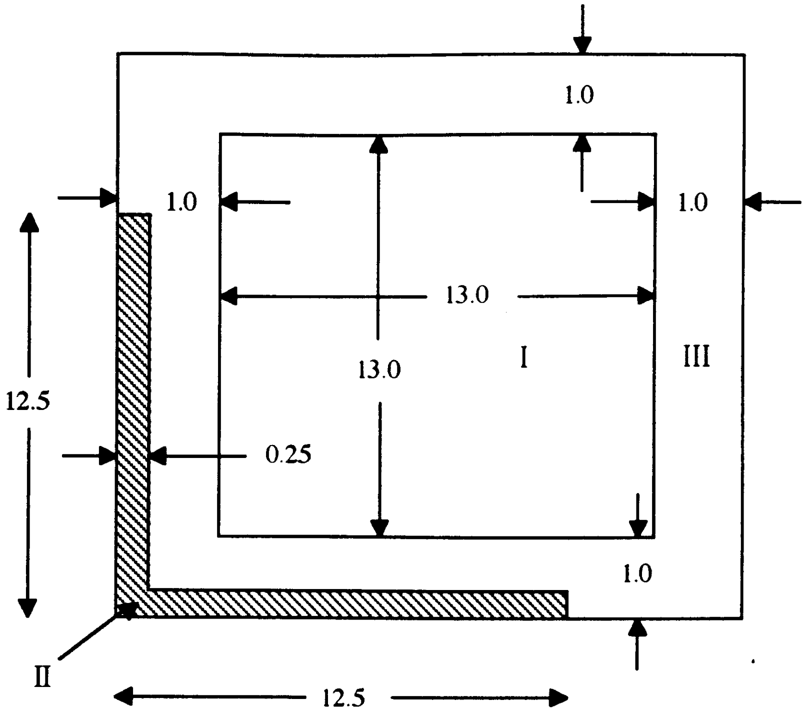
1.0
1.0
1.0
13.0
13.0
I
III
12.5
0.25
1.0
II
12.5

Material to Zone Assignments by Assembly Type:

Zone	Assembly Type A	A+	B	B+	W
I	3	3	4	4	2
II	2	1	2	1	2
III	2	2	2	2	2

Material Properites of Fuel Assembly Zones:

Material	Group g	D_g (cm)	Σ_{ag} (cm^{-1})	$\nu\Sigma_{fg}$ (cm^{-1})	Σ_{2g} (cm^{-1})
1	1	3.00	0.08	0.0	0.0
(Control Blade)	2	0.15	1.00	0.0	
2	1	2.00	0.0	0.0	0.04
(Water)	2	0.30	0.01	0.0	
3	1	1.80	0.008	0.006	0.012
(Fresh Fuel)	2	0.55	0.085	0.110	
4	1	1.80	0.008	0.005	0.012
(Depleted Fuel)	2	0.55	0.085	0.100	

$\chi_1 = 1.0$

$\chi_2 = 0.0$

$\nu = 2.5$

Flux-Weighted Constants for the CISE BWR Problem:

Assembly Type	Group g	$\hat{D}_g$ (cm)	$\hat{\Sigma}_{ag}$ (cm^{-1})	$\nu\hat{\Sigma}_{fg}$ (cm^{-1})	$\hat{\Sigma}_{2g}$ (cm^{-1})
A	1	1.8440	0.00607	0.004556	0.01874
(Fresh Fuel)	2	0.4284	0.05946	0.07254	0.0
A+	1	1.8580	0.00804	0.004565	0.01772
(Fresh Fuel, controlled)	2	0.4283	0.07416	0.07558	0.0
B	1	1.8440	0.00608	0.003796	0.01874
(Depleted Fuel)	2	0.4284	0.05946	0.06595	0.0
B+	1	1.8580	0.00804	0.003804	0.01772
(Depleted Fuel, controlled)	2	0.4283	0.07415	0.06870	0.0
W	1	2.0000	0.0	0.0	0.04
(Water)	2	0.3000	0.01	0.0	0.0

$\chi_1 = 1.0$

$\chi_2 = 0.0$

$\nu = 2.5$

Assembly Discontinuity Factors for the CISE BWR Problem:

Assembly Type	Group g	f_{gx-}	f_{gx+}	f_{gy-}	f_{gy+}
A	1	0.9623	0.9623	0.9623	0.9623
	2	1.4510	1.4510	1.4510	1.4510
A+	1	0.8955	1.0150	0.8955	1.0150
	2	0.6492	1.8880	0.6492	1.8880
B	1	0.9625	0.9625	0.9625	0.9625
	2	1.4510	1.4510	1.4510	1.4510
B+	1	0.8949	1.0160	0.8949	1.0160
	2	0.6488	1.8890	0.6488	1.8890
W	1	1.0	1.0	1.0	1.0
	2	1.0	1.0	1.0	1.0

Assembly Surface Orientation:

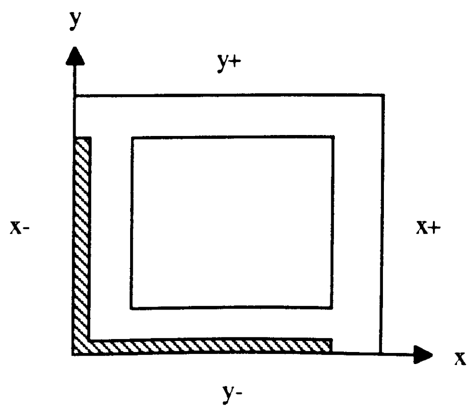

C.7 HAFAS BWR BENCHMARK PROBLEM

Geometry:

Quadrant of the 2D Reactor

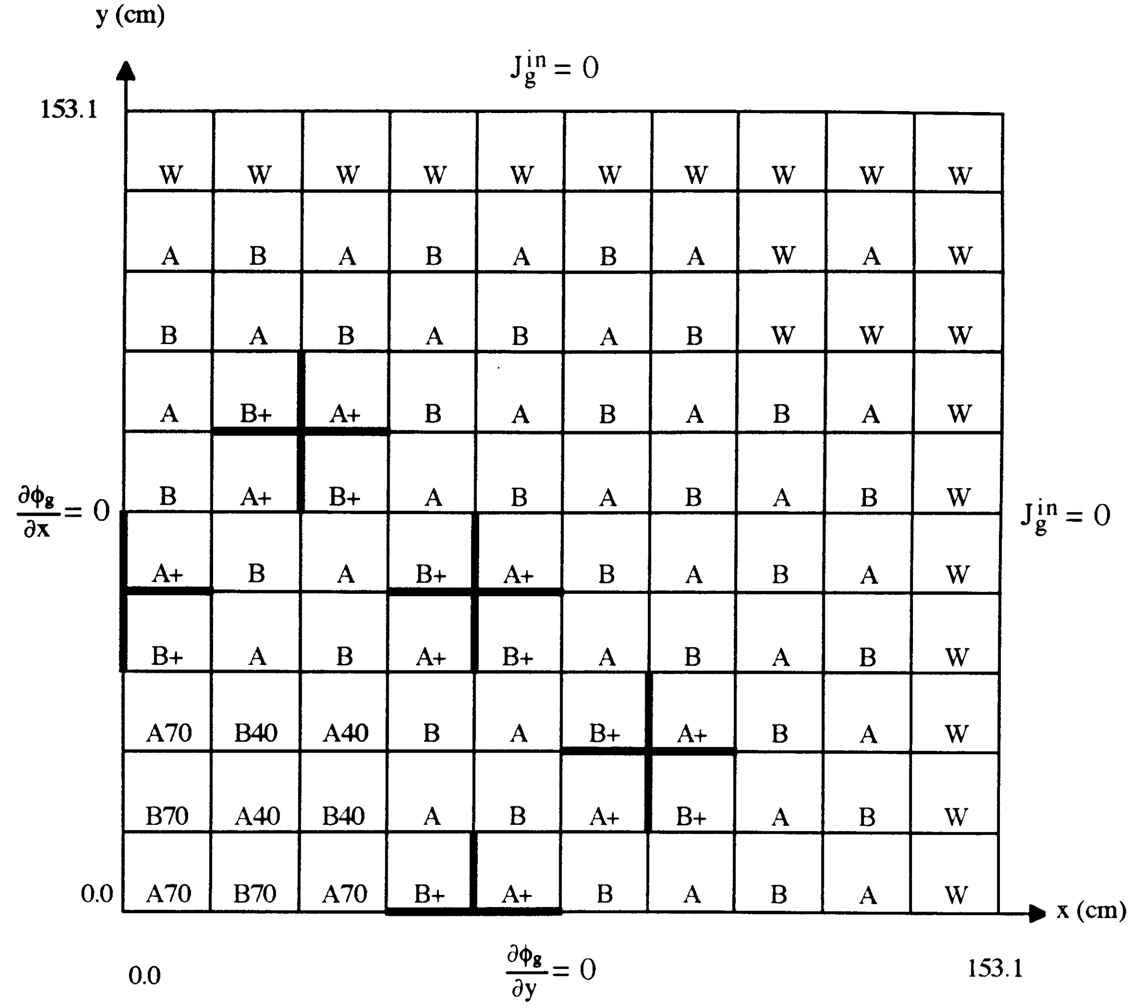

y (cm)
153.1
$J_g^{in} = 0$
$\frac{\partial \phi_g}{\partial x} = 0$
$J_g^{in} = 0$
0.0
x (cm)
0.0
$\frac{\partial \phi_g}{\partial y} = 0$
153.1

W	W	W	W	W	W	W	W	W	W
A	B	A	B	A	B	A	W	A	W
B	A	B	A	B	A	B	W	W	W
A	B+	A+	B	A	B	A	B	A	W
B	A+	B+	A	B	A	B	A	B	W
A+	B	A	B+	A+	B	A	B	A	W
B+	A	B	A+	B+	A	B	A	B	W
A70	B40	A40	B	A	B+	A+	B	A	W
B70	A40	B40	A	B	A+	B+	A	B	W
A70	B70	A70	B+	A+	B	A	B	A	W

Axial Buckling of 0.0 cm^{-2} for all materials.

Fuel Assembly Description by Zone:

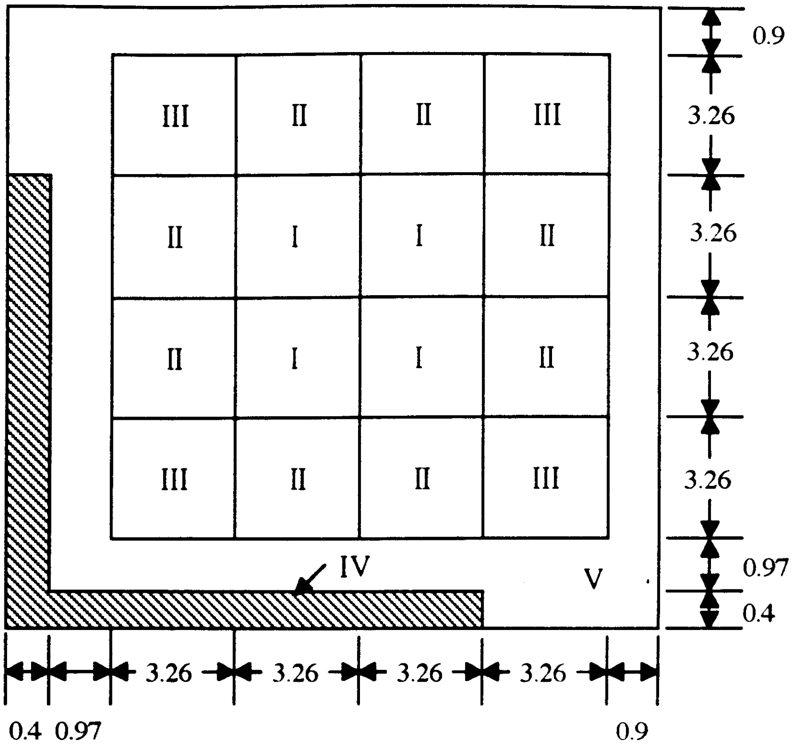
III
II
II
III
II
I
I
II
II
I
I
II
III
II
II
III
IV
V
0.9
3.26
3.26
3.26
3.26
0.97
0.4
3.26
3.26
3.26
3.26
0.4 0.97
0.9

Material to Zone Assignments by Assembly Type:

Zone	Assembly Type								
	A	A40	A70	A+	B	B40	B70	B+	W
I	1	5	9	1	2	6	10	2	15
II	2	6	10	2	3	7	11	3	15
III	3	7	11	3	4	8	12	4	15
IV	13	13	13	14	13	13	13	14	15
V	13	13	13	13	13	13	13	13	15

Material Properites of Fuel Assembly Zones:

Material	Group g	D_g (cm)	Σ_{ag} (cm^{-1})	$\nu\Sigma_{fg}$ (cm^{-1})	Σ_{2g} (cm^{-1})
1	1	1.400	0.009	0.0065	0.016
(Fuel a, void = 0%)	2	0.375	0.080	0.1220	
2	1	1.400	0.009	0.0057	0.017
(Fuel b, void = 0%)	2	0.375	0.070	0.1000	
3	1	1.400	0.009	0.0051	0.018
(Fuel c, void = 0%)	2	0.375	0.060	0.0800	
4	1	1.400	0.009	0.0051	0.018
(Fuel d, void = 0%)	2	0.375	0.050	0.0700	
5	1	1.680	0.008	0.0063	0.010
(Fuel a, void = 40%)	2	0.530	0.077	0.1180	
6	1	1.680	0.0085	0.0055	0.0105
(Fuel b, void = 40%)	2	0.530	0.067	0.0960	
7	1	1.680	0.009	0.0049	0.0110
(Fuel c, void = 40%)	2	0.530	0.057	0.0780	
8	1	1.680	0.009	0.0049	0.0110
(Fuel d, void = 40%)	2	0.530	0.047	0.0680	

Material Properites of Fuel Assembly Zones: (continued)

Material	Group g	D_g (cm)	Σ_{ag} (cm^{-1})	$\nu\Sigma_{fg}$ (cm^{-1})	Σ_{2g} (cm^{-1})
9	1	2.000	0.0078	0.0061	0.0052
(Fuel a, void = 70%)	2	0.800	0.073	0.1140	
10	1	2.000	0.0082	0.0053	0.0053
(Fuel b, void = 70%)	2	0.800	0.0630	0.0920	
11	1	2.000	0.0086	0.0047	0.0054
(Fuel c, void = 70%)	2	0.800	0.0530	0.0720	
12	1	2.000	0.0086	0.0047	0.0054
(Fuel d, void = 70%)	2	0.800	0.043	0.0620	
13	1	1.530	0.0005	0.0	0.031
(Fuel can and water)	2	0.295	0.0090	0.0	
14	1	1.110	0.08375	0.0	0.00375
(Control blade)	2	0.185	0.950	0.0	
15	1	2.000	0.0	0.0	0.04
(Water)	2	0.300	0.010	0.0	

$\chi_1 = 1.0$

$\chi_2 = 0.0$

$\nu = 2.5$

Flux-Weighted Constants for the HAFAS BWR Problem:

Assembly Type	Group g	$\hat{D}_g$ (cm)	$\hat{\Sigma}_{ag}$ (cm^{-1})	$\nu\hat{\Sigma}_{fg}$ (cm^{-1})	$\hat{\Sigma}_{2g}$ (cm^{-1})
A (Fresh fuel 0% void)	1	1.4320	0.00678	0.004255	0.02065
	2	0.3414	0.04713	0.06249	
A40 (Fresh fuel, 40% void)	1	1.6380	0.00639	0.004099	0.01588
	2	0.4097	0.04486	0.05972	
A70 (Fresh fuel, 70% void)	1	1.8500	0.00616	0.003946	0.01208
	2	0.4890	0.04221	0.05661	
A+ (Fresh fuel, controlled)	1	1.4160	0.00927	0.004304	0.01974
	2	0.3441	0.06099	0.06894	
B (Depleted fuel, 0% void)	1	1.4320	0.00678	0.003879	0.02121
	2	0.3424	0.04144	0.05255	
B40 (Depleted fuel, 40% void)	1	1.6380	0.00667	0.003725	0.01617
	2	0.4128	0.0392	0.05052	
B70 (Depleted fuel, 70% void)	1	1.8500	0.00638	0.003573	0.01214
	2	0.4955	0.03655	0.04677	
B+ (Depleted fuel, controlled)	1	1.4160	0.00926	0.003924	0.02031
	2	0.3451	0.05405	0.05773	

Flux-Weighted Constants for the HAFAS BWR Problem: (continued)

Assembly Type	Group g	$\hat{D}_g$ (cm)	$\hat{\Sigma}_{ag}$ (cm^{-1})	$\nu\hat{\Sigma}_{fg}$ (cm^{-1})	$\hat{\Sigma}_{2g}$ (cm^{-1})
W	1	2.0	0.0	0.0	0.04
(Water)	2	0.3	0.01	0.0	

$\chi_1 = 1.0$

$\chi_2 = 0.0$

$\nu = 2.5$

Assembly Discontinuity Factors for the HAFAS BWR Problem:

Assembly Type	Group g	f_{gx-}	f_{gx+}	f_{gy-}	f_{gy+}
A	1	0.9311	0.9677	0.9311	0.9677
	2	1.4740	1.2470	1.4740	1.2470
A40	1	0.9368	0.9709	0.9368	0.9709
	2	1.5330	1.2550	1.5330	1.2550
A70	1	0.9406	0.9739	0.9406	0.9739
	2	1.5830	1.2560	1.5830	1.2560
A+	1	0.8169	1.0570	0.8169	1.0570
	2	0.6264	1.7320	0.6264	1.7320
B	1	0.9313	0.9694	0.9313	0.9694
	2	1.4070	1.2130	1.4070	1.2130
B40	1	0.9372	0.9724	0.9372	0.9724
	2	1.4610	1.2200	1.4610	1.2200
B70	1	0.9407	0.9759	0.9407	0.9759
	2	1.5060	1.2210	1.5060	1.2210
B+	1	0.8151	1.0610	0.8151	1.0610
	2	0.5902	1.6830	0.5902	1.6830
W	1	1.0	1.0	1.0	1.0
	2	1.0	1.0	1.0	1.0

Assembly Surface Orientation:

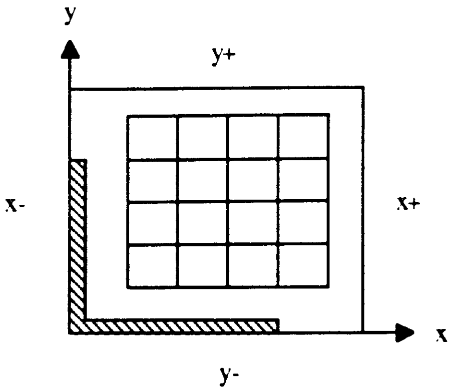

C.8 TWO-GROUP SOURCE BENCHMARK PROBLEM

Geometry:

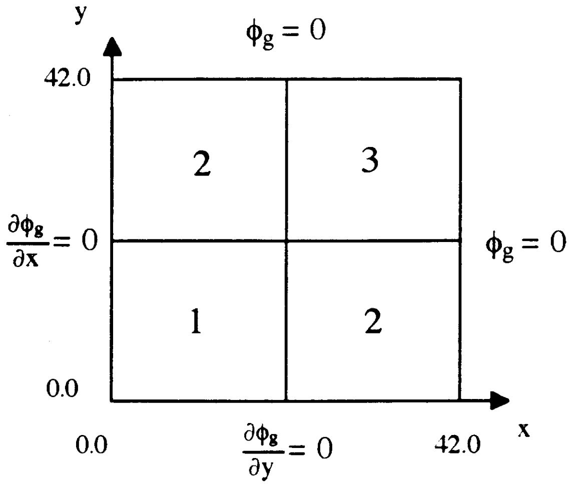
y
$\phi_g = 0$
42.0
2
3
$\frac{\partial \phi_g}{\partial x} = 0$
$\phi_g = 0$
1
2
0.0
0.0
$\frac{\partial \phi_g}{\partial y} = 0$
42.0
x

Material Properties:

Material	Group g	D_g (cm)	Σ_{ag} (cm^{-1})	$\nu\Sigma_{fg}$ (cm^{-1})	Σ_{21} (cm^{-1})
1	1	1.4719	0.017864	0.0060282	0.018824
	2	0.39021	0.21535	0.22912	
2	1	1.5150	0.009325	0.0046245	0.021126
	2	0.3957	0.14157	0.16483	
3	1	1.5150	0.009325	0.0046245	0.021126
	2	0.3957	0.14157	0.16483	

Material Properties: (continued)

Material	Group g	q_g (n cm^{-3} s^{-1})
1	1	1.73679×10^7
	2	0.0
2	1	1.70058×10^7
	2	0.0
3	1	9.29477×10^6
	2	0.0

$\chi_1 = 1.0$

$\chi_2 = 0.0$

$\nu = 2.5$

Axial Buckling of 0.0 cm^{-2} for all materials.

Energy Conversion Factor: 3.204×10^{-11} J/fission

APPENDIX D

CORE MAPS

	Max
Reference ------------	2.3443
CMFD Error (%) -------	0.02
Quadratic Error (%) -----	0.03
Cubic Error (%) --------	0.02
Quartic Error (%) -------	0.02

0.6281 0.00 0.00 0.00 0.00	0.6091 -0.01 -0.01 -0.01 -0.01	0.5715 -0.01 -0.01 0.00 0.00	0.5165 0.00 0.00 0.00 0.00	0.4459 0.00 0.00 0.00 0.00	0.3617 0.00 0.00 0.00 0.00	0.2665 0.00 0.00 0.00 0.00	0.1632 0.00 0.00 -0.01 -0.01	0.0550 0.00 0.00 -0.01 -0.01
1.7161 -0.01 -0.01 0.00 0.00	1.6640 -0.01 -0.02 0.00 0.00	1.5613 -0.01 -0.01 0.00 0.00	1.4111 0.00 0.00 0.01 0.01	1.2181 0.01 0.01 0.01 0.01	0.9881 0.01 0.01 0.00 0.00	0.7280 0.01 0.01 0.00 0.00	0.4459 0.00 0.00 -0.02 -0.02	0.1501 0.01 0.01 0.00 -0.01
2.3443 -0.02 -0.03 0.00 0.00	2.2730 -0.01 -0.01 0.01 0.01	2.1327 -0.01 -0.01 0.01 0.01	1.9276 0.00 0.00 0.02 0.02	1.6640 0.00 0.00 0.01 0.01	1.3497 0.02 0.02 0.01 0.01	0.9945 0.01 0.01 0.00 0.00	0.6091 0.00 0.01 -0.02 -0.02	0.2051 0.00 0.00 -0.01 -0.01

℄

℄

Figure D-1. Seven-Group Homogeneous Bare Core Problem: Error in Normalized Nodal Power Density.

	Average
Reference - - - - - - - - - - - - - - - - - -	1.0000
Error (%), 20x20 cm - - - - - - - - - - -	0.77
Error (%), 10x10 cm - - - - - - - - - - -	0.02
Error (%), 5x5 cm - - - - - - - - - - - - -	0.00

	0.7549 -0.85 -0.05 0.01	0.7358 -0.93 -0.03 0.00	0.6921 -1.13 0.01 0.00					
	0.9343 -0.50 -0.01 0.01	0.9504 -0.63 -0.02 0.00	0.9752 -0.86 -0.03 0.00	0.8461 -1.07 0.00 -0.01	0.5972 -1.11 0.00 -0.01			
	0.9351 0.25 0.02 0.00	1.0361 0.00 0.01 0.01	1.0705 -0.14 -0.01 0.00	0.9064 -0.44 0.02 0.00	0.6856 -0.51 0.03 -0.01	0.5849 -1.51 0.02 -0.01		
	0.6100 0.10 -0.05 0.00	1.0697 0.66 0.02 0.00	1.1792 0.54 0.01 0.01	0.9670 0.44 0.02 0.00	0.4706 -0.45 -0.04 0.00	0.6856 -0.51 0.03 -0.01	0.5972 -1.11 0.00 -0.01	
	1.2107 1.01 0.02 0.00	1.3149 0.98 0.02 0.00	1.3451 1.03 0.00 0.00	1.1929 0.71 0.01 0.00	0.9670 0.44 0.02 0.00	0.9064 -0.44 0.02 0.00	0.8461 -1.07 0.00 -0.01	
	1.4537 1.10 0.00 0.00	1.4799 1.31 -0.01 0.00	1.4694 1.19 -0.02 0.00	1.3451 1.03 0.00 0.00	1.1792 0.54 0.01 0.01	1.0705 -0.14 -0.01 0.00	0.9752 -0.86 -0.03 0.00	0.6921 -1.13 0.01 0.00
	1.3097 1.19 0.02 -0.01	1.4351 1.26 0.01 0.00	1.4799 1.31 -0.01 0.00	1.3149 0.98 0.02 0.00	1.0697 0.66 0.02 0.00	1.0361 0.00 0.01 0.01	0.9504 -0.63 -0.02 0.00	0.7358 -0.93 -0.03 0.00
℄ --	0.7456 0.77 -0.07 0.00	1.3097 1.19 0.02 -0.01	1.4537 1.10 0.00 0.00	1.2107 1.01 0.02 0.00	0.6100 0.10 -0.05 0.00	0.9351 0.25 0.02 0.00	0.9343 -0.50 -0.01 0.01	0.7549 -0.85 -0.05 0.01

|
|
℄

Figure D-2. 2D IAEA PWR Benchmark Problem: Error in Normalized Assembly Power Density.

	Average
Reference ------------------	1.0000
Relative Error (%), 20x20 cm -----	0.74
Relative Error (%), 10x10 cm -----	0.02
Relative Error (%), 5x5 cm -------	0.00

0.7549 -1.30 -0.07 0.01	0.7358 -1.37 -0.04 0.00	0.6921 -1.39 0.01 0.00					
0.9343 -0.58 -0.01 0.01	0.9504 -0.65 -0.02 0.00	0.9752 -0.78 -0.03 0.00	0.8461 -1.29 0.00 -0.01	0.5972 -1.57 0.00 -0.02			
0.9351 0.23 0.02 0.00	1.0361 -0.02 0.01 0.01	1.0705 -0.12 -0.01 0.00	0.9064 -0.37 0.02 0.00	0.6856 -0.33 0.04 -0.01	0.5849 -2.01 0.03 -0.02		
0.6100 0.09 -0.08 0.00	1.0697 0.56 0.02 0.00	1.1792 0.43 0.01 0.01	0.9670 0.48 0.02 0.00	0.4706 -0.80 -0.08 0.00	0.6856 -0.33 0.04 -0.01	0.5972 -1.57 0.00 -0.02	
1.2107 0.74 0.02 0.00	1.3149 0.66 0.02 0.00	1.3451 0.70 0.00 0.00	1.1929 0.57 0.01 0.00	0.9670 0.48 0.02 0.00	0.9064 -0.37 0.02 0.00	0.8461 -1.29 0.00 -0.01	
1.4537 0.64 0.00 0.00	1.4799 0.78 -0.01 0.00	1.4694 0.72 -0.01 0.00	1.3451 0.70 0.00 0.00	1.1792 0.43 0.01 0.01	1.0705 -0.12 -0.01 0.00	0.9752 -0.78 -0.03 0.00	0.6921 -1.39 0.01 0.00
1.3097 0.79 0.02 -0.01	1.4351 0.76 0.01 0.00	1.4799 0.78 -0.01 0.00	1.3149 0.66 0.02 0.00	1.0697 0.56 0.02 0.00	1.0361 -0.02 0.01 0.01	0.9504 -0.65 -0.02 0.00	0.7358 -1.37 -0.04 0.00
0.7456 0.90 -0.09 0.00	1.3097 0.79 0.02 -0.01	1.4537 0.64 0.00 0.00	1.2107 0.74 0.02 0.00	0.6100 0.09 -0.08 0.00	0.9351 0.23 0.02 0.00	0.9343 -0.58 -0.01 0.01	0.7549 -1.30 -0.07 0.01

℄ --

℄

Figure D-3. 2D IAEA PWR Benchmark Problem: Relative Error in Normalized Assembly Power Density.

	Average
Reference	1.0000
Error (%), 15x15 cm	0.39
Error (%), 7.5x7.5 cm	0.04
Error (%), 5x5 cm	0.02

0.9242 -0.84 -0.11 0.00	0.8672 -0.74 -0.10 -0.01	0.8268 -0.75 -0.09 -0.01	0.8530 -0.72 -0.09 -0.03	0.9325 -0.65 -0.07 -0.03	0.9716 -0.63 -0.02 -0.03	0.8465 -0.81 -0.01 -0.06		
1.4810 -0.36 -0.06 0.02	1.2810 -0.19 -0.04 0.01	1.1730 -0.42 -0.05 -0.02	1.2210 -0.31 0.01 0.01	1.4220 0.00 -0.03 -0.07	1.6790 -0.12 0.08 -0.01	1.6210 -0.27 0.07 -0.03	1.3280 -0.37 0.19 -0.04	
1.6610 0.91 -0.01 0.00	1.1510 -0.24 -0.09 -0.01	0.9667 -0.15 -0.02 0.01	1.0220 -0.11 0.02 0.03	1.3390 -0.15 0.01 0.01	2.0510 1.17 0.13 -0.04	2.1610 1.09 0.14 -0.05	1.6210 -0.27 0.07 -0.03	0.8465 -0.81 -0.01 -0.06
1.3860 0.90 -0.04 -0.05	0.9398 0.04 -0.03 0.01	0.7826 0.06 0.00 0.01	0.8432 0.05 0.02 0.01	1.1520 0.01 0.01 -0.01	1.8520 1.18 0.14 -0.02	2.0510 1.17 0.13 -0.04	1.6790 -0.12 0.08 -0.01	0.9716 -0.63 -0.02 -0.03
0.7902 0.10 -0.02 0.02	0.6705 0.31 -0.02 -0.01	0.6181 0.21 0.00 0.01	0.6782 0.21 0.01 0.00	0.8643 0.36 0.01 -0.01	1.1520 0.01 0.01 -0.01	1.3390 -0.15 0.01 0.01	1.4220 0.00 -0.03 -0.07	0.9325 -0.65 -0.07 -0.03
0.5118 0.16 0.01 0.03	0.4904 0.21 0.00 0.01	0.4921 0.23 0.00 0.00	0.5524 0.24 0.01 0.00	0.6782 0.21 0.01 0.00	0.8432 0.05 0.02 0.01	1.0220 -0.11 0.02 0.03	1.2210 -0.31 0.01 0.01	0.8530 -0.72 -0.09 -0.03
0.4130 0.23 0.02 0.02	0.4067 0.23 0.01 0.01	0.4240 0.23 0.00 0.01	0.4921 0.23 0.00 0.00	0.6181 0.21 0.00 0.01	0.7826 0.06 0.00 0.01	0.9667 -0.15 -0.02 0.01	1.1730 -0.42 -0.05 -0.02	0.8268 -0.75 -0.09 -0.01
0.4402 0.29 0.02 0.03	0.3995 0.32 0.01 0.01	0.4067 0.23 0.01 0.01	0.4904 0.21 0.00 0.01	0.6705 0.31 -0.02 -0.01	0.9398 0.04 -0.03 0.01	1.1510 -0.24 -0.09 -0.01	1.2810 -0.19 -0.04 0.01	0.8672 -0.74 -0.10 -0.01
0.6122 0.87 0.04 0.02	0.4402 0.29 0.02 0.03	0.4130 0.23 0.02 0.02	0.5118 0.16 0.01 0.03	0.7902 0.10 -0.02 0.02	1.3860 0.90 -0.04 -0.05	1.6610 0.91 -0.01 0.00	1.4810 -0.36 -0.06 0.02	0.9242 -0.84 -0.11 0.00

℄

℄

Figure D-4. 2D LRA BWR Static Benchmark Problem: Error in Normalized Assembly Power Density.

	Average
Reference	1.0000
Relative Error (%), 15x15 cm	0.42
Relative Error (%), 7.5x7.5 cm	0.04
Relative Error (%), 5x5 cm	0.02

0.9242 -0.91 -0.12 0.00	0.8672 -0.85 -0.12 -0.01	0.8268 -0.91 -0.11 -0.01	0.8530 -0.84 -0.11 -0.04	0.9325 -0.70 -0.08 -0.03	0.9716 -0.65 -0.02 -0.03	0.8465 -0.96 -0.01 -0.07		
1.4810 -0.24 -0.04 0.01	1.2810 -0.15 -0.03 0.01	1.1730 -0.36 -0.04 -0.02	1.2210 -0.25 0.01 0.01	1.4220 0.00 -0.02 -0.05	1.6790 -0.07 0.05 -0.01	1.6210 -0.17 0.04 -0.02	1.3280 -0.28 0.14 -0.03	
1.6610 0.55 -0.01 0.00	1.1510 -0.21 -0.08 -0.01	0.9667 -0.16 -0.02 0.01	1.0220 -0.11 0.02 0.03	1.3390 -0.11 0.01 0.01	2.0510 0.57 0.06 -0.02	2.1610 0.50 0.06 -0.02	1.6210 -0.17 0.04 -0.02	0.8465 -0.96 -0.01 -0.07
1.3860 0.65 -0.03 -0.04	0.9398 0.04 -0.03 0.01	0.7826 0.08 0.00 0.01	0.8432 0.06 0.02 0.01	1.1520 0.01 0.01 -0.01	1.8520 0.64 0.08 -0.01	2.0510 0.57 0.06 -0.02	1.6790 -0.07 0.05 -0.01	0.9716 -0.65 -0.02 -0.03
0.7902 0.13 -0.03 0.03	0.6705 0.46 -0.03 -0.01	0.6181 0.34 0.00 0.02	0.6782 0.31 0.01 0.00	0.8643 0.42 0.01 -0.01	1.1520 0.01 0.01 -0.01	1.3390 -0.11 0.01 0.01	1.4220 0.00 -0.02 -0.05	0.9325 -0.70 -0.08 -0.03
0.5118 0.31 0.02 0.06	0.4904 0.43 0.00 0.02	0.4921 0.47 0.00 0.00	0.5524 0.43 0.02 0.00	0.6782 0.31 0.01 0.00	0.8432 0.06 0.02 0.01	1.0220 -0.11 0.02 0.03	1.2210 -0.25 0.01 0.01	0.8530 -0.84 -0.11 -0.04
0.4130 0.56 0.05 0.05	0.4067 0.57 0.02 0.02	0.4240 0.54 0.00 0.02	0.4921 0.47 0.00 0.00	0.6181 0.34 0.00 0.02	0.7826 0.08 0.00 0.01	0.9667 -0.16 -0.02 0.01	1.1730 -0.36 -0.04 -0.02	0.8268 -0.91 -0.11 -0.01
0.4402 0.66 0.05 0.07	0.3995 0.80 0.03 0.03	0.4067 0.57 0.02 0.02	0.4904 0.43 0.00 0.02	0.6705 0.46 -0.03 -0.01	0.9398 0.04 -0.03 0.01	1.1510 -0.21 -0.08 -0.01	1.2810 -0.15 -0.03 0.01	0.8672 -0.85 -0.12 -0.01
0.6122 1.41 0.07 0.03	0.4402 0.66 0.05 0.07	0.4130 0.56 0.05 0.05	0.5118 0.31 0.02 0.06	0.7902 0.13 -0.03 0.03	1.3860 0.65 -0.03 -0.04	1.6610 0.55 -0.01 0.00	1.4810 -0.24 -0.04 0.01	0.9242 -0.91 -0.12 0.00

℄

℄

Figure D-5. 2D LRA BWR Static Benchmark Problem: Relative Error in Normalized Assembly Power Density.

	Average
Reference - - - - - - - - - - - - - - - - -	1.0000
Error (%), - - - - - - - - - - - - - - - - -	1.06
Relative Error (%), - - - - - - - - - - - -	1.10

0.9722 -0.37 -0.38	0.8753 -0.49 -0.56	0.7515 -0.93 -1.23					
1.3359 0.13 0.10	1.1008 -0.23 -0.21	1.0642 -0.42 -0.39	0.8655 -0.99 -1.14	0.6270 -1.42 -2.26			
1.2581 0.80 0.64	1.4165 0.27 0.19	1.1197 -0.04 -0.04	0.8841 -0.11 -0.13	0.7850 -0.53 -0.67	0.6493 -1.79 -2.76		
1.0294 -2.05 -1.99	1.2195 1.35 1.11	1.2814 1.45 1.13	0.7304 -1.77 -2.43	0.6846 -0.25 -0.36	0.7850 -0.53 -0.67	0.6270 -1.42 -2.26	
0.8404 -0.32 -0.39	1.2566 2.49 1.98	1.0824 1.45 1.34	0.8820 -2.59 -2.94	0.7304 -1.77 -2.43	0.8841 -0.11 -0.13	0.8655 -0.99 -1.14	
1.2094 3.17 2.62	0.8101 -0.81 -1.00	0.9108 -1.30 -1.43	1.0824 1.45 1.34	1.2814 1.45 1.13	1.1197 -0.04 -0.04	1.0642 -0.42 -0.39	0.7515 -0.93 -1.23
1.0362 2.61 2.52	0.8887 -0.46 -0.52	0.8101 -0.81 -1.00	1.2566 2.49 1.98	1.2195 1.35 1.11	1.4165 0.27 0.19	1.1008 -0.23 -0.21	0.8753 -0.49 -0.56
0.8814 -0.10 -0.11	1.0362 2.61 2.52	1.2094 3.17 2.62	0.8404 -0.32 -0.39	1.0294 -2.05 -1.99	1.2581 0.80 0.64	1.3359 0.13 0.10	0.9722 -0.37 -0.38

℄ - -

℄

Figure D-6. CISE BWR Benchmark Problem: Error in Normalized Assembly Power Density.

	Average
Reference	1.0000
Error (%),	1.20
Relative Error (%),	1.29

0.5503 0.42 0.77	0.4973 0.67 1.36	0.5737 0.49 0.86	0.5632 0.77 1.37	0.6332 0.69 1.10	0.5091 0.70 1.37	0.3936 0.61 1.55		
0.7833 0.32 0.41	0.8096 0.37 0.46	0.7761 0.53 0.68	0.9988 0.10 0.10	0.9697 0.86 0.89	0.9887 0.50 0.50	0.6886 0.87 1.27		
1.0152 1.13 1.12	0.6215 -0.32 -0.51	0.7339 -1.42 -1.93	1.0813 1.77 1.64	1.3550 1.33 0.98	1.1996 1.64 1.37	1.0885 1.35 1.24	0.6886 0.87 1.27	0.3936 0.61 1.55
0.9993 1.26 1.26	0.8282 -3.42 -4.13	0.7878 -3.64 -4.62	1.2401 0.98 0.79	1.2596 1.79 1.42	1.4634 0.82 0.56	1.1996 1.64 1.37	0.9887 0.50 0.50	0.5091 0.70 1.37
0.9239 -0.74 -0.80	1.2374 1.97 1.59	1.3736 1.00 0.73	0.8669 -1.81 -2.09	0.9642 -2.41 -2.49	1.2596 1.79 1.42	1.3550 1.33 0.98	0.9697 0.86 0.89	0.6332 0.69 1.10
1.0752 -4.66 -4.34	1.7175 0.30 0.17	1.5325 0.91 0.59	1.1174 -5.84 -5.23	0.8669 -1.81 -2.09	1.2401 0.98 0.79	1.0813 1.77 1.64	0.9988 0.10 0.10	0.5632 0.77 1.37
1.3517 -1.83 -1.36	1.5115 -0.07 -0.05	1.6583 -1.23 -0.74	1.5325 0.91 0.59	1.3736 1.00 0.73	0.7878 -3.64 -4.62	0.7339 -1.42 -1.93	0.7761 0.53 0.68	0.5737 0.49 0.86
1.2997 0.03 0.02	1.7191 -0.38 -0.22	1.5115 -0.07 -0.05	1.7175 0.30 0.17	1.2374 1.97 1.59	0.8282 -3.42 -4.13	0.6215 -0.32 -0.51	0.8096 0.37 0.46	0.4973 0.67 1.36
1.4962 -0.54 -0.36	1.2997 0.03 0.02	1.3517 -1.83 -1.36	1.0752 -4.66 -4.34	0.9239 -0.74 -0.80	0.9993 1.26 1.26	1.0152 1.13 1.12	0.7833 0.32 0.41	0.5503 0.42 0.77

℄

℄

Figure D-7. HAFAS BWR Benchmark Problem: Error in Normalized Assembly Power Density.

Reference, CITATION (21*21) --------	1.5351E+08
Relative Error, QUAGMIRE (1*1) ------	1.24%
Relative Error, QUAGMIRE (2*2) ------	0.03%
Relative Error, QUANDRY (1*1) -------	0.23%

Group 1 Flux

2	1.1453E+09 1.62% -0.10% 0.17%	5.9976E+08 -2.15% 0.29% -0.52%
1	1.6942E+09 1.81% -0.01% 0.00%	1.1453E+09 1.62% -0.10% 0.17%
	1	2

Group 2 Flux

2	1.6328E+08 1.84% -0.17% 0.04%	8.7252E+07 -2.38% 0.45% -0.57%
1	1.5351E+08 1.24% 0.03% 0.23%	1.6328E+08 1.84% -0.17% 0.04%
	1	2

Figure D-8. Two-Group Source Benchmark Problem: Error in Assembly-Averaged Flux.

	Average
Reference - - - - - - - - - - - - - - -	1.000
Error (%), 20x20 cm - - - - - - - -	0.27
Error (%), 10x10 cm - - - - - - - -	0.09

	0.773 -0.08 -0.15	0.753 0.15 -0.08	0.707 0.39 0.11					
	0.958 -0.11 -0.06	0.974 -0.07 -0.04	0.997 0.16 0.15	0.864 0.49 0.21	0.608 0.72 0.24			
	0.954 -0.20 -0.19	1.055 -0.24 -0.08	1.088 0.00 0.07	0.923 0.15 0.00	0.699 0.58 0.10	0.597 0.20 0.17		
	0.610 0.07 0.13	1.072 -0.14 -0.08	1.181 -0.34 0.00	0.972 0.04 0.00	0.475 -0.13 0.17	0.699 0.58 0.10	0.608 0.72 0.24	
	1.195 -0.49 -0.12	1.292 -0.43 -0.09	1.311 0.00 0.07	1.179 -0.14 0.00	0.972 0.04 0.00	0.923 0.15 0.00	0.864 0.49 0.21	
	1.423 -0.68 0.00	1.432 -0.32 0.00	1.369 -0.27 0.00	1.311 0.00 0.07	1.181 -0.34 0.00	1.088 0.00 0.07	0.997 0.16 0.15	0.707 0.39 0.11
	1.283 -0.68 -0.14	1.398 -0.56 0.00	1.432 -0.32 0.00	1.292 -0.43 -0.09	1.072 -0.14 -0.08	1.055 -0.24 -0.08	0.974 -0.07 -0.04	0.753 0.15 -0.08
℄ — —	0.729 0.22 0.17	1.283 -0.68 -0.14	1.423 -0.68 0.00	1.195 -0.49 -0.12	0.610 0.07 0.13	0.954 -0.20 -0.19	0.958 -0.11 -0.06	0.773 -0.08 -0.15
	| | ℄							

Figure D-9. 3D IAEA PWR Benchmark Problem: Error in Normalized Assembly Power Density.

	Average
Reference ---------------	1.000
Relative Error (%), 20x20 cm - -	0.30
Relative Error (%), 10x10 cm - -	0.11

	0.773 -0.10 -0.19	0.753 0.20 -0.10	0.707 0.55 0.16					
	0.958 -0.11 -0.06	0.974 -0.07 -0.04	0.997 0.16 0.15	0.864 0.57 0.24	0.608 1.18 0.40			
	0.954 -0.21 -0.20	1.055 -0.23 -0.08	1.088 0.00 0.06	0.923 0.16 0.00	0.699 0.83 0.15	0.597 0.33 0.29		
	0.610 0.12 0.22	1.072 -0.13 -0.07	1.181 -0.29 0.00	0.972 0.04 0.00	0.475 -0.27 0.36	0.699 0.83 0.15	0.608 1.18 0.40	
	1.195 -0.41 -0.10	1.292 -0.33 -0.07	1.311 0.00 0.05	1.179 -0.12 0.00	0.972 0.04 0.00	0.923 0.16 0.00	0.864 0.57 0.24	
	1.423 -0.48 0.00	1.432 -0.22 0.00	1.369 -0.20 0.00	1.311 0.00 0.05	1.181 -0.29 0.00	1.088 0.00 0.06	0.997 0.16 0.15	0.707 0.55 0.16
	1.283 -0.53 -0.11	1.398 -0.40 0.00	1.432 -0.22 0.00	1.292 -0.33 -0.07	1.072 -0.13 -0.07	1.055 -0.23 -0.08	0.974 -0.07 -0.04	0.753 0.20 -0.10
℄ --	0.729 0.30 0.23	1.283 -0.53 -0.11	1.423 -0.48 0.00	1.195 -0.41 -0.10	0.610 0.12 0.22	0.954 -0.21 -0.20	0.958 -0.11 -0.06	0.773 -0.10 -0.19
	| | ℄							

Figure D-10. 3D IAEA PWR Benchmark Problem: Relative Error in Normalized Assembly Power Density.

	Average
Reference	1.0000
Error (%), 15x15x25(15) cm	0.36
Error (%), 7.5x7.5x12.5(7.5) cm	0.04

0.9241 -0.83 -0.10	0.8671 -0.73 -0.09	0.8267 -0.74 -0.08	0.8527 -0.68 -0.05	0.9321 -0.59 -0.03	0.9711 -0.54 0.02	0.8457 -0.69 0.06		
1.4811 -0.36 -0.08	1.2811 -0.19 -0.05	1.1729 -0.39 -0.03	1.2212 -0.30 0.00	1.4212 0.13 0.05	1.6787 -0.02 0.09	1.6204 -0.13 0.10	1.3271 -0.21 0.24	
1.6606 0.93 -0.01	1.1510 -0.26 -0.08	0.9670 -0.18 -0.03	1.0225 -0.16 -0.01	1.3391 -0.14 0.00	2.0499 1.33 0.17	2.1596 1.31 0.20	1.6204 -0.13 0.10	0.8457 -0.69 0.06
1.3851 0.95 0.01	0.9401 -0.02 -0.04	0.7830 0.00 -0.02	0.8436 0.00 0.00	1.1520 0.01 0.01	1.8512 1.29 0.15	2.0499 1.33 0.17	1.6787 -0.02 0.09	0.9711 -0.54 0.02
0.7906 0.02 -0.05	0.6706 0.27 -0.01	0.6184 0.15 -0.01	0.6784 0.17 0.01	0.8643 0.35 0.03	1.1520 0.01 0.01	1.3391 -0.14 0.00	1.4212 0.13 0.05	0.9321 -0.59 -0.03
0.5123 0.08 -0.02	0.4907 0.15 -0.01	0.4923 0.18 0.00	0.5527 0.18 0.00	0.6784 0.17 0.01	0.8436 0.00 0.00	1.0225 -0.16 -0.01	1.2212 -0.30 0.00	0.8527 -0.68 -0.05
0.4134 0.15 -0.01	0.4070 0.17 -0.01	0.4243 0.17 -0.01	0.4923 0.18 0.00	0.6184 0.15 -0.01	0.7830 0.00 -0.02	0.9670 -0.18 -0.03	1.1729 -0.39 -0.03	0.8267 -0.74 -0.08
0.4406 0.21 -0.01	0.3998 0.25 -0.01	0.4070 0.17 -0.01	0.4907 0.15 -0.01	0.6706 0.27 -0.01	0.9401 -0.02 -0.04	1.1510 -0.26 -0.08	1.2811 -0.19 -0.05	0.8671 -0.73 -0.09
0.6124 0.78 0.01	0.4406 0.21 -0.01	0.4134 0.15 -0.01	0.5123 0.08 -0.02	0.7906 0.02 -0.05	1.3851 0.95 0.01	1.6606 0.93 -0.01	1.4811 -0.36 -0.08	0.9241 -0.83 -0.10

℄

℄

Figure D-11. 3D LRA BWR Static Benchmark Problem: Error in Normalized Assembly Power Density.

	Average
Reference	1.0000
Relative Error (%), 15x15x25(15) cm	0.37
Relative Error (%), 7.5x7.5x12.5(7.5) cm	0.04

0.9241 -0.90 -0.11	0.8671 -0.84 -0.10	0.8267 -0.90 -0.10	0.8527 -0.80 -0.06	0.9321 -0.63 -0.03	0.9711 -0.56 0.02	0.8457 -0.82 0.07		
1.4811 -0.24 -0.05	1.2811 -0.15 -0.04	1.1729 -0.33 -0.03	1.2212 -0.25 0.00	1.4212 0.09 0.04	1.6787 -0.01 0.05	1.6204 -0.08 0.06	1.3271 -0.16 0.18	
1.6606 0.56 -0.01	1.1510 -0.23 -0.07	0.9670 -0.19 -0.03	1.0225 -0.16 -0.01	1.3391 -0.10 0.00	2.0499 0.65 0.08	2.1596 0.61 0.09	1.6204 -0.08 0.06	0.8457 -0.82 0.07
1.3851 0.69 0.01	0.9401 -0.02 -0.04	0.7830 0.00 -0.03	0.8436 0.00 0.00	1.1520 0.01 0.01	1.8512 0.70 0.08	2.0499 0.65 0.08	1.6787 -0.01 0.05	0.9711 -0.56 0.02
0.7906 0.03 -0.06	0.6706 0.40 -0.01	0.6184 0.24 -0.02	0.6784 0.25 0.01	0.8643 0.40 0.03	1.1520 0.01 0.01	1.3391 -0.10 0.00	1.4212 0.09 0.04	0.9321 -0.63 -0.03
0.5123 0.16 -0.04	0.4907 0.31 -0.02	0.4923 0.37 0.00	0.5527 0.33 0.00	0.6784 0.25 0.01	0.8436 0.00 0.00	1.0225 -0.16 -0.01	1.2212 -0.25 0.00	0.8527 -0.80 -0.06
0.4134 0.36 -0.02	0.4070 0.42 -0.02	0.4243 0.40 -0.02	0.4923 0.37 0.00	0.6184 0.24 -0.02	0.7830 0.00 -0.03	0.9670 -0.19 -0.03	1.1729 -0.33 -0.03	0.8267 -0.90 -0.10
0.4406 0.48 -0.02	0.3998 0.63 -0.03	0.4070 0.42 -0.02	0.4907 0.31 -0.02	0.6706 0.40 -0.01	0.9401 -0.02 -0.04	1.1510 -0.23 -0.07	1.2811 -0.15 -0.04	0.8671 -0.84 -0.10
0.6124 1.41 0.02	0.4406 0.48 -0.02	0.4134 0.36 -0.02	0.5123 0.16 -0.04	0.7906 0.03 -0.06	1.3851 0.69 0.01	1.6606 0.56 -0.01	1.4811 -0.24 -0.05	0.9241 -0.90 -0.11

℄

℄

Figure D-12. 3D LRA BWR Static Benchmark Problem: Relative Error in Normalized Assembly Power Density.